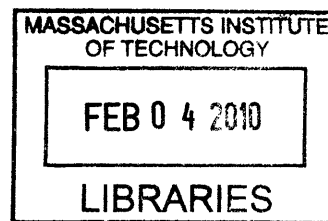Single-Walled Carbon Nanotubes as Near Infrared Fluorescent Sensors: Characterization, Biological and Analytical Applications

by

Hong Jin

B.E. Chemical Engineering
Tsinghua University, 2005
M.S. Chemical and Biomolecular Engineering
University of Illinois at Urbana-Champaign, 2007

SUBMITTED TO THE DEPARTMENT OF CHEMICAL ENGINEERING IN
PARTIAL FULFILLMENT OF THE REQUIREMENTS FOR THE DEGREE OF

DOCTOR OF PHILOSOPHY IN CHEMICAL ENGINEERING
AT THE
MASSACHUSETTS INSTITUTE OF TECHNOLOGY

OCT 2009

ARCHIVES

Signature of Author: _

Department of Chemical Engineering
OCT 19, 2009

Certified by: _____

Michael S. Strano
Associate Professor of Chemical Engineering
Thesis Supervisor

Accepted by: _____

William M. Deen
Professor of Chemical Engineering
Chairperson, Department Committee for Graduate Students

1

Single-Walled Carbon Nanotubes as Near Infrared Fluorescent Sensors: Characterization, Biological and Analytical Applications

by

Hong Jin

Submitted to the Department of Chemical Engineering
on OCT 22, 2009, in Partial Fulfillment of the
Requirements for the Degree of
Doctor of Philosophy

Abstract

Reactive oxygen species (ROS) have emerged as biological signaling molecules, participating in newly discovered cascades that govern cell proliferation, migration, and pathogenesis. A major challenge in understanding these pathways is the lack of detection technologies that allow for spatial and temporal resolution of specific ROS at the cellular level. The goal of this thesis is to design a nanotube sensor platform able to detect and study H_2O_2 signaling fluxes at the cellular level in order to elucidate their role in biological processes. Understanding this role may lead to new therapeutic targets, and improve understanding of biological signaling. Single-walled carbon nanotubes (SWNT) are rolled sheets of graphene and can be either semiconducting or metallic depending on the angle of rolling and the diameter of the tube. Semi-conducting SWNT are one of only a few types of molecules that exhibit band gap photoluminescence (PL) in the near infrared (nIR), making them ideal for detection in biologically relevant media since it avoids biological auto-fluorescence. SWNT are also completely photostable even at high fluence, unlike conventional fluorophores and quantum dot systems, allowing them to serve as nIR single molecule optical sensors capable of long term and stable operations *in vitro* and *in vivo*.

In this thesis, we show that the 1D quantum confinement of photogenerated excitons in SWNT can amplify the detection of molecular adsorption to where single-molecule discrimination is realizable, even from within living cells and tissues. We have developed a type I collagen film, similar to those used as 3D cell scaffolds for tissue engineering, containing embedded SWNT capable of reporting single-molecule adsorption of quenching molecules such as H_2O_2. A Hidden Markov Modeling algorithm is utilized to link single-molecule adsorption events detected on the nanotube to forward and reverse kinetic rate constants for many different analytes. The collagen matrix is shown to impart selectivity to H_2O_2 over other ROS and common interferents.

We utilized these new single-molecule sensors to study the fluxes of H_2O_2 from A431 human skin carcinoma cells and particularly the local generation rate from Epidermal Growth Factor Receptor (EGFR), a membrane protein and tyrosine kinase that controls cell proliferation among other functions. We show that an array of nIR fluorescent SWNT is capable of recording the discrete, stochastic quenching events that

occur as H_2O_2 molecules are emitted from individual A431 and murine 3T3 fibroblasts cells in response to epidermal growth factor (EGF). We also show mathematically that such single molecule detection arrays have the unique property of distinguishing between "near field" and "far field" molecular generation, allowing one to isolate the flux originating from only the membrane protein. Corresponding inhibition experiments suggest a mechanism whereby water oxidizes singlet oxygen at a catalytic site on the receptor itself, generating H_2O_2 in response to receptor binding. An EGFR-mediated H_2O_2 generation pathway that is consistent with all current and previous literature findings has been proposed for the first time and numerically tested for consistency.

In an effort to extend this detection to *in vivo* systems, we investigated how SWNT are uptaken and localized within living cells and as well as their potential cytotoxicity. To this end, we have developed a novel method of studying this problem by tracking the non-photobleaching SWNT in real time by using a single particle tracking method. Over 10,000 individual trajectories of SWNT were tracked as they are incorporated into and expelled from NIH-3T3 cells in real time on a perfusion microscope stage. An analysis of mean square displacement allows the complete construction of the mechanistic steps involved from single duration experiments. We observe the first conclusive evidence of SWNT exocytosis and show that the rate closely matches the endocytosis rate with negligible temporal offset, thus explains why SWNT are non-cytotoxic for various cell types at a concentration up to 5 mg/L, as observed from our live-dead assay experimental results. Further, we studied the cellular uptake and expulsion rates of length-fractionated SWNT from 130 to 660 nm in NIH-3T3 cells using this method. We developed a quantitative model to correlate endocytosis rate with nanoparticle geometry that accurately describes our data set and also literature results for Au nanoparticles. The model asserts that nanoparticles cluster on the cell membrane to form a size sufficient to generate a large enough enthalpic contribution via receptor ligand interations to overcome the elastic energy and entropic barriers associated with vesicle formation. The total uptake of both SWNT and Au nanoparticles is maximal at a common radius of 25 nm when scaled using an effective capture dimension for membrane diffusion. The ability to understand and predict the cellular uptake of nanoparticles quantitatively should find utility in designing nanosystems with controlled toxicity, efficacy and functionality.

The development of such single molecule detection technologies for ROS motivates their application to many other unexplored signaling pathways both *in vitro* and *in vivo*.

Thesis Supervisor: Michael S. Strano
Title: Associate Professor of Chemical Engineering

Acknowledgements

"Bernard of Chartres used to say that we are like dwarfs on the shoulders of giants, so that we can see more than they, and things at a greater distance, not by virtue of any sharpness of sight on our part, or any physical distinction, but because we are carried high and raised up by their giant size."

----by John of Salisbury, from Metalogicon

This work would not have been completed without my advisor, Dr. Michael S. Strano, who has helped me to shape my project quite a bit according to my interest. His curiosity and enthusiasm in research, together with his sharpness in science, has transitioned me from a fresh college student into a young scientist. I still vividly remember the day when I brought into his office the first real-time movie of nanotubes moving across living cells. We were both very exited and there we were, sitting in his office, and watching the movie again and again until 7 pm that day. His enthusiasm has inspired me to work hard with passion, which leads to fruitful results as evidenced by my 6 first-authored, 3 co-authored publications in high-impact journals, 8 conference presentations and contribution to 3 book chapters in 4 years. One of my papers, based on the nanotube movies, has won the first prize in the graduate student paper competition hosted by the organization of American Institute of Chemical Engineers (AIChE), which is the world's leading organization for chemical engineering professionals with more than 40,000 members in 93 countries.

I would also like to express my gratitude to Dr. K. Dane Wittrup and Dr. Gregory Stephanopoulos for taking an active interest in my work since I came to MIT. They teach me to always think physically when setting up a mathematical model, which has benefited me by a lot.

The rest of the giants that make this work possible are, by all means, the members of the Strano Group. I tried to figure out one person who has not helped me to survive the seemingly endless, sometimes desperate journey, and I cannot think of the name of one single person. However, if I only have the space to mention one person, it would always be Daniel A. Heller, a very talented, hardworking and productive young scientist in my group. Dan has taught me everything that one can ever possibly teach on science and beyond. My PhD life has been better because he has always been there for me.

Last but not least, I would like to thank my parents. Although they are thousands of miles away, they always believe in me and encourage me to climb the mountains of challenges and never give up. I would not be where I am today without them. So any accomplishment is as much of theirs as it is mine.

Table of Contents

List of Figures

8

List of Tables

1. Introduction

1.1 Background of Single-Walled Carbon Nanotubes

Discovered in 1991 by Iijima and co-workers[1], single-walled carbon nanotubes (SWNT) are rolled sheets of graphene[2-4]. Depending on the angle of rolling and the diameter of the tube, SWNT can be either semiconducting or metallic[5,6].

The diameters of semi-conducting SWNT are around 1 nm and are one of only a few types of molecules that exhibit band gap photoluminescence (PL) in the near infrared (nIR)[7-10] when dispersed in solution. The fluorescence is completely photostable even at high fluence, unlike conventional fluorophores and even quantum dot systems. Several promising applications of SWNT nIR emission are under investigation, including imaging and electroluminescent devices[11]. We have pioneered their use as optical sensors, both as biomedical devices[7,12,13] and as sub-cellular molecular beacons[8,14].

Toward the latter application, sensors designed to exploit nanotube PL have modulated fluorescence wavelength by modifying solution and adsorbate properties[9,14], or have used either redox chemistry to populate/depopulate the first interband transition, or E_{11} band[7,12,13]. The former has been described as solvatochromism[15] and will be discussed in detail in Chapter 3.1. Generally, when the adsorbate surface coverage on nanotubes dispersed in aqueous solution decreases, the emission energy decreases (due to an increase in the dielectric constant from water exposure). Upon dilution of a solution of sodium dodecyl sulfate (SDS) suspended SWNT below the critical micelle concentration (CMC), the fluorescence energy systematically decreases; emission exhibits a surfactant concentration-dependent red-shift[16]. The detection limit of the latter has been extended down to single molecule level by others[17] and our own laboratory[18]

from analyzing the stepwise quenching of single molecules as they adsorb to the SWNT surface. This mechanism will be discussed in detail in Chapter 3.2.

1.2 Structure of Biopolymer-Wrapped Single-Walled Carbon Nanotubes

Various polymers have been used to suspend nanotubes in solution. In this work, only biopolymers (DNA, collagen) are considered because of the *in vitro* nature of this study. Briefly, nanotubes and biopolymers are mixed and bath or probe sonicated[18,19]. Centrifugation/ultracentrifugation and dialysis are performed post-sonication to purify the sample[20]. In the following, DNA is used as a model of a prototypical biopolymer wrapping around SWNT.

DNA is highly polymorphic and several types of single[9] and double stranded oligonucleotides can adsorb to the surface of SWNT. AFM measurements of the $d(GT)_{15}$-SWNT complex, conducted in air, show a regular banding pattern along the nanotube (Fig. 1.1a, b). The band heights reach up to 1.2 nm above the surface of the nanotube, with typical heights of 0.7-0.8 nm, and exhibit a regular spacing of 14-20 nm (Fig. 1.1c). Measurements conducted in fluid show greatly diminished banding attributed to the effective increase of DNA's hydrated radius compared to the dehydrated strand (Fig. 1.1d-f). However, a random single-stranded DNA (5'-TAG CTA TGG AAT TCC TCG TAG GCA-3', henceforth called DNA1) adsorbs in a globular manner on SWNT, as observed from its AFM image in air (Fig. 1.1g-h). The average diameter of DNA1-SWNT complex is estimated as its radius of gyration and calculated to be 1.66 nm ($d=l\sqrt{N}$, where l is the length between adjacent bases and N is the number of bases), assuming the single-stranded DNA chains are behaving as free non-entangled Gaussian chains. This is consistent with the average height that is observed by AFM where the

12

nanotube height is ~1 nm. The smaller extension of d(GT)$_{15}$ from the nanotube also implies a tighter binding to its surface, and the regular banding pattern suggests a more uniform conformation of the oligonucleotide. These conclusions concur with the observed relative stability of the d(GT)$_x$ oligonucleotide binding to the nanotube[21].
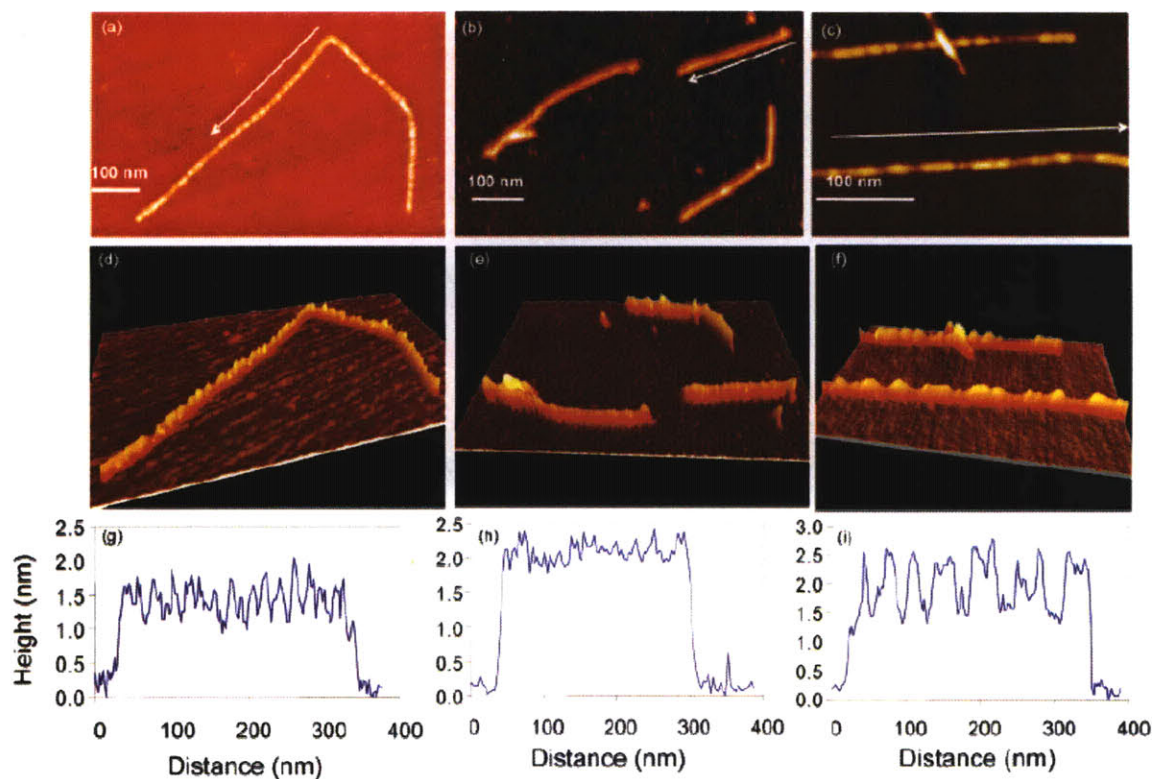
Figure 1.1 AFM images of DNA-SWNT complexes. (a) AFM height image of d(GT)$_{15}$-SWNT on freshly-cleaved mica conducted in air showing regular banding pattern of the d(GT)$_{15}$ oligonucleotide extending up to 0.8 nm above the surface of the nanotube. (b) Wet AFM of d(GT)$_{15}$-SWNT in water shows diminished bands. (c) AFM of DNA1-SWNT in air shows pronounced bands reaching 1 nm above the nanotube surface on average. (d-f) 3D renderings of the micrographs. (g-i) Height profiles of the nanotubes denoted by the white arrows in the original height images.

The structure of biopolymers on the nanotube plays a key role in the PL modulation of SWNT, and their subsequent application as sensors. We will elaborate on the sensing mechanism based on this in Chapter 3.1.

Some of the work is reproduced in part with permission from Ref 18, 19, 20, 50, copyright 2009 American Chemical Society.

1.3 The Motivation and Goals of This Work

Reactive oxygen species (ROS) have emerged as biological signaling molecules, participating in newly discovered cascades that govern cell proliferation, migration, and pathogenesis. A major challenge in understanding these pathways is the lack of detection technologies that allow for spatial and temporal resolution of specific ROS at the cellular level. The goal of this thesis is to design a nanotube sensor platform able to detect and study H_2O_2 signaling fluxes at the cellular level in order to elucidate their role in biological processes. Understanding this role may lead to new therapeutic targets, and improve understanding of biological signaling. Single-walled carbon nanotubes (SWNT) are rolled sheets of graphene and can be either semiconducting or metallic depending on the angle of rolling and the diameter of the tube. Semi-conducting SWNT are one of only a few types of molecules that exhibit band gap photoluminescence (PL) in the near infrared (nIR), making them ideal for detection in biologically relevant media since it avoids biological auto-fluorescence. SWNT are also completely photostable even at high fluence, unlike conventional fluorophores and quantum dot systems, allowing them to serve as nIR single molecule optical sensors capable of long term and stable operations *in vitro* and *in vivo*.

In this thesis, we show that the 1D quantum confinement of photogenerated excitons in SWNT can amplify the detection of molecular adsorption to where single-molecule discrimination is realizable, even from within living cells and tissues. We have developed a type I collagen film, similar to those used as 3D cell scaffolds for tissue

engineering, containing embedded SWNT capable of reporting single-molecule adsorption of quenching molecules such as H_2O_2. A Hidden Markov Modeling algorithm is utilized to link single-molecule adsorption events detected on the nanotube to forward and reverse kinetic rate constants for many different analytes. The collagen matrix is shown to impart selectivity to H_2O_2 over other ROS and common interferents.

We utilized these new single-molecule sensors to study the fluxes of H_2O_2 from A431 human skin carcinoma cells and particularly the local generation rate from Epidermal Growth Factor Receptor (EGFR), a membrane protein and tyrosine kinase that controls cell proliferation among other functions. We show that an array of nIR fluorescent SWNT is capable of recording the discrete, stochastic quenching events that occur as H_2O_2 molecules are emitted from individual A431 and murine 3T3 fibroblasts cells in response to epidermal growth factor (EGF). We also show mathematically that such single molecule detection arrays have the unique property of distinguishing between "near field" and "far field" molecular generation, allowing one to isolate the flux originating from only the membrane protein. Corresponding inhibition experiments suggest a mechanism whereby water oxidizes singlet oxygen at a catalytic site on the receptor itself, generating H_2O_2 in response to receptor binding. An EGFR-mediated H_2O_2 generation pathway that is consistent with all current and previous literature findings has been proposed for the first time and numerically tested for consistency.

In an effort to extend this detection to *in vivo* systems, we investigated how SWNT are uptaken and localized within living cells and as well as their potential cytotoxicity. To this end, we have developed a novel method of studying this problem by tracking the non-photobleaching SWNT in real time by using a single particle tracking

method. Over 10,000 individual trajectories of SWNT were tracked as they are incorporated into and expelled from NIH-3T3 cells in real time on a perfusion microscope stage. An analysis of mean square displacement allows the complete construction of the mechanistic steps involved from single duration experiments. We observe the first conclusive evidence of SWNT exocytosis and show that the rate closely matches the endocytosis rate with negligible temporal offset, thus explains why SWNT are non-cytotoxic for various cell types at a concentration up to 5 mg/L, as observed from our live-dead assay experimental results. Further, we studied the cellular uptake and expulsion rates of length-fractionated SWNT from 130 to 660 nm in NIH-3T3 cells using this method. We developed a quantitative model to correlate endocytosis rate with nanoparticle geometry that accurately describes our data set and also literature results for Au nanoparticles. The model asserts that nanoparticles cluster on the cell membrane to form a size sufficient to generate a large enough enthalpic contribution via receptor ligand interations to overcome the elastic energy and entropic barriers associated with vesicle formation. The total uptake of both SWNT and Au nanoparticles is maximal at a common radius of 25 nm when scaled using an effective capture dimension for membrane diffusion. The ability to understand and predict the cellular uptake of nanoparticles quantitatively should find utility in designing nanosystems with controlled toxicity, efficacy and functionality.

The development of such single molecule detection technologies for ROS motivates their application to many other unexplored signaling pathways both *in vitro* and *in vivo*.

16

2. Cell-Nanotube Interactions

2.1 Cellular Endocytosis, Intracellular Trafficking and Exocytosis of Nanotubes

2.1.1 Introduction

There is much concern over the fate of nanoparticles in biological systems with the development of novel inorganic nanomaterials such as nanotubes, nanowires and quantum dots. The single most important factor to be considered before designing an *in vitro* nanotube sensor is its compatibility with the cells. In this chapter, we aim at understanding how SWNT are uptaken and processed by the cells. The motivation stems from the goal of better designing nanotubes as *in vitro* sensors, the interest in basic nanoparticle toxicology [22,23], and also promising applications such as drug delivery [24,25], photodynamic therapy [26,27], and implantable sensors [8,14].

Carbon nanotubes, like other nanoparticles, under certain conditions of functionalization, are readily taken up by cells, and are non-cytotoxic over a wide range of conditions [28-31]. Understanding the uptake mechanism of nanoparticles has been the focus of several recent studies [28-30,32-35]. However, there is some debate on the uptake mechanism, which may vary based on the specific functionalization. Endocytosis, which describes a process for cells to absorb exogenous materials from the outside by engulfing it in a pocket formed from the cell membrane, is one of the major pathways for cellular uptake of nanoparticles [28-30,32-34,36]. The two categories for endocytosis are receptor-mediated and receptor-independent. The clathrin-mediated pathway is one of the well-studied receptor-dependent endocytosis (RME) pathways [37,38]. While some reports show that Au nanoparticles and short SWNT with various functionalities are internalized via clathrin-mediated endocytosis[28,32-34], others argue that nanoparticle uptake may not solely

depend on endocytosis[35,39]. It should be noted that nanoparticles displaying different functional groups are internalized via different uptake mechanisms[35].

The role of intracellular aggregation is important in the fate of internalized nanoparticles. However, only a few examples are reported in literature. For instance, the aggregates within cells observed on Au nanorods coated with cetyltrimethylammonium bromide (CTAB)[40]. We also observed, via TEM, aggregation within intracellular vesicles of DNA-wrapped SWNT after incorporation by murine myoblast stem cells[8]. It is not clear if these aggregates form in the cell by endosomal fusion, on the outer membrane surface via surface diffusion, or in solution and are subsequently incorporated as an intact aggregate. Indeed, all three mechanisms may occur.

Another central question is the existence of exocytosis, which is very important in nanotube cytotoxicity. A discussion of this process for nanoparticles is nearly absent from the literature. The exceptions are in recently published works on Au nanoparticles[32], where the removal of transferrin-coated nanoparticles was found to be linearly related to size, and poly (D,L-lactide-co-glycolide; PLGA) nanoparticles[41], where exocytosis occurred for about 65% of the internalized fraction over a 30 min period after the extracellular nanoparticle concentration gradient was removed.

Single particle tracking (SPT) using fluorophores is a recently developed technique for answering the questions mentioned above in cellular systems [42-44], although with small molecule fluorophores and quantum dots, photobleaching is a major limitation to real-time measurements. The photobleaching time constrains the observation window during tracking so that events that occur on the order of several hours must be observed through multiple and distinct incubation periods, with each observation starting at a

different time after incubation. In practice, this lack of continuity has prevented the complete and continuous mapping of transport pathways.

In this chapter, we use the intrinsic band gap fluorescence of DNA-suspended SWNT (DNA-SWNT) to track their interactions with NIH-3T3 cells using a 2D InGaAs imaging array coupled to an inverted microscope with a perfusion stage. Because the SWNT emission undergoes no observable photobleaching, and cells do not autofluoresce in the nIR, we are able to completely map the pathways involved in cellular uptake for the first time by continuously tracking 10,288 independent trajectories for over 127 min using SPT methods. In the SPT method, microscopic theory is applied where diffusion is defined as the random migration of molecules or small particles arising from motion due to thermal energy [45]. Mean squared displacement (MSD) is computed based on the position of the particle over time [46-48]. The analytical expressions of the curves of MSD versus time form the basis of classification. There are basically four types of motion, including normal diffusion (MSD = 4Dt (Eq. 2.1), where D is the microscopic diffusion coefficient, derived from a two-dimensional random walk[45]. The expressions are MSD = 2Dt and MSD = 6Dt for one-dimensional and three-dimensional random walks respectively), anomalous diffusion (MSD = $4Dt^{\alpha}$ (Eq. 2.2), where $\alpha<1$), directed/convective motion with diffusion (MSD = 4Dt + $(Vt)^2$ (Eq. 2.3), where V is velocity) and corralled/confined motion with diffusion (MSD = $C[1-A_1\exp(-4A_2Dt/C)]$ (Eq. 2.4), where C is the corral size, A_1 and A_2 are constants determined by the corral geometry) [49].

Trajectories that show distinct signatures of adsorption, endocytosis, confined diffusion (both on the cell membrane and inside the cell), exocytosis and desorption are

identified and are then used to construct the complete pathway. We observe the first conclusive evidence of SWNT exocytosis in this system, and show that the rate closely matches the endocytosis rate with negligible temporal offset. We identify and study a unique pathway that leads to the previously observed aggregation and accumulation of SWNT within the cells. The results have significant implications for the use of nanoparticles in biological systems.

2.1.2 Experimental Results, Model Algorithm and Discussion

To test if proteins in cell media adsorb to the SWNT surface, we performed gel electrophoresis on DNA-SWNT with and without exposure to media. Figure 2.1A demonstrates an electrophoretic mobility difference between DNA-SWNT in water and in media in a 1 wt% agarose gel (see Appendix A). DNA-SWNT in media (Fig. 2.1A, lane 2) move more slowly, indicating the DNA-SWNT surface charge or size in media reduces their mobility, as compared to that in water (Fig. 2.1A, lane 1). Spectral shifting of DNA-SWNT in water and media suggests that proteins adsorb on the outer DNA layer without changing the local dielectric properties significantly[50]. Protein attachment without DNA displacement or rearrangement on SWNT is consistent with these observations. While intuitive, these results have not been demonstrated for SWNT and we feel the result significantly informs the current debate concerning the mechanism of DNA-SWNT cellular uptake, where proteins adsorb to both the SWNT and the receptors on the cell membrane, facilitating receptor-mediated endocytosis, consistent with what Dai and co-workers have observed[34]. Further, colocalization of SWNT fluorescence in 3T3 cells with the lysosomal stain (Lysotracker) shows overlap, suggesting DNA-SWNT presence in lysosomes, which is part of the endocytosis pathway (Fig. 2.2). However, we

note that our model and analysis platform are independent of the uptake mechanism thus can be used as a general analysis method across various particles and cell lines.
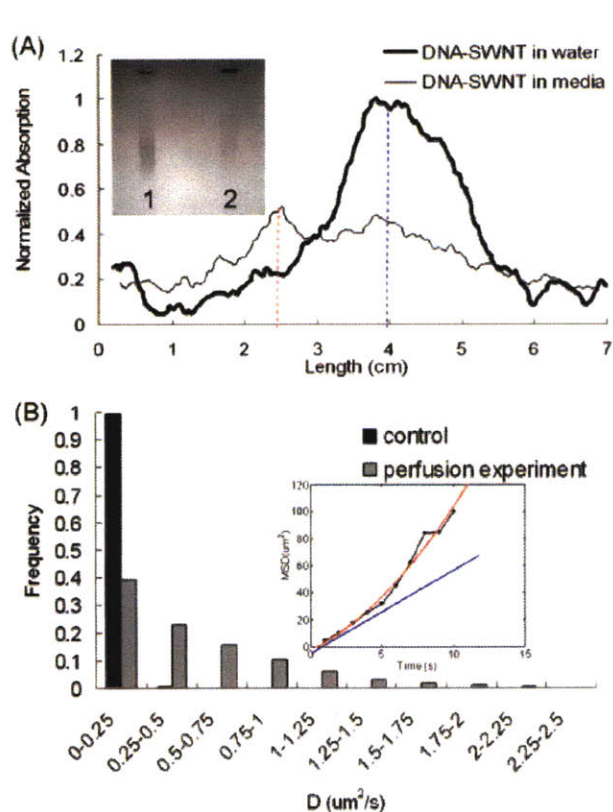
Figure 2.1
(A) A comparison between DNA-SWNT in water (lane 1) and after incubation in DMEM media (lane 2) in a 1 wt % agarose gel in 1x TAE buffer showing decreased migration of the latter, suggesting bound proteins and/or aggregation.
(B) A comparative histogram of D of DNA-SWNT obtained in a flow field (convective) in media on a perfusion stage (gray) with a control in the absence of flow (purely Brownian). Brownian diffusion and convective components can be extracted from each individual MSD-t trace (inset, the red line is the model for the convective diffusion and the blue line is its Brownian component). The magnitude of the Brownian components is in agreement in both experiments (~ 0.25 $\mu m^2/s$), indicating that perfusion does not appreciably affect the morphology of the DNA-SWNT.
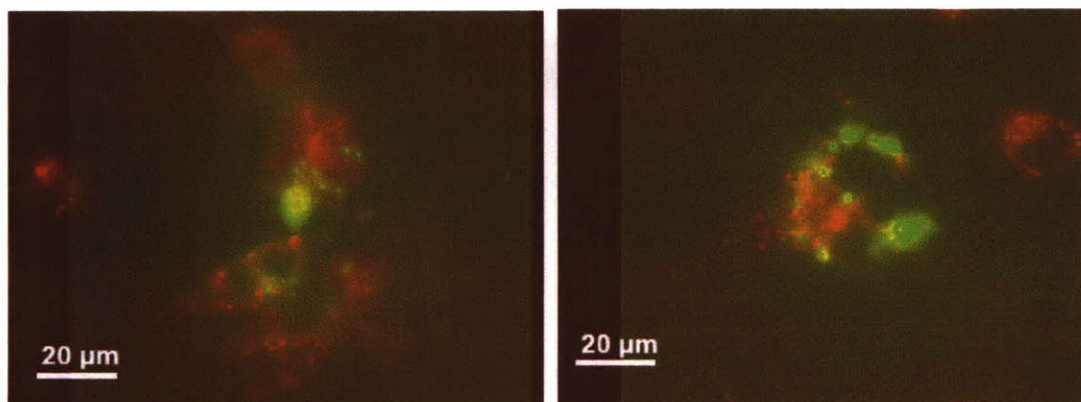
Figure 2.2 Colocalization of nanotube fluorescence (green) in murine 3T3 cells with Lysotracker the lysosomal stain (red) shows overlap, suggesting DNA-SWNT is present in lysosomes.

In order to track SWNT in real time during cellular uptake and intracellular trafficking, we used a variation on an imaging optical microscope for single molecule spectroscopy in the nIR that has appeared previously[51], and equipped it with a temperature controlled perfusion stage. The inlet to the stage allowed for alternate perfusion of standard cell media and media containing 5.0 mg/L of d(GT)$_{15}$-DNA wrapped SWNT (DNA-SWNT) with controlled switching between these solutions. The stage is illuminated via a 785 nm laser at 100 mW power at the source, and nIR collected light is projected onto a 2D InGaAs imaging array after passing through an 840 nm long pass filter (Fig. 2.3). To ensure that the flow field does not alter the colloidal properties of the SWNT, we compared D calculated from the convective transport to quiescent solution under zero flow conditions (Brownian diffusion) as shown in Fig. 2.1B. From the raw data of one example single trajectory, the MSD can be computed, thus D can be obtained, using Eq 2.1 for simple diffusion and Eq 2.3 for convective diffusion.

The mode in the distribution of D for both samples is 0.25 $\mu m^2/s$. The mean value under zero flow is 0.25 $\mu m^2/s$ while the value for the convective case is 0.40 $\mu m^2/s$. The similar values suggest only minor changes in colloidal properties with flow through the stage.
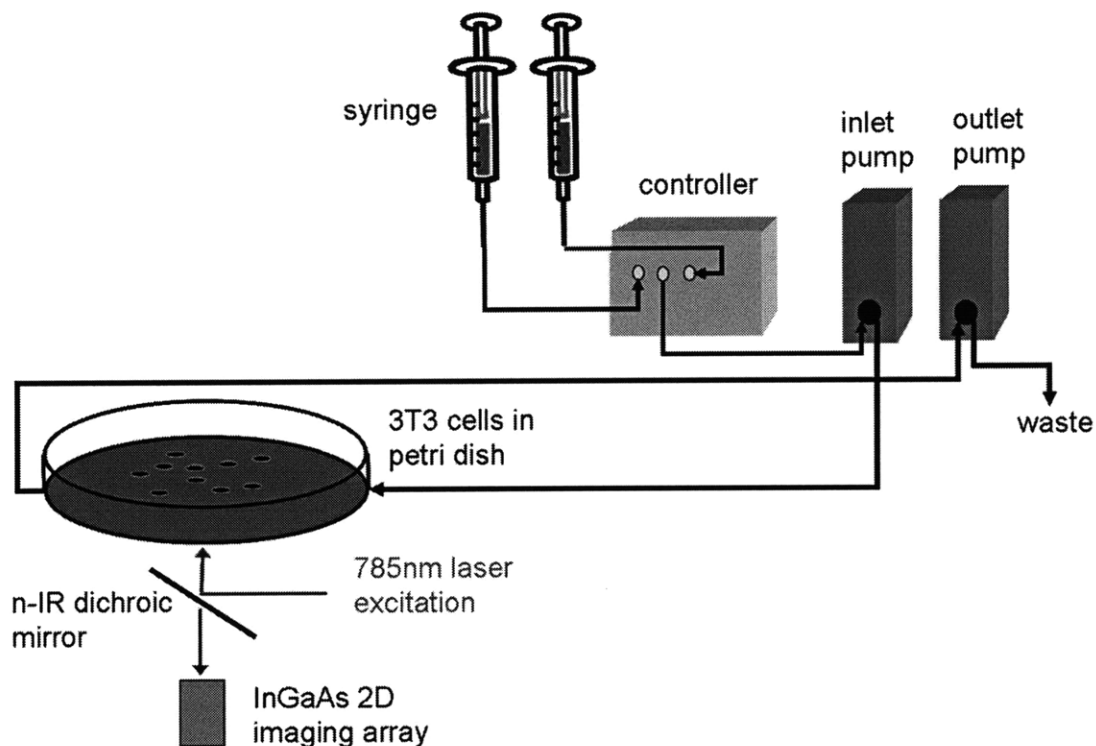
Figure 2.3 Configuration of the inverted microscope with 785 nm laser excitation and 2D InGaAs imaging array with perfusion stage. The inlet to the stage can be rapidly switched between a syringe with cell media, or DNA-SWNT in media

During a typical experiment, two long duration pulses of DNA-SWNT media are perfused onto the stage at the beginning of the experiment producing a bimodal injection that allows for the calculation of uptake rates as described below. At $t = 0$ s, SWNT free media is switched to DNA-SWNT perfused at a constant rate of 5.65 μL/s for 800 seconds. A second pulse of DNA-SWNT is started at $t = 827$ sec for another 173 seconds, after which SWNT free media is perfused at a constant speed of 3.46 μL/s for the duration of the experiment. Imaging is performed at 1 frame/sec for 7515 seconds. To confirm cell viability and correct for potential migration at the start, duration and completion of the experiment, four visible CCD images were collected at $t = 0$ s, $t = 3000$ s, $t = 6000$ s and $t = 7515$ s. Figure 2.4 traces the total integrated intensity of nIR light

23

collected by the InGaAs array with two peaks corresponding to the two perfused pulses of SWNT onto and across the stage.
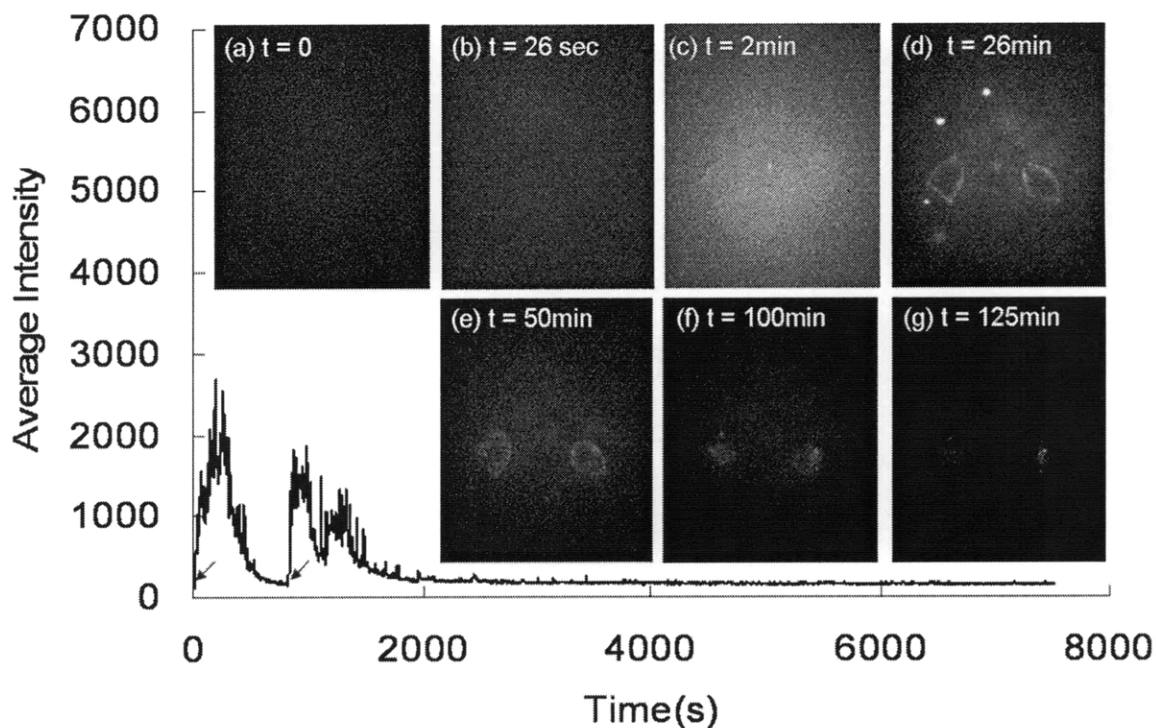
Figure 2.4 A solution of DNA-SWNT in cell media is perfused at t = 0s with 5.65 µL/s for 800s and then at t = 827s for an additional 173 s resulting in a bimodal injection profile. The graph shows the average nIR intensity of the illuminated area, tracing the injection. The insets (a) to (g) are images at various times during the experiment. No fluorescence is observed at t = 0 sec (a). At t = 26 s nIR emission begins to appear (b). SWNT accumulate on the membrane as early as t = 2 min (c). At t = 26 min, SWNT accumulation on the membrane outlines two particular cells (c). Internalization is observed slowly over the course of the experiment (e) and (f) with aggregates moving inward (g).

Included in the inset are images of two isolated cells observed during the perfusion experiment. No nIR image is observed at t = 0 s (Fig. 2.4a) and before the 26 s required for the solution to travel from the syringe to the stage at a speed of 5.65 µL/s. At t = 26 s, background illumination from the SWNT pulse is observable (Fig. 2.4b) with subsequent accumulation on the membrane observed (Fig. 2.4c) at t = 2min. The membrane is clearly outlined at t = 26 min (Fig. 2.4d). Internalization is observed slowly

24

over the duration of the experiment (Fig. 2.4e-f) with aggregates moving inward at later times (Fig. 2.4g). Artifacts associated with the injection itself are ruled out by increasing the flow speed and the time of perfusion to 10 μL/s and 1000 s in subsequent experiments yielding similar results detailed in one of our publications[50]. The imaging plane is focused on the cell cross section, which is equally far to the top and bottom of the cell. The calculated depth of field for imaging through our system is 295 nm while the thickness of cultured 3T3 cells is 5-6μm[52]. The depth of field is calculated for the 63x oil immersion objective (numerical aperture = 1.4) in our experiment and assuming the wavelength to be 1000 nm (a good assumption since we are using CoMoCAT nanotubes) using the equation by Shillaber[53]. Particles that are not in the imaging plane are excluded by the image processing algorithm because light from them is necessarily diffuse with larger radii and lower intensities. Filtering is realized by using a size restriction and an intensity cutoff in the particle detection. Both the depth of field from data collection and the localization accuracy from data analysis indicate that only particles in the focal plane contribute to the data.
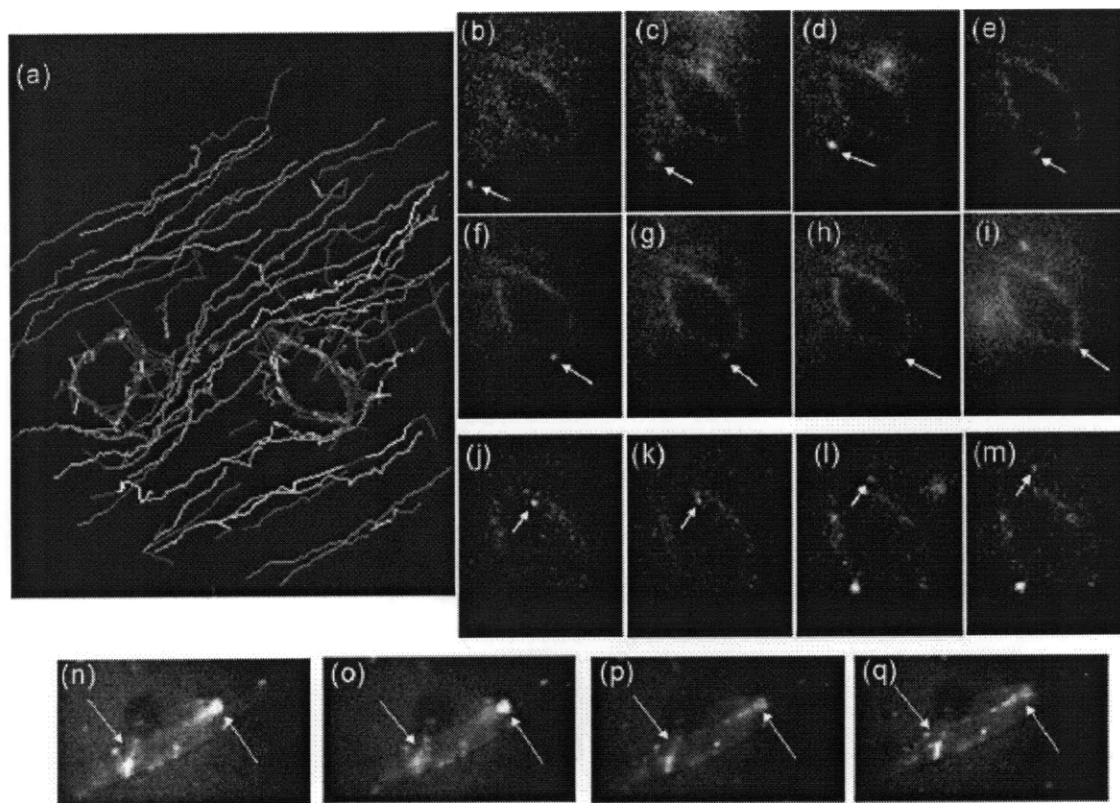
Figure 2.5 (a) A subset of observed trajectories extracted using ParticelTracker. (b-i) Endocytosis (confirmed by MDS feature) of a single particle (arrow) is observed between t = 1029 and 1112 s, identified as receptor-mediated endocytosis. (j-m) Evidence of exocytosis (confirmed by MSD feature) of a single particle (arrow) observed from t = 2218 to 2250 s. (n-q) Aggregation and movement of SWNT inside the cell. The cell is illuminated by the halogen lamp and DNA-SWNT is illuminated by laser at 785 nm.

Using image processing algorithms[54], a total of 10,288 SWNT trajectories are tracked from the sequence of images. A snapshot of the detected trajectories from ImageJ is shown in Fig. 2.5a. Direct proof of endocytosis (Fig. 2.5b-i) and exocytosis (Fig. 2.5j-m) is repeatedly observed from the nIR image sequences, represented as independent trajectories, confirmed by the MSD features of endocytosis and exocytosis. For instance, MSD feature of endocytosis has the signature as presented later in this chapter. By using a halogen illuminator (100W), we can observe the scattering of the cell periphery and the PL signal from DNA-SWNT simultaneously, which allows for

unambiguous classification. An example image sequence of the movement of internalized particles is shown in Fig. 2.5n-q (the dark spot in the middle is from the shade of the light filter). This technique can also verify the overlap between phase contrast cell images and measured trajectories. In order to explain the endocytosis and exocytosis mathematically, recurring events of temporal and spatial coordinates of each particle are then analyzed using an algorithm we have written in Matlab that classifies the transport pathway observed using the starting and ending location of the particle in the trajectory, as well as the functional form of its MSD. Briefly, the coordinates of the particle on the stage relative to the location of the cell membrane, cell interior, and the flow direction along the stage assist in classifying the MSD according to a number of commonly observed pathways. While 5223 trajectories (49.2%) were purely convective diffusion in the flow field with no cellular interaction, the remaining 5065 trajectories (50.8%) demonstrated membrane surface adsorption (6.2%), surface diffusion (18.4%), endocytosis (12.7%), exocytosis (5.9%), desorption (7.4%) or a combination of these behaviors (0.2%). Figure 2.6 superimposes example trajectories recorded in the nIR onto the corresponding optical CCD image of two different cells as an illustration of these classifications.
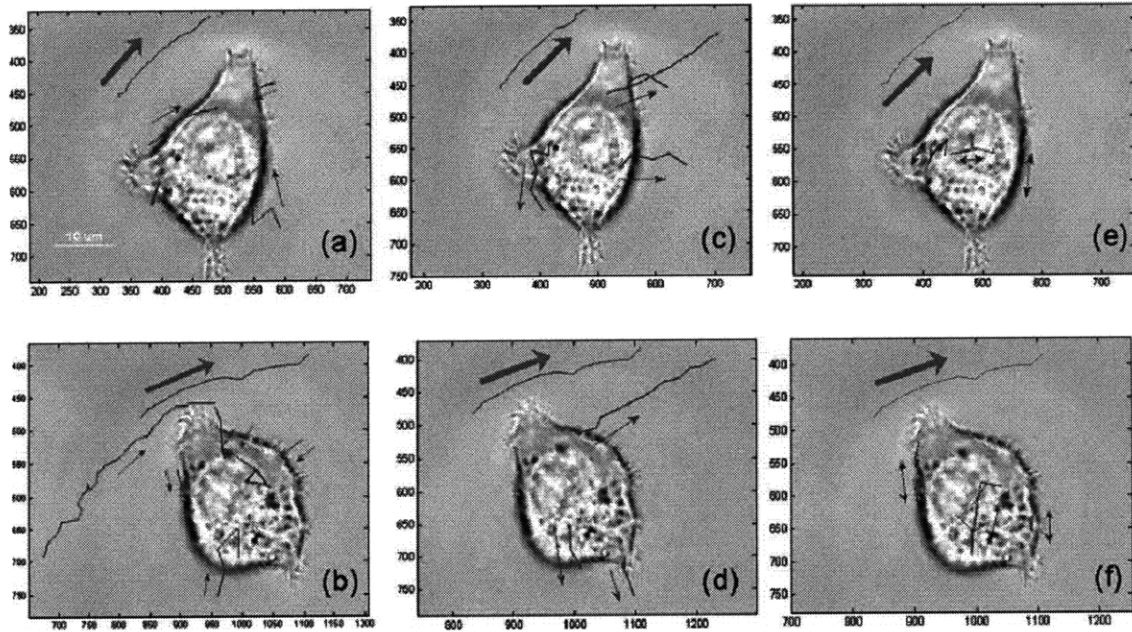
Figure 2.6 Trajectories can be classified into repeatedly observed phenomena. Typical adsorption and endocytosis trajectories are plotted for two different cells in (a) and (b). Exocytosis and desorption trajectories in the same two cells appear in (c) and (d). Confined motion on the membrane and after internalization are depicted in (e) and (f). The thick green arrow in each image indicates the direction of the perfusion flow field.

Figure 2.6a and 2.6b show the adsorption and endocytosis steps while Fig. 2.6c and 2.6d show pathways characteristic of exocytosis and desorption steps. Figure 2.6e and 2.6f are typical of confined diffusion of internalized particles and those observed on the cell membrane (surface diffusion). The transition from convective transport to confined diffusion, coinciding with a localization of the particle from the convective flow outside the cell to the membrane surface, was labeled according to the UC→A pathway (Fig. 2.7).
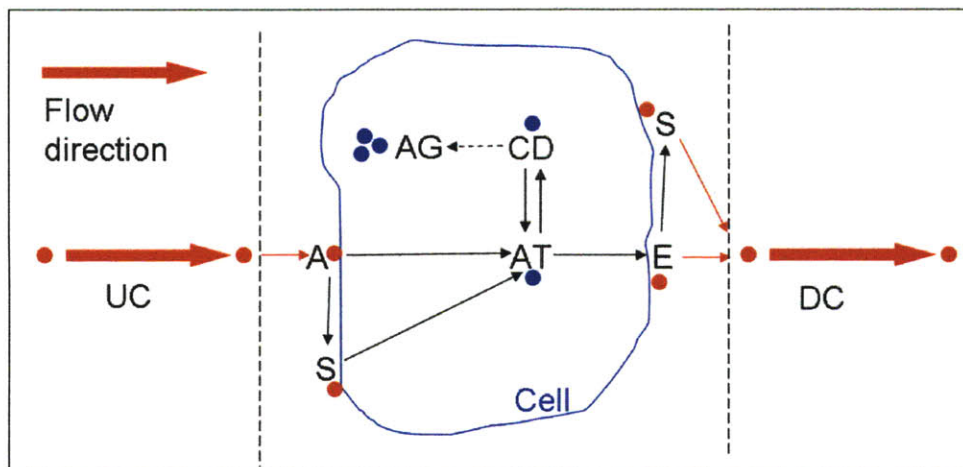
Figure 2.7 The pathways involved in the cellular uptake of carbon nanotubes as reconstructed from single molecule trajectories. The blue line indicates the cell membrane. The blue dots indicate internalized particles. UC = upper stream convective diffusion, A = adsorbed, S = surface diffusion, AT = active transport, CD = confined diffusion, E = externalized, DC = down stream convective diffusion, AG = intracellular aggregation.

Some trajectories observed exclusively within the cell interior transitioned between an activated transport (quadratic MSD) to a confined diffusion and labeled the AT ↔ CD pathway. Table 2.1 summarizes the pathways identified and the sorting criteria for the MSD. All 10,288 trajectories were classified according to one of the 14 pathways in the table.

Table 2.1 Details of the cellular uptake network.

Step Name	Step Name Abbreviation	MSD Equation	Starting Location	Ending Location	Example Graph
upper stream to down stream convective diffusion	UC→DC	Eq. 2.3	outside the cell	outside the cell	Fig.2.8a
upper stream convective diffusion to adsorption	UC→A	Eq. 2.3 Eq. 2.4	outside the cell	cell membrane	Fig.2.8b
adsorption to surface diffusion	A→S	Eq. 2.4	cell membrane	cell membrane	Fig.2.8c
adsorption to active transport	A→AT	Eq. 2.3 Eq.2.4	cell membrane	inside the cell	Fig.2.8d
surface diffusion to active transport	S→AT	Eq. 2.3 Eq.2.4	cell membrane	inside the cell	Fig.2.8d
surface diffusion	S↔S	Eq. 2.4	cell membrane	cell membrane	Fig.2.8c
upper stream to adsorption/surface diffusion to active transport	UC→S(A) →AT	Eq. 2.3 Eq.2.4	outside the cell	inside the cell	Fig.2.8e
active transport to confined diffusion	AT→CD	Eq. 2.3 Eq. 2.4	inside the cell	inside the cell	Fig.2.8f
active transport to externalization	AT→E	Eq. 2.3	inside the cell	cell membrane	Fig.2.8g
confined diffusion to externalization	CD→E	Eq. 2.3 Eq. 2.4	inside the cell	cell membrane	Fig.2.8g
externalization to surface diffusion	E→S	Eq. 2.4	cell membrane	cell membrane	Fig.2.8c
surface diffusion to down stream convective diffusion	S→DC	Eq. 2.4 Eq. 2.3	cell membrane	outside the cell	Fig.2.8h
externalization to down stream convective diffusion	E→DC	Eq. 2.4 Eq. 2.3	cell membrane	outside the cell	Fig.2.8h
active transport/confined diffusion to externalization to down stream convective diffusion	AT(CD)→E→DC	Eq. 2.3 Eq. 2.4	inside the cell	outside the cell	Fig.2.8i

This large data set of observed trajectories, combined with our classification algorithm, allow for the complete pathway of SWNT endocytosis and trafficking within living cells to be constructed for the first time (Fig. 2.7). Some SWNT are adsorbed onto the cell membrane (UC→A, Fig. 2.8b), where they either internalize (A→AT, Fig. 2.8d), or diffuse in a confined manner on the membrane surface (A→S, Fig. 2.8c) followed by internalization (S→AT, Fig. 2.8d).
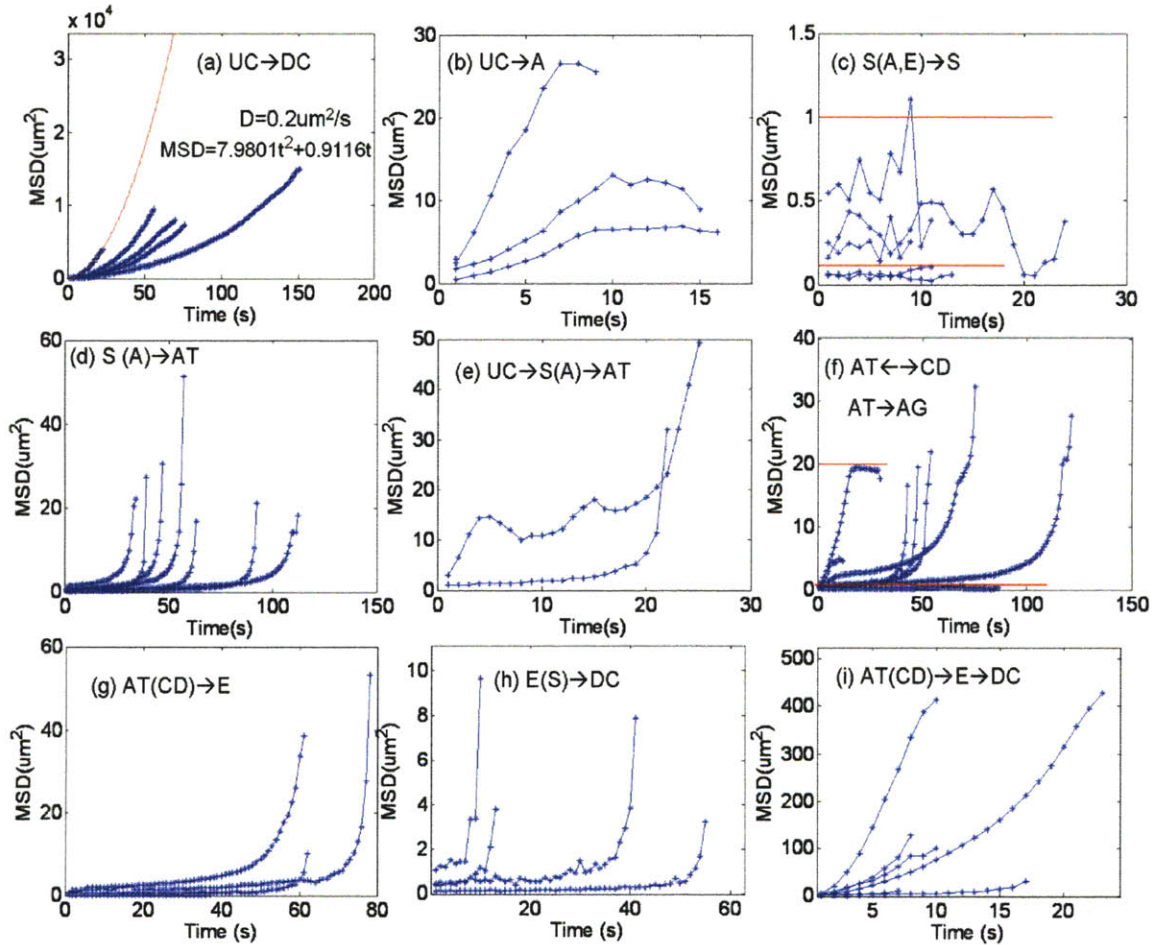
Figure 2.8 Example MSD curves versus time from single particle tracking. In conjunction with the starting and final location of the particle, these curves identify a unique transport pathway.
  (a) Convective diffusion outside the cell;
  (b) Adsorption onto the cell membrane, convective to confined diffusion;
  (c) Confined diffusion on the cell membrane, with a corral size of 0.1-1 μm^2;
  (d) From cell membrane to inside the cell, confined to convective;

31

(e) Endocytosis that is equivalent to the process from (b) to (d);

(f) Two types of motion for the internalized particles: one is confined diffusion with a corral size of 0.1-20 μm^2, the other is convective motion;

(g) Exocytosis;

(h) Desorption from the membrane to the outside;

(i) Exocytosis that is equivalent to the process from (g) to (h).

The MSD curve can be statistically regressed as linear for Brownian diffusion (Eq. 2.1) or quadratic for either convective or active transport with a diffusive component (Eq. 2.3). The equation for corralled or confined motion (Eq. 2.4) allows for the calculation of the corral size C. For instance, convective diffusion outside of the cell is well described by a quadric function as shown in Fig. 2.8a. Regression for one example (in red) yields a diffusion coefficient of 0.2 μm^2/s and a velocity of 2.8 μm/s.

The membrane adsorption usually results in confined diffusion (Fig. 2.8b), as is expected. This membrane confined diffusion (Fig. 2.8c) has a calculated corral size between 0.1-1 μm^2. Diffusion coefficients vary from 0.30 to 2.24 μm^2/s, with an average of 0.37 μm^2/s. Confined lateral diffusion of membrane receptors studies suggest that the plasma membrane is compartmentalized into many small domains 300-600 nm in diameter and 0.04-0.24 μm^2 in area [55], in agreement with our calculations. Note that this implies that specific receptors are involved in cellular internalization of DNA-SWNT.

Once inside of the cell, the confined diffusion (Fig. 2.8f) demonstrates greater variability in corral size of 0.1-20 μm^2. A quadratic (convective-like) diffusion is observed at the start of internalization beginning from the cell membrane (Fig. 2.8d). The MSD for these trajectories can be fit to a quadratic function, yielding a velocity from 0.3 to 2.3 μm/s. The velocity of one motor protein, kinesin, is calculated to be ~0.8 μm/s in microtubules [56]. Similar behavior is reported in the literature for other systems. For

instance, the velocity of the direct motion for adeno-associated viruses (AVV) is found to be between 1.8 and 3.7 μm/s in cytoplasm and 0.2 to 2.8 μm/s within the nuclear area. This was attributed to a microtubule-dependent transport of viruses by motor proteins including kinesin [48]. *In vitro* assays for individual, conventional kinesin motors give a velocity range from 0.6 to 0.8 μm/s [57]. A study of quantum dot-tagged kinesin yields an average velocity of 0.57 ± 0.02 μm/s [58]. The consistency between the data and the literature suggests that motor proteins are involved and thus results in the observation of convective diffusion. Similar explanation can be made for the convective diffusion observed in Fig. 2.8e, f, g and i. For the convective diffusion observed in desorption (Fig. 2.8h), it is clearly caused by the flow field.

Of the particles that are internalized, a fraction exhibit confined diffusion (AT↔CD, Fig. 2.8f), while some are clearly externalized (AT→E, Fig. 2.8g). The confined diffusion of particles either results in externalization (CD→E, Fig. 2.8g), or aggregation and remain internalized [59]. The externalized particles are either translated down-stream directly (E→DC, Fig. 2.8h) or confined to the cell membrane (E→S, Fig. 2.8c) for a period followed by down stream translation (convection) (S→DC, Fig. 2.8h). Sometimes the internalization or externalization process happens so quickly that the time the particles spend on the membrane is negligible, resulting a combination of several steps together (Fig. 2.8e, f).

With our direct observation of endocytosis and the associated receptor-involved, active transport analysis, together with several studies on similar nanoparticle systems [28,32-34], we propose the mechanism to be receptor-mediated endocytosis for our system. However, there is a dearth of literature on nanoparticle exocytosis. Only recently has it

been found that for Au nanoparticles exocytosis exhibits a linear relationship to their size, with the larger particles less likely to be exocytosed [32]. We note that a similar relationship between exocytosis rate and size can explain the aggregation observed in this work. As SWNT are tethered or agglomerated within the cell, their size should reduce the exocytosis rate, resulting in an apparent accumulation. We note here that endocytosis and exocytosis are observed throughout the experiment, meaning that cells can actively take up and expel particles. This again, confirms the cell viability, which is consistent with our experimental result from live/dead assay (Fig. 2.9), where DNA-SWNT is non-cytotoxic to three different cell types (3T3, HeLa and A431) with the typical concentration used in this study (5mg/L, ~10 nM if assuming each nanotube has 40,000 carbon atoms).
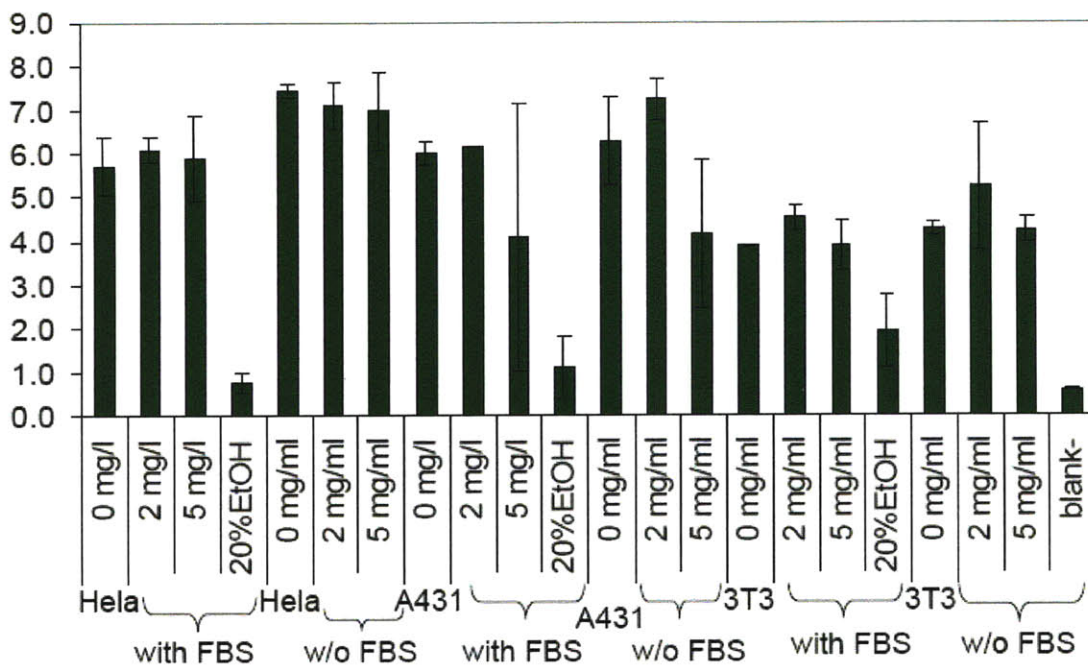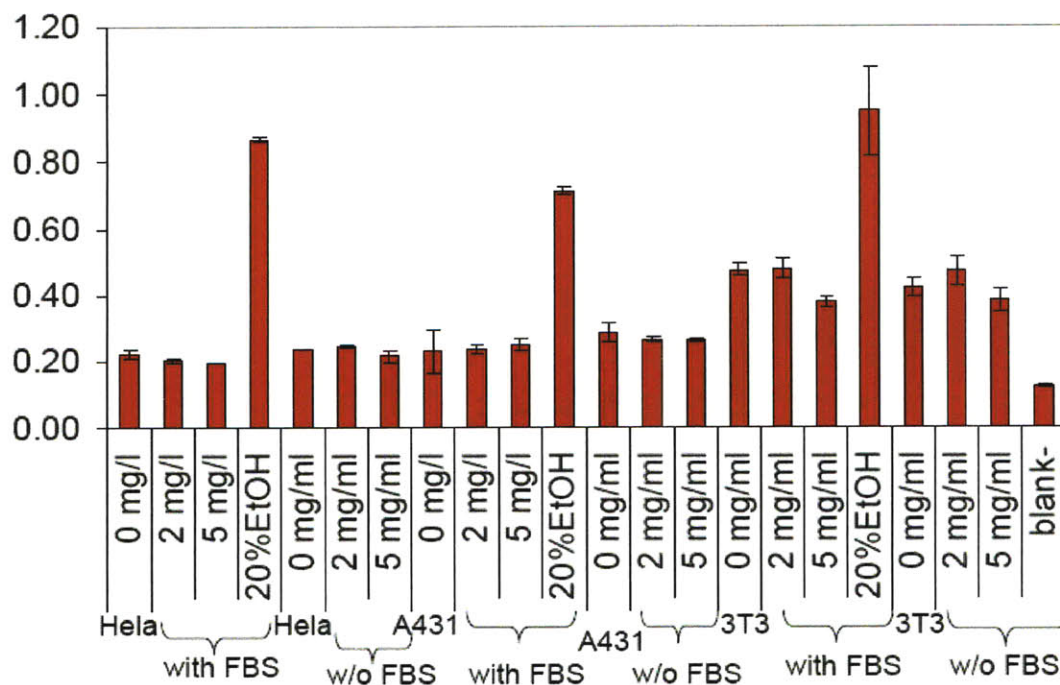
Figure 2.9 Live/dead assay of DNA-SWNT of a concentration up to 5mg/L across three different cell types.

This work provides the first clear evidence for an active exocytosis pathway, suspected to be non-existent for nanoparticles as an explanation for the consistency of observed aggregates for many nanoparticle systems [60]. The existence of exocytosis explains why nanotubes are non-cytotoxic and forms the basis for their biological applications which will be detailed in Chapter 4. The rates of cellular endocytosis and exocytosis were computed by summing the observed trajectories over time and the results are plotted in Fig. 2.10.
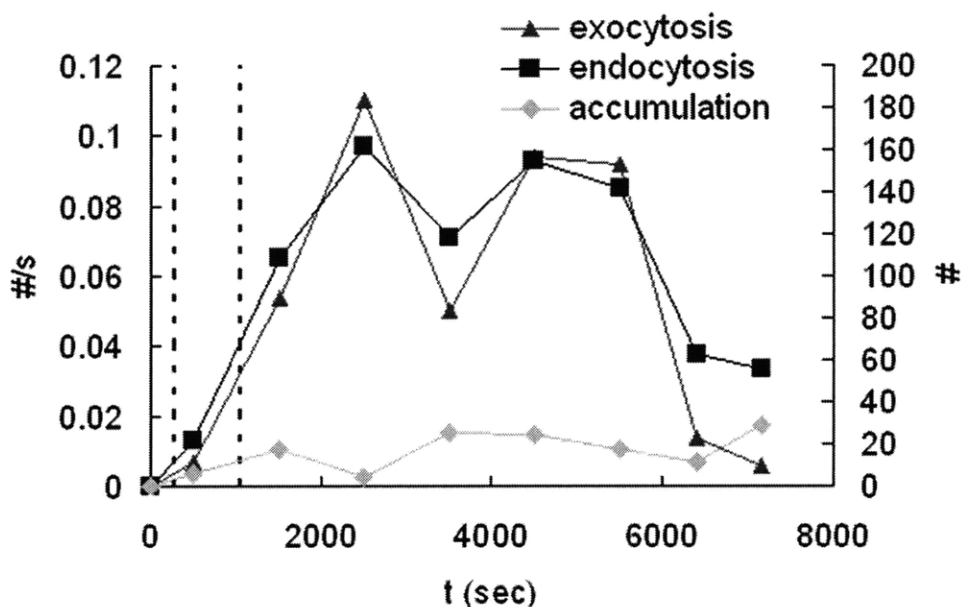
Figure 2.10 Endocytosis, exocytosis rate (#/s) and accumulation (#) over time as compiled from single particle tracking. Two peaks are observed in response to the bimodal injections (dotted lines), although they are shifted in time by ~1200s. The two dotted lines show the peaks of the injections. Cellular endocytosis and exocytosis rates for nanoparticles are closely regulated.

The bimodal nature of the pulsed injections is preserved in the transient rates of endocytosis and exocytosis. The bimodal response is shifted in time from the initial injection, resulting in an average lifetime of SWNT in the cell as 0.09 sec/cell. Here, the sparsely populated cells on the stage at a density of 1.4×10^{-4} cells/μm^2 act to broaden the

injected pulse by successive endocytosis and exocytosis of SWNT from cell to cell. The rates of endocyctosis and exocytosis are found to be closely monitored and regulated by the cell itself. This is completely expected based upon the well-known mechanism for the recycling of cell membrane receptors involved in internalization [61]. The uptake rate is closely related to the rate at which recycled receptors can be re-displayed on the surface via an exocytosis path. It is clear that the endocytosis rate is highest initially, but the excytosis rate is closely matched with a negligible temporal offset. The accumulation is nearly constant in time, a representative of a small fraction of SWNT processed by the cell.

2.2 Size-Dependent Uptake of Nanoparticles

2.2.1 Introduction

Theoretical progress has been made in understanding how the geometry of a nanoparticle can potentially influence its endocytosis rate. However a quantitative description remains elusive with some key aspects unexplained. Gao and co-workers[62] used a thermodynamic and mechanic analysis derived by Freund and Lin[63] to estimate the receptor-mediated endocytosis (RME) rate of a nanoparticle. Briefly, in the process of RME of nanoparticles, receptors binding to the curved nanoparticle surfaces causes membrane curvature with a corresponding increase in elastic energy. On the other hand, this receptor-ligand binding also causes configurational entropy to be reduced from the immobilization of the receptors. Meanwhile, receptors can diffuse to the wrapping site driven by the local reduction in free energy, allowing the complete membrane wrapping around the particle (endocytosis). Decuzzi and Ferrari[64,65] generalized this approach to include the contribution of non-specific forces such as electrostatics arising at the cell-

nanoparticle interface. All existing models to date predict a threshold radius below which nanoparticle uptake by RME is impossible, and a highly asymmetric distribution of rates that decrease as nanoparticle diameter increases. Experimentally, the distribution is instead highly symmetric for both Au nanoparticles in the literature[32,33] and DNA-SWNT, as we have demonstrated for the first time in this work. Moreover, there is relatively little quantitative data or predictive modeling of the dynamics of nanoparticle trafficking into mammalian cells, despite significant progress in the quantitative description of endocytosis for small molecule ligands[61,66].

In this section, we have developed the first quantitative model capable of relating the RME rate of spherical and anisotropic nanoparticles to their geometry and predict important aspects of their trafficking dynamics. We provide indirect evidence that nanoparticle surface clustering on the external cellular membrane facilitates RME by lowering the otherwise prohibitive thermodynamic barrier. The formalism explains why particles with a radius smaller than 25 nm can be endocytosed in this manner, a fact not explained by previously developed models. We validate the model experimentally for d(GT)$_{15}$ wrapped SWNT of controlled lengths ranging from 130±18 nm to 660±40 nm and show that the mechanism accurately describes data for SWNT in this work and also for Au nanoparticles with diameters from 14 to 100 nm[32,33]. Also consistent with our model is the recent study which shows that the changes in nanoparticle size affect the binding capacity of antibody coated Au nanoparticles with receptors[67]. The model is also the first to quantitatively describe the dynamics of nanoparticle uptake and trafficking, as we demonstrate for the aforementioned SWNT using SPT. All three nanoparticle types (Au, SWNT and PLGA) show that recycling (exocytosis) rate constants calculated from

the model are similar in magnitude, which are more related to the membrane turnover rate constant.

2.2.2 Experimental Results, Model Derivation and Validation

While size-dependent cellular uptake studies of spherical particles have been performed for citrate-coated Au nanoparticles[32,33], these studies have not been fully explored for highly anisotropic particles after the first study of SWNT length and cellular uptake[68]. Chan and co-workers[32,33] reported that the maximum uptake in HeLa cells occurs with 50 nm diameter Au nanoparticles after a 6 hr incubation.

We use d(GT)$_{15}$ wrapped SWNT with a high aspect ratio to directly study the length effect on cellular uptake using well-characterized platform employed in several of our previous studies[8,14,19,69] and others' studies[21,34,70]. The length separation procedure is detailed in Appendix B. To obtain the uptake for different lengths, we used an altered imaging optical microscope for SPT in the nIR with a perfusion stage as described in the previous section[50]. During a typical experiment, a steady flow of cell media, Dulbecco's Modified Eagle's Medium (DMEM), is established followed by a pulse of 0.025 mg of perfused DNA-SWNT in media. In order to compare the difference in the uptake, the concentration of SWNT (5mg/L), the total volume of SWNT (5mL) and the perfusion speed (5.65 μL/s) are kept constant. We note that the amount of SWNT for different lengths is magnitudes greater than the available receptors on the cell membrane so we could consider SWNT to be in excess. Because SWNT do not photobleach, we are able to track their fluorescence trajectories relative to the cell for up to 6 hr. Figure 2.11 shows the co-localization of the fluorescence of SWNT (green) with the cell image at the end of each experiment. As shown in the figure, long (Fig. 2.11a, 660 ± 40 nm) and short

(Fig. 2.11d, 130 ± 18 nm) SWNT have lower fluorescent intensities than SWNT with an average length of 430 ± 35 nm (Fig. 2.11b) and 320 ± 30 nm (Fig. 2.11c). The 320 nm length SWNT have the highest uptake even if one corrects for the length dependent quantum yield. The SWNT quantum yield has been shown to increase with length[69]. If a correction is applied[59], 320 nm remains the maximum.

Endocytosis and exocytosis are dynamically regulated for SWNT,[50] and the corrected intensity therefore reflects only the accumulation difference for different lengths. The exocytosis rate can be decoupled from the nanoparticle net accumulation data via separate parallel experiments, as recently reported for Au nanoparticles.[32] Alternatively, the ability to track and compile statistics on single SWNT in real-time allows for a direct measurement of the endocytosis rate using SPT. Briefly, trajectories of non-photobleaching SWNT are extracted using ImageJ and the ParticleTracker plugin.[54] Endocytosis and exocytosis events are documented in real-time using a Matlab script.[50]
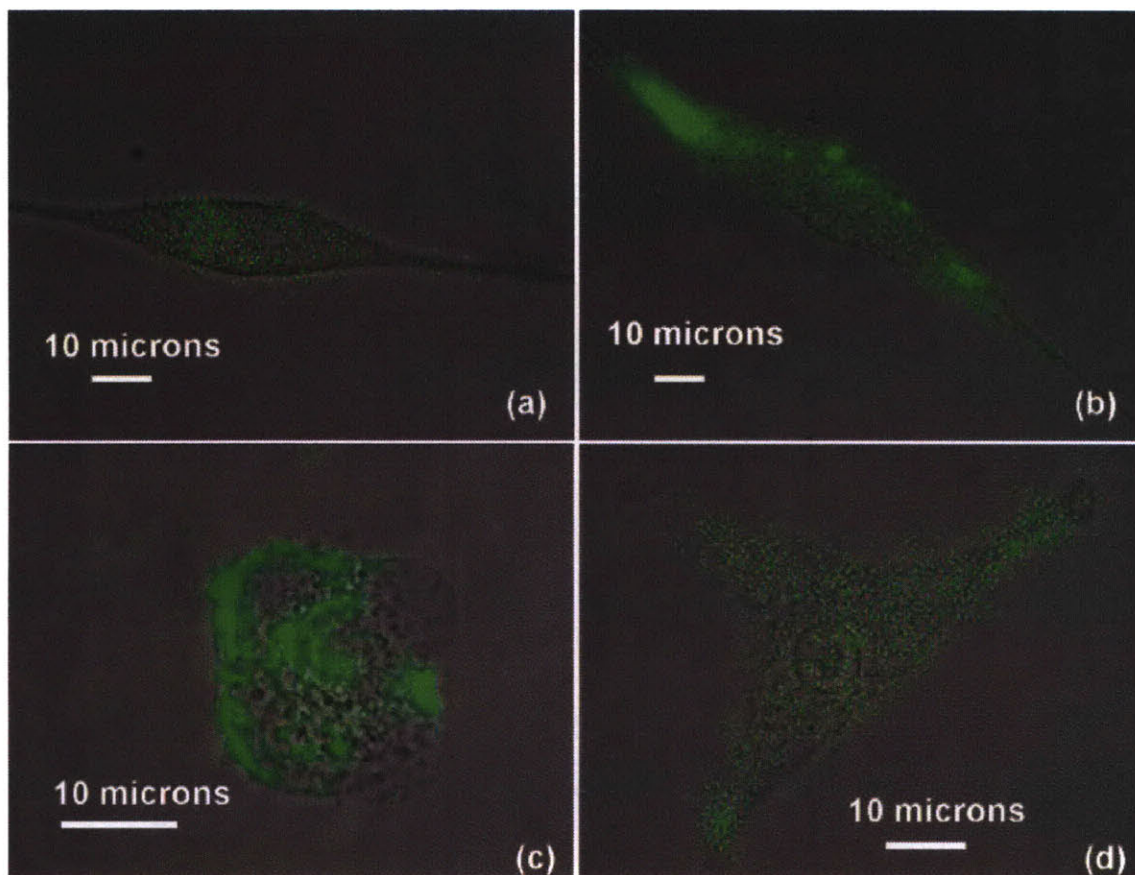
Figure 2.11 Colocalization of the fluorescence from SWNT (green) with its corresponding cell image at the final stage of the experiment for the four different lengths: (a) 660 ± 40, (b) 430 ± 35, (c) 320 ± 30, and (d) 130 ± 18 nm.

The rates of internalization and recycling of membrane receptor-bound low molecular weight ligands can be described by a variety of kinetic network models[61,66] that approximate the rate of transport between various cellular compartments. Experimental work has confirmed that such networks (Fig. 2.12a) accurately predict the dynamics of cellular endocytosis of small molecules and proteins, the mechanism of which is not restricted to RME; however their application to nanoparticle trafficking has not yet been explored. We propose that nanoparticles bound to membrane receptors initially follow similar trafficking mechanisms (Fig. 2.12b). Our interest is only in those pathways that dominate the observable rates of uptake and expulsion, and therefore we neglect less

important details of the endocytosis process. The unbound, protein coated nanoparticles of concentration, L, adsorb via cell membrane surface receptors of density, Rs, to the membrane with kf and kr as forward and reverse adsorption rate constants, respectively, creating a concentration, Cs, at the membrane surface.   With rate constant, ke, the adsorbed particle can be internalized into an endosome with cellular concentration Ci. As we have demonstrated directly for the first time for SWNT[50], in this scheme the nanoparticle either accumulates inside the cells or is recycled back to the membrane with rate constant krec. Membrane receptors are also recycled to the cell surface.
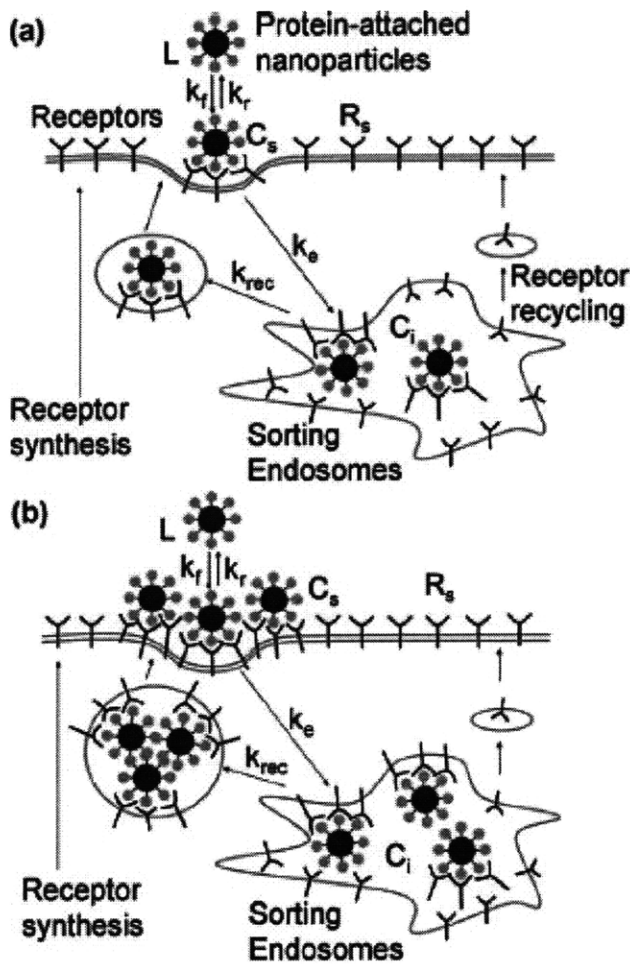
Figure 2.12 An illustration of endocytosis, trafficking and exocytosis steps in the model for (a) single nanoparticle and (b) nanoparticle clusters. Nanoparticles with an extracellular concentration of L can reversibly bind to free surface receptors (R_s) with binding and dissociation rate constant of k_f and k_r respectively and form nanoparticle-receptor complexes on the membrane with a concentration of C_s. These complexes can be endocytosed with a rate constant of k_e. A fraction of the internalized nanoparticle-receptor complexes (C_i) can be recycled back to the plasma membrane with a rate constant of k_{rec}. Other factors, such as the recycling and synthesis of the free receptors, do not affect L, C_i and C_s and thus will not be discussed in this model.

42

In our model, we assert that nanoparticles first reversibly adsorb to the plasma membrane and form receptor-bound complexes capable of membrane surface diffusion (Fig. 2.12b). This process invariably causes clusters of sufficient size to lower the elastic energy required for wrapping so it can be overcome by the free energy reduction associated with receptor-particle binding, driving the diffusion of receptors for internalization[62-65] as detailed previously. This is consistent with the experimental data for SWNT in this work and those published previously for Au nanoparticles,[32,33] where internalization of smaller particles far below the predicted threshold optimum is significant. Moreover, this assumption is also consistent with a distinct increase in the nIR fluorescence from SWNT concentrated at the external cell membrane during the early stages of the transient uptake experiment (Fig. 2.13). The illuminated exterior of the cell from adsorbed nanotubes is magnitudes higher than a single nanotube. To get this larger intensity, in a diffraction limited spot, it is highly possible that the nanotubes distribute or pack in a cluster.
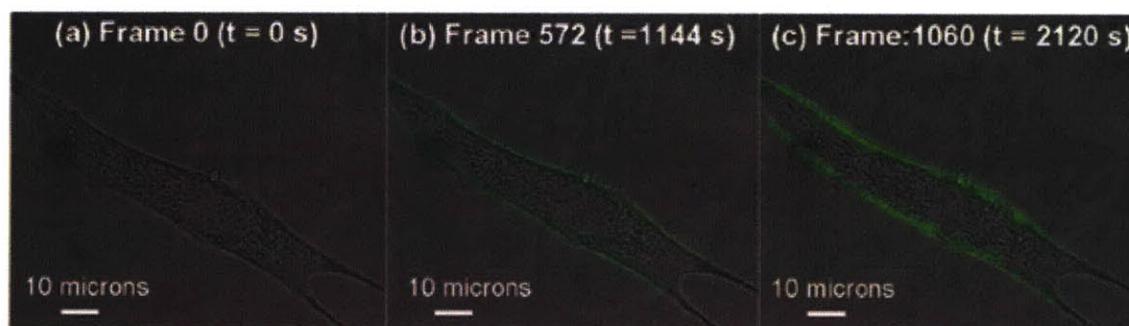
Figure 2.13 Experimental observation of SWNT surface clustering on the cell membrane (430 ± 35 nm SWNT is shown as an example). The fluorescence of SWNT indicated by green is projected onto the corresponding phase contrast image of the cell. (a) At the beginning of the experiment (t = 0s), there is no SWNT present; (b) a thin layer of SWNT adsorption of the cell membrane is observed at t = 1144 s; (c) this layer becomes denser at t = 2120 s, indicating the existence of surface clustering.

The thermodynamic aspects of size-dependent RME have been addressed previously[62,63]. We instead focus on complex formation at the membrane surface in the following derivation. Consider two spherical nanoparticle complexes A and B in this process. The diffusion-controlled association rate constant is calculated to be [71,72]

$$k = 2\pi \lambda (D_A + D_B)(R_A + R_B) \quad \text{(Eq. 2.5)}$$

where D_A and D_B are the surface diffusion constants for A and B respectively, and R_A and R_B are the radii of particles A and B respectively. In Eq. 2.5, λ is calculated as [72]

$$\lambda = \frac{\gamma K_1(\gamma(R_A + R_B))}{K_0(\gamma(R_A + R_B))}$$

where γ is the inverse of half the average distance traveled by a reactant molecule in the time before desorption and K_0 and K_1 are the modified Bessel functions of the second kind.

For cylindrical molecules such as carbon nanotubes, references 71 and 73 provide an effective capture radius R^* defined by:

$$R^* = a / \ln(2a/b) \quad \text{(Eq. 2.6)}$$

where a and b are the major and minor semi-axes of the cylinder[71,73]. Remarkably, when this effective capture radius is used for carbon nanotubes, their relative uptake becomes nearly identical to Au nanoparticles, indicating its importance as an effective scaling metric.

The extracellular nanoparticles can reversibly adsorb onto the membrane. Adsorbed complexes (protein coated SWNT or protein coated Au NP) diffuse on the cell membrane surface and form clusters with a radius of sufficient size that eventually satisfy the thermodynamic requirement for endocytosis[62]. This process is described as follows:

$$A(\text{extracellular}) \xrightleftharpoons[k_{-1}]{k_1} A_1$$

$$A_1 + A_1 \xrightleftharpoons[k_{-2}]{k_2} A_2$$

$$A_2 + A_1 \xrightleftharpoons[k_{-3}]{k_3} A_3$$

$$A_3 + A_1 \xrightleftharpoons[k_{-4}]{k_4} A_4$$

...

$$A_i + A_1 \xrightleftharpoons[k_{-(i+1)}]{k_{i+1}} A_{i+1}$$

$$A_i \xrightleftharpoons[krec(Ri)]{ke(Ri)} A_i(\text{endocytosed})$$
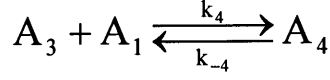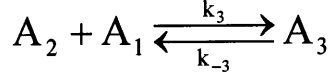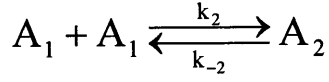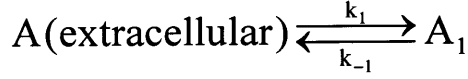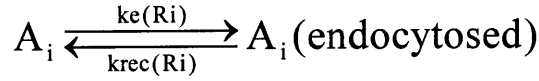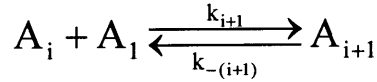
where A(extracellular) represents the nanoparticle in the bulk during experiments; A_1 represents single nanoparticle-receptor complex and Ai represents a cluster formed by i such singlets. The endocytosis and recycling rate constant is represented by ke(Ri) and krec(Ri) for clusters of radius Ri. We assume that the concentration of A_1 is constant because of the extracellular reservoir of A. The population of Ai changes according to:

$$[A_1] \approx \text{constant}$$

$$\frac{d[A_i]}{dt} = k_i \cdot [A_1] \cdot [A_{i-1}] + k_{-(i+1)} \cdot [A_{i+1}] + k_{rec}(R_i) \cdot [A_i(\text{endocytosed})]$$
$$- (k_{i+1} \cdot [A_1] \cdot [A_i] + k_{-i} \cdot [A_i] + k_e(R_i) \cdot [A_i]) \quad \text{for} \quad i = 2,3,4...$$

where [Ai] is the concentration of Ai. The endocytosis and recycling process is much slower compared to the clustering process, so at early time,

$$\frac{d[A_i]}{dt} = k_i \cdot [A_1] \cdot [A_{i-1}] + k_{-(i+1)} \cdot [A_{i+1}]$$
$$- (k_{i+1} \cdot [A_1] \cdot [A_i] + k_{-i} \cdot [A_i]) \quad \text{for} \quad i = 2,3,4...$$

At the early stage of the clustering process, the clustering rate is much larger than the reverse rate, so

$$\frac{d[A_i]}{dt} = k_i \cdot [A_1] \cdot [A_{i-1}] - k_{i+1} \cdot [A_1] \cdot [A_i] \qquad \text{for} \quad i = 2, 3, 4...$$

As this process advances, pseudo-equilibrium is reached for the clusters of radius Ri as long as larger clusters are permitted to form:

$$[A_i] = \frac{k_2}{k_{i+1}}[A_1] \qquad \text{for} \quad i = 2, 3, 4...$$

These assumptions simplify the problem mathematically and allow us to solve for [Ai] given the complication of Eq. 2.5. The corresponding association rate constants are calculated as (via Eq. 2.5):

$$k_i = 2\pi \cdot \lambda(iR, \gamma) \cdot 2D \cdot iR$$

Neglecting the small change in γ and knowing that $K_0(\gamma \cdot iR)/K_1(\gamma \cdot iR) \sim 1$,

One obtains:

$$[A_i] = \frac{2}{i+1}[A_1]$$

The total endocytosis rate can then be expressed as:

$$r = \sum_{i=1}^{\infty}[A_i] \cdot k_e(R_i) = \sum_{i=1}^{\infty}\frac{2[A_1]}{i+1} \cdot k_e(R_i) \qquad (\text{Eq. 2.7})$$

or for the clusters of radius Ri, the endocytosis rate is:

$$r_i = \frac{2[A_1]}{i+1} \cdot k_e(R_i)$$

We use the unmodified intrinsic endocytosis rate constant, k_e, from Gao and co-workers[62] to describe uptake of a cluster of radius R_i. It should be noted that Eq. 2.7 requires no additional parameter estimation and introduces only known or measurable parameters. Experimentally, the observed endocytosis rate constant can be obtained

46

directly from transient nanoparticle uptake data as a function of time and incubation concentration as detailed in Appendix C for comparison and validation of Eq.2.7.
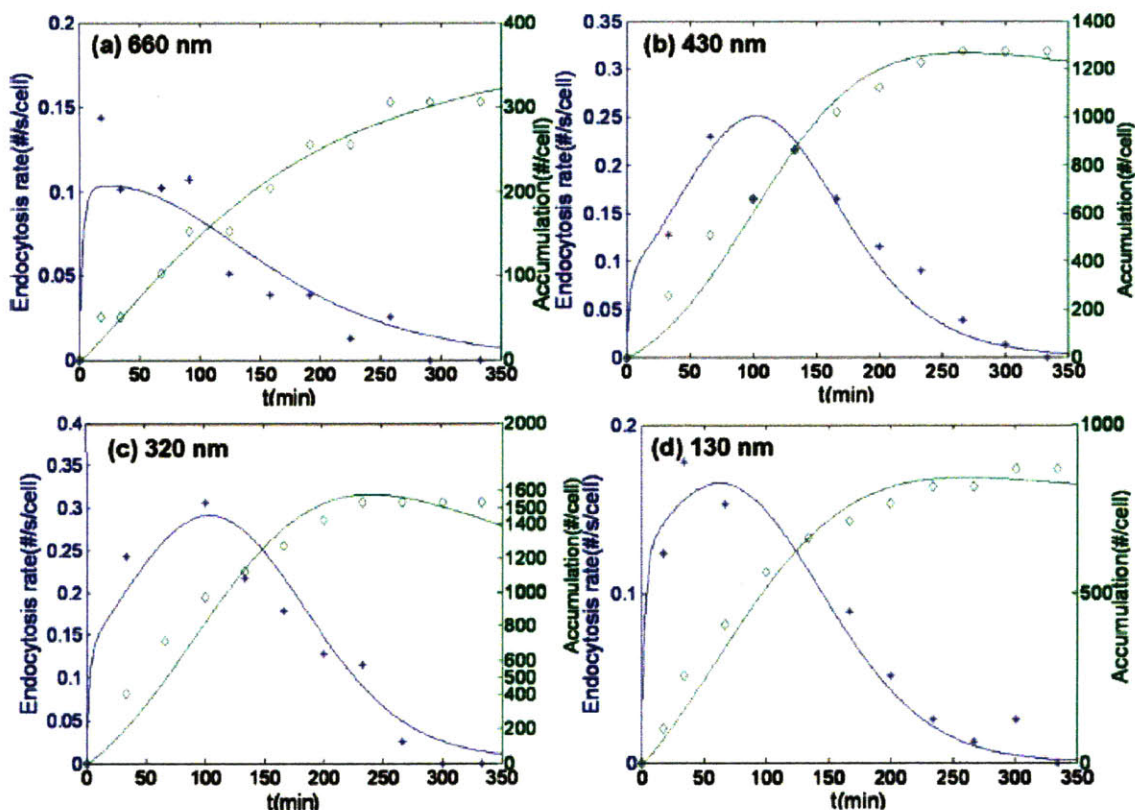
Figure 2.14 Endocytosis rate (#/s/cell, blue) and accumulation (#/cell, green) of DNA-SWNT complexes are solved numerically in real-time for SWNT of length (a) 660 ± 40 nm, (b) 430 ± 35 nm, (c) 320 ± 30 nm and (d) 130 ± 18 nm respectively. The endocytosis rate and accumulation data obtained by SPT is shown in blue diamonds and empty green diamonds. The results obtained using the parameter values of $k_a = 7 \times 10^{-4}$ min^{-1} and $k_r = 0.34$ min^{-1} are summarized in Table 2.2.

We model the dynamics of SWNT uptake quantitatively for the four different lengths in Fig. 2.14. As with Au nanoparticles in the literature[32,33], there is a maximum rate observed except for SWNT, it occurs at 320 nm length. We note that the effective capture radius for SWNT of this size is 26.4 nm, which is very close to the 25 nm radius reported for maximum update of Au nanoparticles[32,33]. Further, our model describes the equilibrium cellular uptake as a function of the size for both Au nanoparticles and DNA-

SWNT (Fig. 2.15). The calculations for SWNT are shown in Fig. 2.15a with contributions from clusters varying from singlets (A_1) to quintuplets (A_5) as example curves compared to the summation model distribution. As seen in Fig. 2.15b, the model can accurately predict the experimental trends observed for the uptake of both Au nanoparticles and SWNT. Here, we have assumed a Gaussian distribution of energies for the nanoparticle-receptor bond (e_{RL}) and the excess binding energy (e_c) with a mean of 15(k_BT) for $e_{RL} + e_c{}^{62}$ and a standard deviation of 12(k_BT). The ratio ($\tilde{\xi}$) of the initial receptor density on the membrane to the receptor density at the nanoparticle-receptor contact area[62] was estimated at 0.01. In the SPT experiments, the initial SWNT concentration is 5mg/L. The cell density is 1.4×10^{-4} cells/μm^2, hence L_0 is 4.5×10^7 /cells. Values for kr, kf depend on the type of ligand attached (intentionally or otherwise) to the nanoparticles and their corresponding receptors on the membrane. Both quantities can be estimated from the literature[66]. The estimates for kr and kf are 0.34 min^{-1} and 7.2×10^7 M^{-1} min^{-1} respectively, and ka is 7×10^{-4} min^{-1} from a receptor concentration of 10^5/cell and a cell density of 6×10^7 cell/L. Our model is used to fit the cellular uptake quantitatively for SWNT of different length and the results are shown in Fig. 2.15 and Table 2.2a. The confidence interval is 95% throughout this work.

(a) 3500

1: singlet (R)
2: doublet (2R)
3: triplet (2.155R)
4: quadruplet (2.414R)
5: quintuplet (3R)
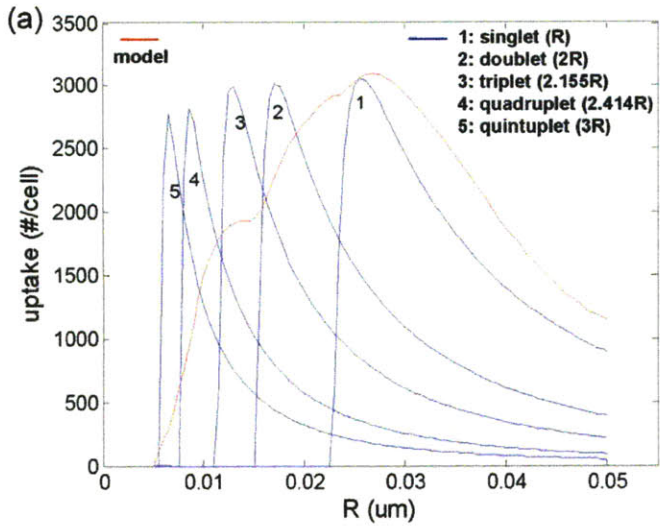
Figure 2.15

(a) The symmetric size-dependent uptake curve (red) in this model (Eq.2.7) is obtained by adding up the contributions from clusters of different sizes (singlets, doublets, triplets, etc.) shown in blue curves. The calculations of SWNT are shown here as an example.
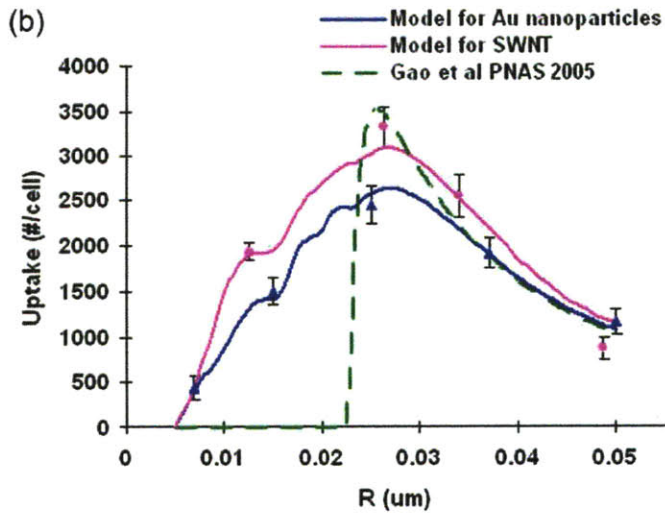
(b) The uptake of Au nanoparticles (blue) and DNA-SWNT (pink) of different sizes are described by the model (Eq.2.7) and compared to the model prediction in Ref [62].

Table 2.2

Model parameter regression for the endocytosis rate constant (ke) and recycling rate constant (krec) of (a) DNA-SWNT with lengths from 130 nm to 660 nm, (b) Au nanoparticles with diameter 14 nm, 50 nm and 74 nm, (c) Au nanoparticles with diameters from 14 nm to 100 nm in media (serum protein coating) and in transferrin (transferrin coating) and (d) PLGA nanoparticles with a diameter of 97 ± 3 nm.

a. DNA-SWNT (this work)				
	130 ± 18 nm	320 ± 30 nm	430 ± 35 nm	660 ± 40 nm
k_e ($\times 10^{-3}$ min^{-1})	13.6 ± 1.0	28.2 ± 1.9	17.7 ± 1.3	5.5 ± 0.4
k_{rec} (min^{-1})	0.0010 ± 0.0001	0.0008 ± 0.0001	0.0006 ± 0.0001	0.0002 ± 0.00003

b. Au nanoparticles [33]			
	14 nm	50 nm	74 nm
k_e ($\times 10^{-6}$ min^{-1})	3.57 ± 0.76	4.53 ± 0.85	2.20 ± 0.34
k_{rec} (min^{-1})	0.0069 ± 0.0020	0.0055 ± 0.0014	0.0054 ± 0.0012

c. Au nanoparticles [33]					
	14 nm	30 nm	50 nm	74 nm	100 nm
k_e ($\times 10^{-6}$ min^{-1}) media	2.61	3.45	4.21	2.76	1.14
k_e ($\times 10^{-6}$ min^{-1}) transferrin	2.76	3.83	5.91	3.44	8.75
k_{rec} (min^{-1}) both	0.0069	0.006	0.0055	0.0054	0.0050

d. PLGA nanoparticles [41]				
k_e ($\times 10^{-4}$ min^{-1})	6.13 ± 1.07		k_{rec} (min^{-1})	0.0073 ± 0.0020

For Au nanoparticles, L_0 is the extracellular concentration of free nanoparticles at t = 0 and is estimated to be 10 μM [33], that is 10^7 /cell given a confluent cell density of 10^{11} cells/L. The average estimate for kr and kf is 0.34 min^{-1} and 7.2×10^7 M^{-1} min^{-1}

respectively. Thus ka can be estimated as 1.196 min^{-1} from a receptor concentration of 10^5/cell [66] and a cell density of 10^{11} cell/L. Specifically when transferrin functions as the ligand, the estimate for kr and kf is 0.1 min^{-1} and 3×10^6 M^{-1} min^{-1} respectively[66]. Transferrin receptor density is 5×10^4 /cell so the calculated ka is 0.025 min^{-1}. ke and krec are obtained via non-linear regression. The fitting result is summarized in Fig. 2.16 and Table 2.2b.
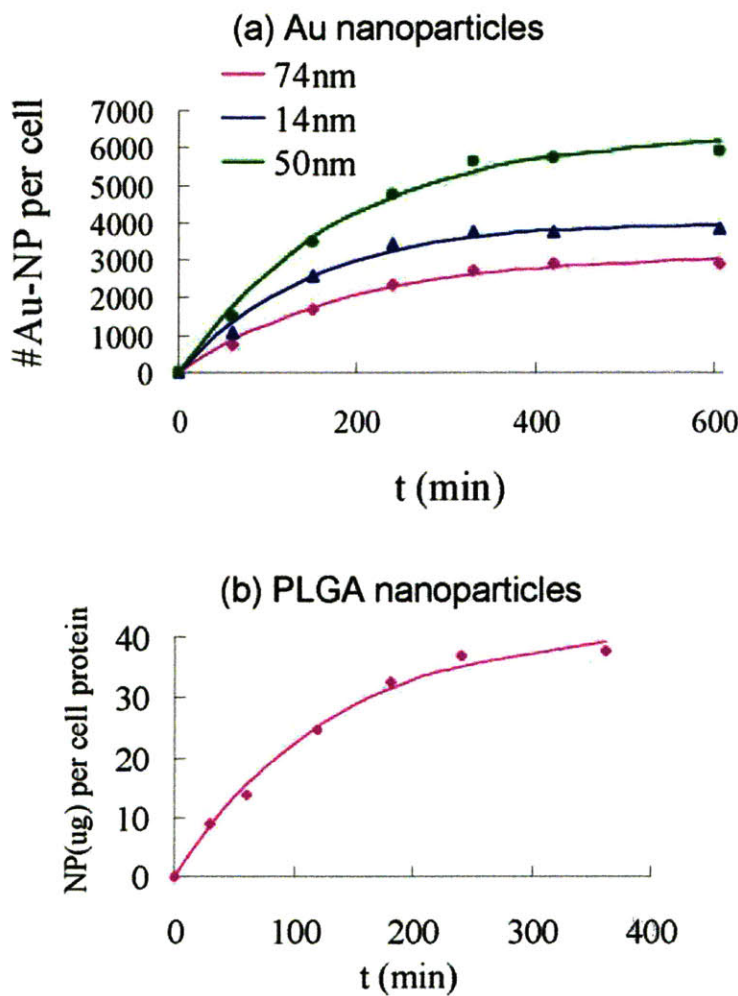
Figure 2.16

The real-time cellular uptake data of (a) Au nanoparticles of different diameters from ref [31,32]: 14nm (blue triangles), 50nm (green circles) and 74nm (pink diamonds), and (b) PLGA nanoparticles with a diameter of 97±3 nm from ref [40]. The results were obtained using the parameter values of k_a=1.196 min^{-1} and k_r=0.34 min^{-1} and summarized in Table 2.2 b and d.

The endocytosis rate constant is on the magnitude of 10^{-6} min^{-1}, with a maximum at a diameter of 50 nm, consistent with the experimental result. The recycling rate constant generally decreases with nanoparticle diameter, also in agreement with the

experimental finding that the exocytosis of Au nanoparticles is linearly related to size, with particles of larger diameter less likely to be exocytosed[32]. The recycling rate constant of Au nanoparticles is larger than that of DNA-SWNT. This rate should depend upon cell type (Hela cell for Au nanoparticles in ref 31,32 and 3T3 cell for DNA-SWNT in this work) and nanoparticle properties and is closely related to the membrane turnover rate.

The size-dependent, steady-state cellular uptake of Au nanoparticles with serum protein and transferrin coatings are compared in the literature[33]. The uptake of transferrin-coated Au nanoparticles is found to have a similar trend as those coated with serum protein, with a maximum uptake at a diameter of 50 nm. However, the uptake of transferrin-coated Au nanoparticles is only 1/3 that of the serum protein-coated ones. The result is consistent, since transferrin represents only one kind of protein in cell media and cells should display multiple receptor types, diminishing the surface density of transferrin-specific receptors[74]. As a result, transferrin-receptors are quickly saturated by the transferrin-coated Au-nanoparticles while for serum-coated nanoparticles, the surface density of receptors is much larger, since many kinds of receptors are available. However, this does not necessarily mean that transferrin is less favored or has a smaller endocytosis rate. As shown in Table 2.2c, for transferrin, ke is larger for all diameters, and disproportionately larger for the 50 nm-diameter case. Transferrin is endocytosed via clathrin-mediated endocytosis[75] and the microcages of clathrin coats that nucleate near or at the edge of a region of a clathrin network are almost perfectly spherical, with a radius of ~25-30 nm.[76]

For poly(D,L-lactide-co-glycolide; PLGA) nanoparticles with a diameter of $97 \pm$ 3 nm, cellular uptake versus time, attributed to endocytosis, has been reported for human arterial vascular smooth muscle cells[41]. The results of non-linear regression of ke and krec using are shown in Fig. 2.16b and Table 2.2d.

While the endocytosis rate constant differs by a factor of 10^3 in all three cases, the recycling rate constant only varies by a factor of 10. The values of ke found for the Au and PLGA nanoparticles are four orders of magnitude lower than constitutive membrane component turnover rate constants $(0.01 \text{ min}^{-1})^{77}$, which suggests that suppression of coated vesicle formation and/or uptake might be occurring in those situations. This suppression may be due to the nature of the nanoparticles, or the interaction of the cell membrane with the nanoparticle. The values found for the SWNT are much more in line with typical constitutive membrane turnover and thus no or little suppression may exist. The recycling rate constant, on the other hand, is quite similar across cell lines and nanoparticles, which may primarily depend upon the membrane turnover rate. Many aspects are amenable to quantitative analysis in our model.

We have developed a deterministic kinetic model for endocytosis and proposed a clustering mechanism to describe nanoparticles smaller than the predicted energy cutoff aggregate on the cell surface after a 2D diffusion process in order to be endocytosed. The model is validated for DNA-SWNT of lengths from 130 ± 18 nm to 660 ± 40 nm and for Au nanoparticles of diameters from 14 to 100 nm. This model describes the geometric influence and the dynamics of nanoparticle uptake for the first time. Both SWNT and Au have a maximum endocytosis rate near the 25 nm radius when scaled to account for diffusive interactions. The recycling (exocytosis) rate constants are similar in magnitude

(10^{-4} to 10^{-3} min^{-1}) for poly(D,L-lactide-co-glycolide), SWNT and Au nanoparticles and decrease with increasing size of either the nanoparticle or its clusters. Therefore, the model is able to quantitatively predict the cellular uptake of nanoparticles, which is necessary for engineering nano-systems of controlled toxicity, efficacy and functionality.

3. Modulation of Nanotube Fluorescence

3.1 Solvatochromism

3.1.1 Introduction

We will introduce the solvatochromism effect in the case of DNA-SWNT in the following as an example.

DNA is highly polymorphic and several types of single[9] and double stranded oligonucleotide can adsorb to the surface of SWNT. In a previous study[14], we found that divalent ions optically modulate SWNT PL when the nanotube is wrapped using a GT repeating 30-nucleotide. Divalent ions are known to bind to the negatively-charged backbone of DNA and induce conformational changes, as in the case of the first-order cooperative transition[78]. The DNA-SWNT complexes demonstrate reversible red shifting of the emission energies of their nIR PL in response to increasing divalent ion concentration. We aimed at understanding the mechanism of the red shifting, performed the following studies.

The modulation has an ion selectivity that is identical to the B to Z form transition for the corresponding free DNA. With increasing concentration, the PL emission wavelength of the SWNT traces a two state equilibrium curve that coincides closely with this B-Z form transition for the corresponding free DNA strand as monitored by circular dichroism.

The transition on the SWNT is also thermodynamically reversible: selective removal of the ions via a 12-14 kDa membrane restores the initial optical state. A

mathematical and conceptual model that assumes the transition on the SWNT proceeds identically to its free solution counterpart apparently describes several key features of these data. However, the exact molecular mechanism that proceeds on the nanotube surface is still unknown thus is the focus in this section.

DNA is known to adopt various conformations, including the right-handed A, B, C, D form and left-handed Z form[79]. In contrast to B-DNA, the Z-DNA form lacks a major groove. The purine 6, 7, and 8 positions and the pyrimidine 4 and 5 positions are exposed to the external solvent in Z-DNA. Both natural DNA and a variety of synthetic DNA of simple repetitive sequences are capable of adopting more than one conformation. Base sequence rather than overall base composition often clearly influences the preferred conformation under a given set of conditions. Moreover, Pohl and Jovin observed that the circular dichroism (CD) spectrum of (poly(dG-dC) • poly(dG-dC)) underwent a B to Z transition when the polymer was exposed to high salt concentrations[78]. Generally speaking, oligomers tend to be in the left-handed conformation in the presence of multivalent cations[80] such as Mg^{2+}, $Co(NH_3)_6{}^{3+}$, and spermidine^{3+} . It is reported that Mg^{2+} can coordinate directly to N7 of guanine and can hydrogen bond through its hydration sphere to a phosphate oxygen, stabilizing the Z conformation[81,82]. The stability of one DNA conformation is influenced by both the anions and cations[80].

Understanding how the diverse mechanisms of DNA conformational polymorphism are influenced upon adsorption to the nanotube surface is important for several reasons. First, DNA oligonucleotides have been effective handles to manipulate SWNT[21,70]. Second, they also provide a unique scaffold for sensors, electronic applications[83] and in vitro single-molecule studies.

3.1.2 Experimental Results and Discussion

The PL emission is observed to trace a two state, equilibrium curve, as depicted in Fig. 3.1 for various ions and three different sequences of DNA on the SWNT. While all SWNT in the sample demonstrate the PL red shift, the diameter dependence of the trend reported earlier[14] is such that the (6,5) SWNT has the largest shift. We focus on this species for the remainder of the study, while acknowledging similar trends for other SWNT. The maximum photoluminescence red-shift for all sequences is approximately 15 meV upon introduction of Hg^{2+} cations, with smaller shifts seen in response to other ions. Under some conditions, the ion concentration results in weakly attractive inter-particle potentials between DNA-SWNT, and quiescent solutions show loosely assembled aggregates (Open symbols, Fig. 3.1). These aggregates remain photo-luminescent and are easily re-dispersed by simple stirring (no ultrasonic processing). This process does <u>not</u> appear to affect the PL wavelength, and is therefore not responsible for the optical modulation. A maximum entropy evaluation of the autocorrelation functions resulted in the Maxent plots given in Fig. 3.2 with a bimodal distribution in relaxation times $\tau_R = 1/\Gamma$. The analysis found two dominant components. The major component's diffusion coefficient (from $\Gamma=q^2D$) is 4.2×10^{-12} m^2 s^{-1} and a minor fast component is apparent at 2.1×10^{-11} m^2 s^{-1}. Assuming an average nanotube diameter of 1 nm, these correspond to lengths of 600 nm and 40 nm respectively. In the presence of $HgCl_2$, the plots show no significant change in diffusion coefficient and therefore, no aggregation.
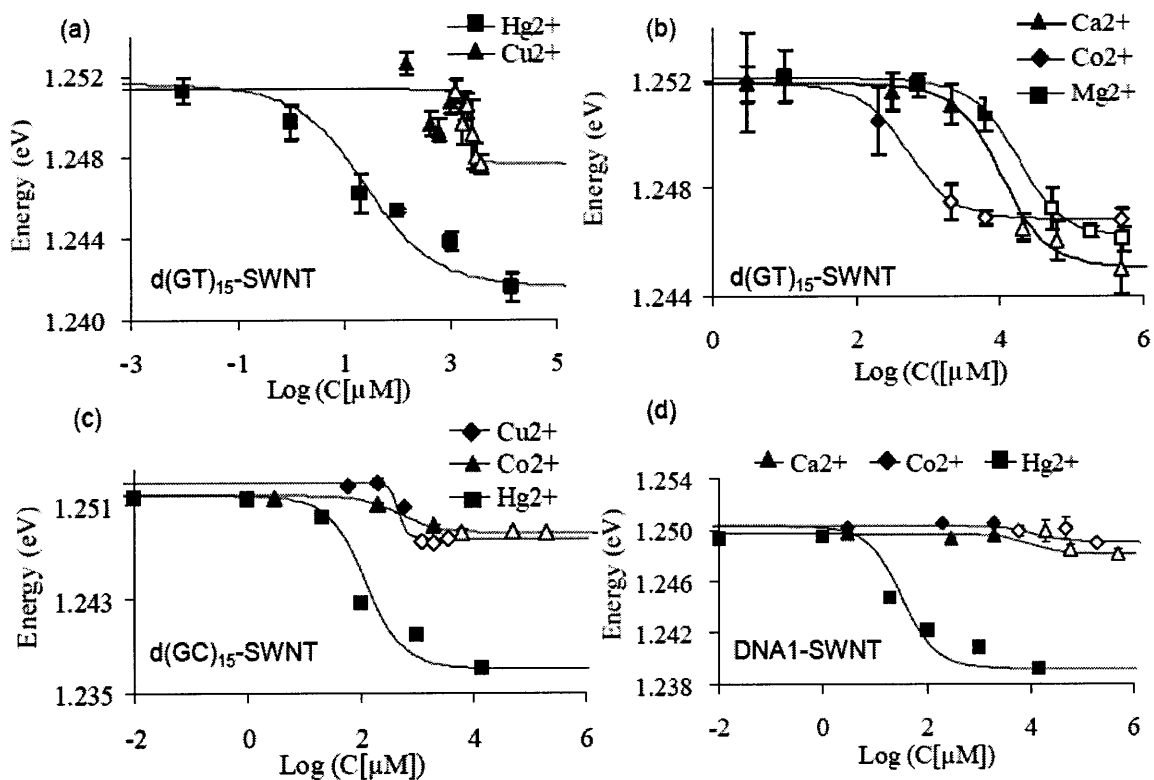
Figure 3.1 (a)-(d) Photoluminescence energy of (6,5) nanotube decreases due to the addition of various ions to d(GT)$_{15}$-SWNT(a)(b), d(GC)$_{15}$-SWNT(c) and DNA1-SWNT(d). The response is observed to trace a two state, equilibrium curve. Points here indicate data; hollow points indicate loosely held aggregates. Curves show the two-state model developed in the text.
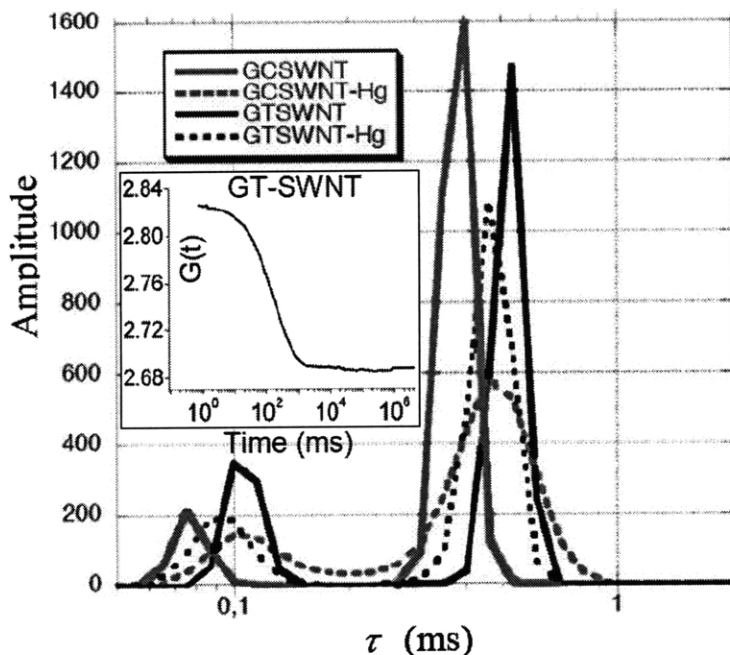
Figure 3.2 Dynamic light scattering Maxent plots compiled from correlation curves of DNA-SWNT complexes show no significant change in τ upon addition $HgCl_2$. Inset shows a correlation curve of the GT-SWNT complex.

A red shift of the SWNT PL is observed with an increase in temperature to 50 °C for all three DNA-SWNT (Fig. 3.3). Cooling below this temperature to 0 °C causes a blue shift. No divalent ions were added in this experiment, proving that the transition can be induced thermally. We anticipate that temperature changes over this range generally induce secondary structural changes in DNA[80]. The observation makes the possibility that the ion adsorbs and interacts with the SWNT directly unlikely. Both temperature and divalent ions alter DNA secondary structure, thus we conclude that the SWNT is modulated by changes in the adsorbed DNA structure.
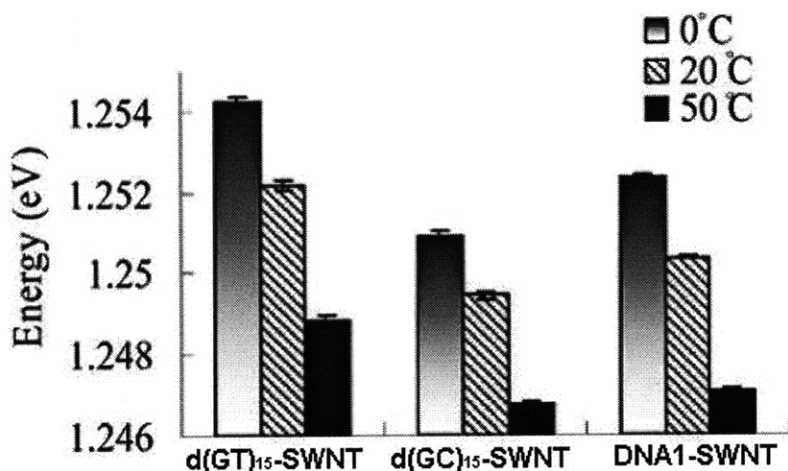
Figure 3.3 Energy decrease of (6,5) nanotube due to the temperature increase with three different kinds of DNA-SWNT.

To test whether a dissociative mechanism is involved (i.e. desorption of the DNA from the SWNT surface), the following dialysis experiment was performed. The (6,5) nanotube energy of d(GT)$_{15}$-SWNT, d(GC)$_{15}$-SWNT and DNA1-SWNT before and after the introduction of Ca^{2+} or Hg^{2+} was plotted in Fig. 3.4. A further dialysis step using 100 kDa MW cutoff tubing was performed after the transition reached steady state, and it was compared to the result by using 12-14 kDa MW cutoff tubing. Figures 3.4b-d show that for all three sequences the use of 100 kDa MW cutoff tubing to remove the Hg^{2+} results in no return blue shift to the starting point. Because the pore size of the membrane determines whether the shift is reversible or irreversible upon ion dialysis, we hypothesize that a dissociative mechanism is involved. Upon ion addition, DNA in single or complex form desorbs from the SWNT. If it is prevented from escaping through the dialysis tubing, the transition remains reversible. Otherwise it is irreversible. The extent or reversibility via the small pore (12-14 kDa) membrane is d(GT)$_{15}$-SWNT > d(GC)$_{15}$-SWNT > DNA1-SWNT. We note that the molecular weight for d(GT)$_{15}$,

d(GC)$_{15}$ and DNA1 is 9439.1 g/mol, 9213.9 g/mol and 7367.8 g/mol respectively, meaning that DNA1 has the highest possibility to transport through the 12-14 kDa MW cutoff tubing pore. Moreover, a 24 hr dialysis using 12-14 kDa MW cutoff tubing after a 24hr dialysis using 100 kDa MW cutoff tubing did not cause the blue shift back (Fig.3.4b). Hence, the energy shift is irreversible when the system is dialyzed using 100 kDa MW cutoff tubing at any stage. Herein, the transition is proposed as a competitive, partially peeling off of the DNA with increasing divalent ion concentration. DNA removal proceeds in a step-wise manner along the length. The process must complete before total desorption occurs. Compared to other ions, Hg^{2+} binds effectively, and at nano-molar concentrations should facilitate this process. However, for the other ions, complete desorption is not certain for moderate concentration ranges. For example, in the case of CaCl$_2$, the transition remains fully reversible when dialyzing using a 100 kDa MW cutoff tubing for 24 hours (Fig. 3.4a).
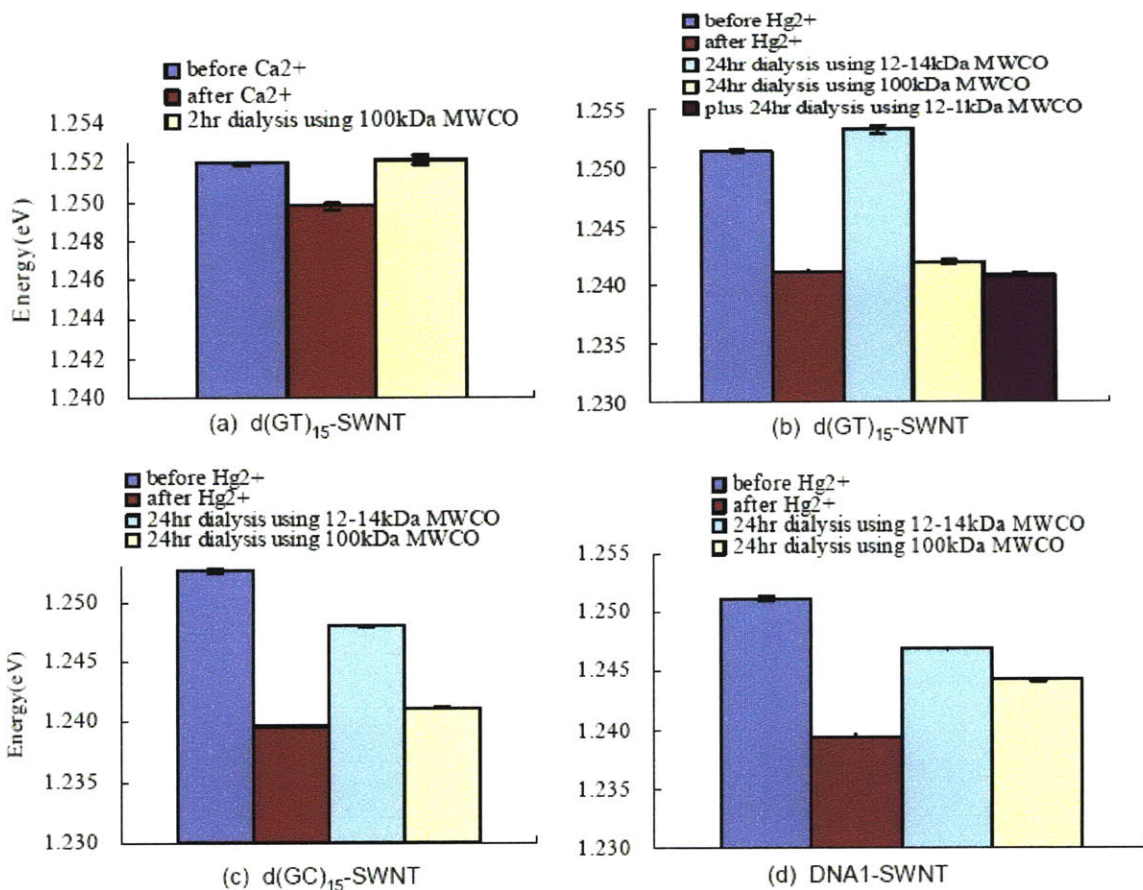
Figure 3.4 Photoluminescence energy of (6,5) nanotube before and after the introduction of ions to d(GT)$_{15}$-SWNT(a),(b), d(GC)$_{15}$-SWNT(c) and DNA1-SWNT(d). A 24hr dialysis was done for experiments with HgCl$_2$ using both 12-14kDa MWCO and 100kDa MWCO tubings, (b) (c) (d). An extra step of 24hr dialysis using 12-14dDa MWCO tubing is performed after the 24hr dialysis using 100kDa MWCO tubing for d(GT)$_{15}$-SWNT in (b). A 24hr dialysis was done for experiment with CaCl$_2$ (a), using 100kDa MWCO tubing. The concentrations for CaCl$_2$ and HgCl$_2$ are 2.5 mM and 0.5mM respectively.

To validate this dissociative hypothesis, we sought to detect an increase in free solution DNA upon divalent ion addition. A 20% PAGE gel that only allows free DNA to permeate into the gel was utilized. GelStar nucleic acid gel stain was used to detect either double-stranded (ds-) or single-stranded (ss-) DNA in gels. GelStar stain is highly fluorescent only when bound to nucleic acids thus giving superior signal-to-noise ratios

and obviating the need to destain the gel. The detection limits of GelStar strain are 20 pg for dsDNA and 25 pg for ssDNA[84]. Further, we observed that its fluorescence is not quenched by $HgCl_2$ in the case of $d(GC)_{15}$ (Fig. 3.5b). There are two bands for $d(GC)_{15}$ because this oligonucleotide can self-associate (Fig. 3.5a). The fast band is the single strand band and the slow band is the double strand band. The intensity of the fast band is increased by 23 % with 0.2 mM $HgCl_2$ and 55% with 1 mM Hg. Moreover, the length of the slow band is increasing with the concentration of $HgCl_2$ (Fig. 3.5c). On the other hand, the result from DNA1-SWNT is inconclusive in Fig. 2.4a because the dye fluorescence is quenched by $HgCl_2$ (Fig. 3.5b). The sample of $d(GT)_{15}$ is not included here because no fluorescence was observed in this assay.
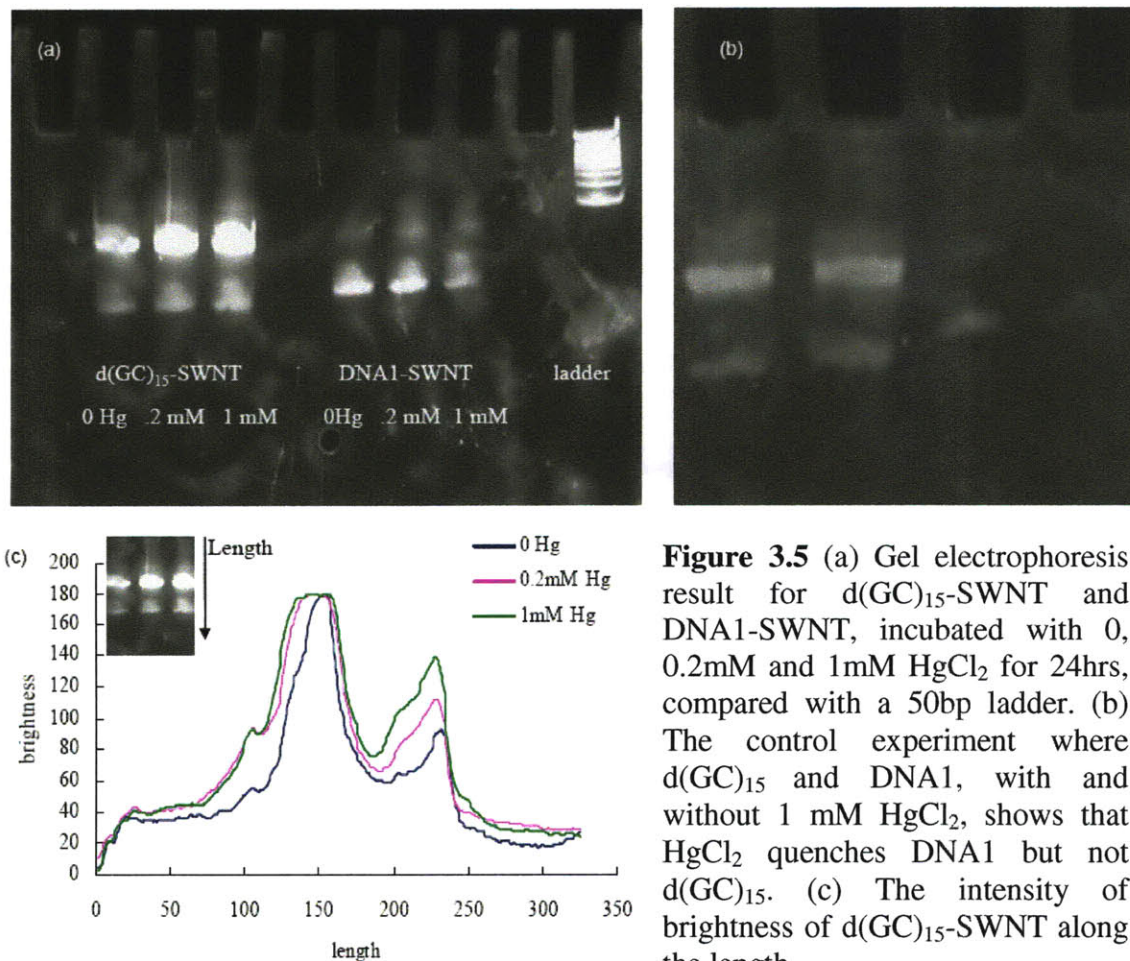
Figure 3.5 (a) Gel electrophoresis result for $d(GC)_{15}$-SWNT and DNA1-SWNT, incubated with 0, 0.2mM and 1mM $HgCl_2$ for 24hrs, compared with a 50bp ladder. (b) The control experiment where $d(GC)_{15}$ and DNA1, with and without 1 mM $HgCl_2$, shows that $HgCl_2$ quenches DNA1 but not $d(GC)_{15}$. (c) The intensity of brightness of $d(GC)_{15}$-SWNT along the length.

While d(GT)$_{15}$ does not form the traditional Watson-Crick base pairs, it can form T-T and G-G base pairs by hydrogen bonds[85]. It was discovered by optical techniques that the telomeric dG(GT)$_4$G sequence can form a parallel-stranded double helical conformation via this nontraditional purine-purine and pyrimidine-pyrimidine base paring[86]. G quadruplexes are formed in this case to stabilize the structure. We have found, however, that the d(GT)$_{15}$ oligonucleotide does not form a duplex based on experimental results using FRET. A d(GT)$_{15}$ oligonucleotide labeled with Cy5 at the 5' end and a similar strand with 3' bound Cy3 were annealed in the presence of two different NaCl concentrations. On exciting the annealed sample at the Cy3 absorption maximum of 535 nm, we expect to see a strong Cy5 emission at 664 nm due to FRET between the dye pair if double stranded DNA is formed. The GT annealed product did not produce an emission peak at 664 nm for either parallel or anti parallel duplex formation at 100 mM Na and at 1 M Na (Fig. 3.6).
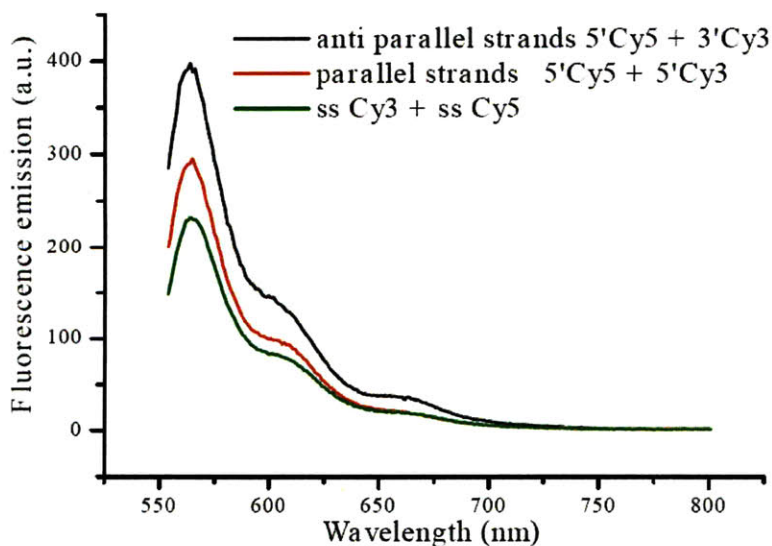
Figure 3.6 Fluorescence emission of the annealed DNA samples and the control of separate Cy3-ssDNA and Cy5-ssDNA on 535nm excitation. The lack of Cy5 emission implies that no parallel or anti parallel duplex was formed and hence no FRET between Cy3 and Cy5 occurred.

The small peak visible at ~ 660 nm is understood to be Cy5 emission on indirect absorption of the 535 nm incident light. This can be seen in the dotted curve which is the sum of the emission obtained on separately excited Cy3-ssDNA and Cy5-ssDNA. Hence, we conclude GT does not form a parallel or anti parallel duplex in free solution, also confirmed by an experiment involving the intercalating dye PicoGreen (Fig. 3.7). We tested the double-strandness and single-strandness of d(GT)$_{15}$, d(GC)$_{15}$ using DNA1 and hybrid DNA1 with the PicoGreen assay[87]. The PicoGreen assay is based on a cyanine dye that exhibits a very large (>1000-fold) increase in fluorescence quantum yield upon binding to dsDNA, while single-stranded oligodeoxyribonucleotides are detected weakly[87,88]. Figure 3.7 compares the PicoGreen fluorescence intensity for DNA1, DNA1+cDNA1, d(GT)$_{15}$ and d(GC)$_{15}$, each contains a total of 10μg of DNA. We know that DNA1 is single stranded while DNA1+cDNA1 is double stranded. The PicoGreen fluorescence intensity for d(GT)$_{15}$ (85.5782) is less than that of DNA1(122.6251), indicating that d(GT)$_{15}$ does not form the traditional duplex in solution that could be detected by PicoGreen effectively. Similarly, the PicoGreen fluorescence intensity for d(GC)$_{15}$ (279.0048) is closer to that of the hybrid DNA1 (371.8714) than DNA1 (122.6251), meaning that d(GC)$_{15}$ forms duplex in solution. This is easy to understand because guanine (G) forms a base pair with cytosine (C) via three hydrogen bonds.
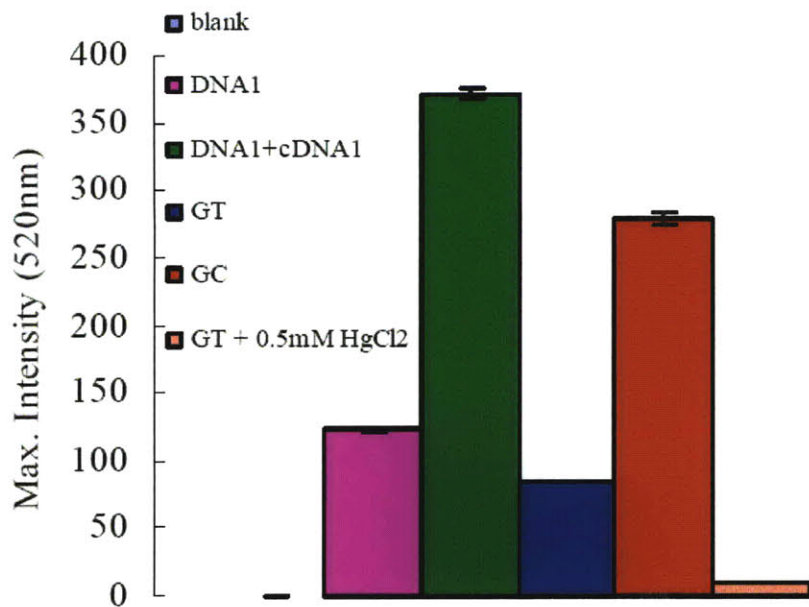
Figure 3.7 PicoGreen fluorescence intensity from DNA samples used in this work indicating single or duplex wrapping

However, we note that on the SWNT surface, it behaves functionally similar to d(GC)$_{15}$ which is a dimer both in free solution and on the SWNT. It is likely that d(GT)$_{15}$ does not have a simple single-stranded structure on the SWNT, despite the evidence that in free solution, it is dissociated. The sequence we refer to as DNA1 is obviously single-stranded and a duplex is formed only in the presence of its complement sequence. Herein, we attribute the red shift to the conformational change of DNA on SWNT, which involves a competitive, stepwise partial peeling off the DNA along the length of SWNT.

3.1.3 Derivation of the Polymorphism Model

We assume that it takes β steps for the complete peeling of DNA from SWNT. In the step-wise peeling process, there exist β states of DNA on SWNT described as $DNA_i - \theta_{\beta-i}$ (i=0, 1...$\beta-1$), where DNA_i represents the part of DNA that is released

from its binding sites on SWNT (vacuuming i binding sites), $\theta_{\beta-i}$ represents the binding sites on SWNT occupied by the other part of DNA (Given a total number of β binding sites per SWNT, if i of them are empty, β-i of them are still occupied). We note here that the physical meaning of β can be considered as the number of binding sites per SWNT, based on Langmuir isotherm theory. However, this 'binding site' is theoretical and is different from the actual physical binding site, which depends on the length and sequence of DNA and its chemical bonding with SWNT. No assumption of exact structure of DNA (like double or single strand) is made here so this model can be applied to all three samples of DNA-SWNT in this study.

The β steps of this peeling process can be described in the following reactions:

$$DNA_i\text{-}\theta_{\beta-i} + nI \rightleftharpoons DNA_{i+1}\text{-}\theta_{\beta-i-1} \qquad 0 \le i \le \beta-1$$
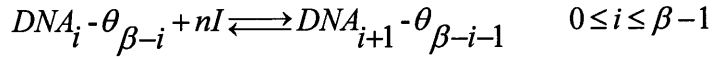
where n is the number of ions involved in each step

The overall reaction is obtained by summing the above β reactions together

$$DNA_0\text{-}\theta_\beta + \beta nI \rightleftharpoons DNA_\beta\text{-}\theta_0$$
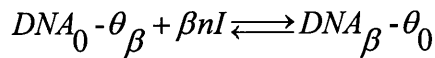
For convenience, $[DNA_i\text{-}\theta_{\beta-i}]$ is written as Ai, which means there are i binding sites released per SWNT. The concentration of ions is written as I. We make the assumption here that the forward reaction rate constant (k_1) are identical for the β reaction steps and the backward reaction rate constant (k_{-1}) are also identical for the β reaction steps. The equilibrium constant for the β reactions equals k_1 / k_{-1}, and we use K to represent this. We can write β differential equations as follows.

$$\frac{dA_0}{dt} = -k_1 A_0 I^n + k_{-1} A_1 = 0 \qquad (1)$$

$$\frac{dA_1}{dt} = (k_1 A_0 I^n + k_{-1} A_2) - (k_{-1} A_1 + k_1 A_1 I^n) = 0 \qquad (2)$$

...

$$\frac{dA_i}{dt} = (k_1 A_{i-1} I^n + k_{-1} A_{i+1}) - (k_{-1} A_i + k_1 A_i I^n) = 0 \qquad (i)$$

i is an integer and $1 \le i \le \beta - 1$

...

$$\frac{dA_\beta}{dt} = k_1 A_{\beta-1} I^n - k_{-1} A_\beta = 0 \qquad (\beta)$$

We solve the above β algebraic equations and get

$A_i = (KI^n)^i A_0 = q^i A_0$, where i is an integer, $1 \le i \le \beta$

Let $B_0 = \sum_{i=0}^{\beta} A_i = A_0 + A_1 + ... + A_\beta = A_0 + qA_1 + ... + q^\beta A_\beta = A_0 \cdot \frac{1 - q^{\beta+1}}{1-q}$

$\Rightarrow A_0 = \frac{(1-q)B_0}{1 - q^{\beta+1}}$

The number of total binding sites still occupied $\theta = \sum_{i=0}^{\beta} iA_i$

$\theta = 0 \cdot A_0 + A_1 + 2A_2 + ... + \beta A_\beta$

$= qA_0 + 2q^2 A_0 + ... + \beta q^\beta A_0$

$= A_0(q + 2q^2 + ... + \beta q^\beta)$

$= A_0 R$

$R = q + 2q^2 + ... + \beta q^\beta$

$qR = q^2 + 2q^3 ... + \beta q^{\beta+1}$

$$(1-q)R = q + q^2 + \ldots + q^\beta - \beta q^{\beta+1}$$

$$= \frac{q(1-q^\beta)}{1-q} - \beta q^{\beta+1}$$

$$= \frac{q(1-(\beta+1)q^\beta + \beta q^{\beta+1})}{1-q}$$

$$R = \frac{q(1-(\beta+1)q^\beta + \beta q^{\beta+1})}{(1-q)^2} \quad \text{plug into the expression of } \theta \text{ and get}$$

$$\theta = \frac{A_0 q(1-(\beta+1)q^\beta + \beta q^{\beta+1})}{(1-q)^2}$$

$$q = KI^n$$

$$= \frac{q(1-(\beta+1)q^\beta + \beta q^{\beta+1})}{(1-q^{\beta+1})(1-q)} \cdot B_0$$

The DNA surface coverage on SWNT and the normalized energy has the following relation

$$\frac{\Delta E}{\Delta E_{max}} = \frac{\theta}{\beta B_0} = \frac{q(1-(\beta+1)q^\beta + \beta q^{\beta+1})}{\beta(1-q^{\beta+1})(1-q)}$$

The curves in Fig. 3.1 a-d show the model. $A_\beta = (KI^n)^\beta A_0$ describes the population of complete transition.

3.2 Fluorescence Quenching

3.2.1 Introduction

Besides solvatochromism, we explored other method of SWNT fluorescence modulation towards a single molecule sensor. The 1D quantum confinement of photogenerated excitons in SWNT can amplify the detection of molecular adsorption to where single molecule discrimination is realizable, even from within living cells and tissues. As is shown in Fig. 3.8, the 1D exiton has a lifetime of 100 ps, a diffusion

coefficient of 0.4 cm^2/s, and an excursion range of 90 nm[17]. If the exiton encounters an adsorbate (i.e., hydrogen peroxide, H_2O_2), energy is lost to phonons, in other words, this exiton is quenched. The quenched state persists until desorption.
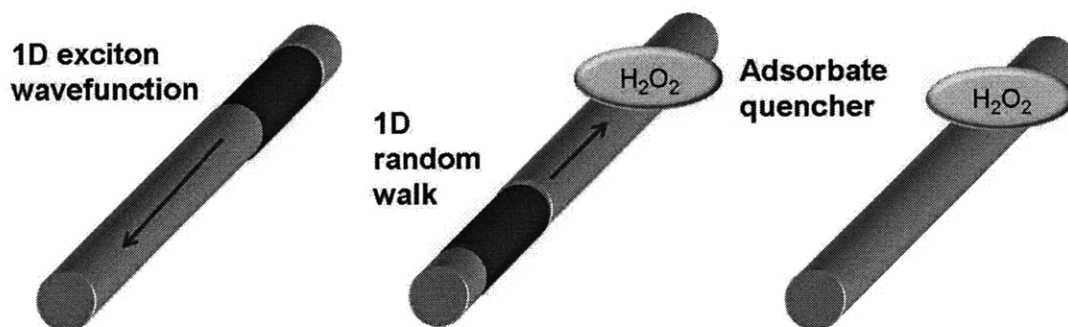
Figure 3.8 Exitons on the nanotube is confined to 1D and can be quenched and dequenched upon adsorption and desorption of a quencher (i.e., H_2O_2).

Towards the aim of engineering and modeling the fluorescence change based on this mechanism, we present a type 1 collagen film, similar to those used as 3D cell scaffolds for tissue engineering, containing an array of embedded SWNT capable of reporting single molecule adsorption of quenching molecules. We utilize Hidden Markov Modeling to link single molecule adsorption events to rate constants for H_2O_2, proton (H^+), nitric oxide (NO), nitrite (NO_2^-), nitrate (NO_3^-), various cell media, etc. (Fig. 3.9). Among the kinds of reactant molecules studied, H_2O_2 binds the nanotube with a forward (77.8 M^{-1}s^{-1}) and reverse (0.0006 s^{-1}) rate constant[18] that enables both sensitive detection and reversibility to the exclusion of other reactive species with long lifetimes. Except for nitric oxide (NO), H_2O_2 has the largest forward rate constant of all species considered, meaning that its capture probability is highest. Protons (H^+) can be detected with a forward rate of 8.1 M^{-1}s^{-1}, but their reverse rate constant is high (0.0011 s^{-1}) such that, at physiological pH (7.4) their contribution is negligible. Likewise, interfering nitrites and

nitrates have small rate constants and there is no contribution from components of cell media (Dulbecco's Modified Eagle Medium and Leibovitz's L-15 Medium). NO has a high forward binding rate of 80.0 $M^{-1}s^{-1}$, however its reverse rate is almost immeasurable under these experimental conditions. This means that its presence can be easily distinguished, as it irreversibly deactivates the SWNT single molecule sensor that it encounters. In this work, we did not detect any events of this kind and therefore rule out NO as an interfering agent in our experiments. In addition, our sensor is inert to singlet oxygen ($^1O_2$) and superoxide ($O_2^{\bullet-}$). Generally, the quenching rate constants increased with an increase in redox potential of the quencher, indicating that electron transfer increases the adsorption equilibrium constant on the nanotube surface, and hence the dwell time of the quencher. These developments provide the material, analytical, and mechanistic groundwork for SWNT to function as single-molecule stochastic biosensors.
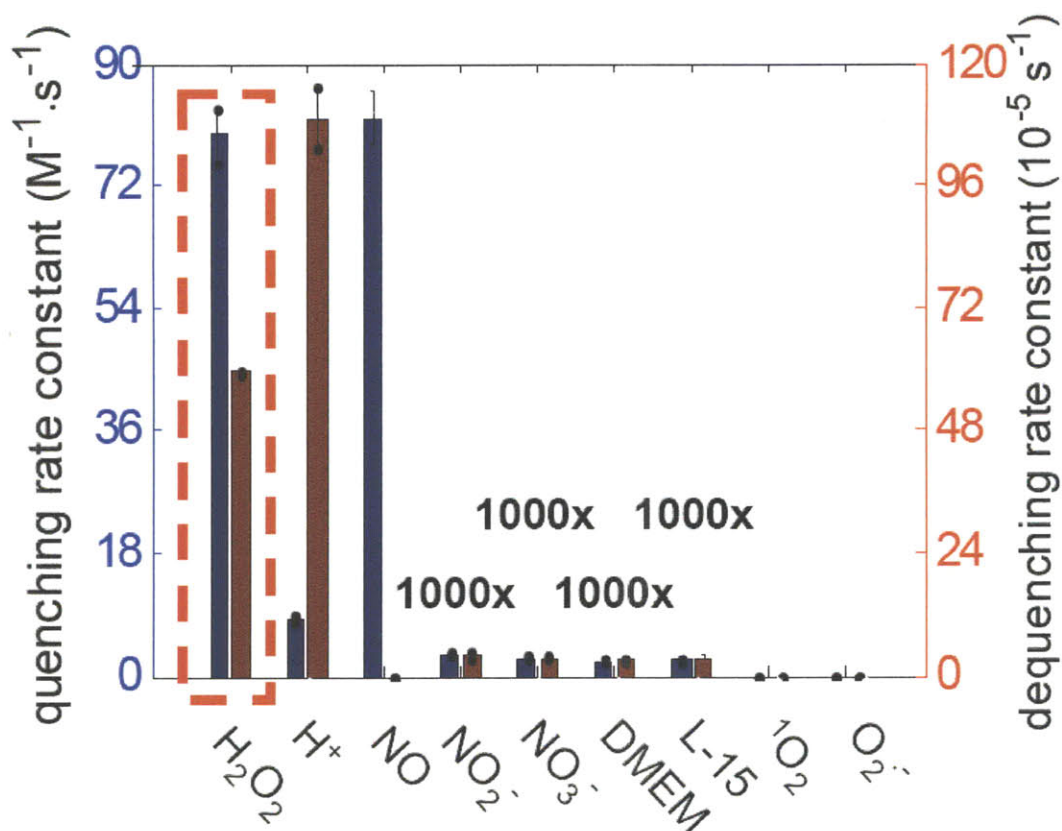
Figure 3.9 Sensor binding rate and reverse binding rate for collagen-SWNT embedded in collagen film for various analytes. SWNT sensors are selectively sensitive for H_2O_2 in that the binding rate is much higher than the reverse binding rate. H^+ has a high reverse binding rate. Nitric oxide has a high binding rate, indicating that its contribution is easily identified as an irreversible signal response.

3.2.2 Experimental Results, Model Derivation and Discussion

Collagen 1 is found in most tissues and organs of animals, but is most plentiful in dermis, tendon and bones. The use of collagen substrates *in vitro* facilitates the growth and differentiation of many cell types[89]. Collagen promotes attachment of plated cells when used as a thin layer[90]. Cells adhere directly to collagen through integrin receptors or via adhesion proteins such as fibronectin, which binds to both the cells and the collagen[90]. SWNT, if properly embedded in a collagen thin film, provide a promising

platform for cellular based single-molecule detection, an application that we plan to develop in the final chapter of this work.

Hidden Markov Modeling (HMM), recently applied to single molecule biophysical applications[91,92], is an analytical method used in this work which allows efficient statistical extraction of stochastic events from any number of luminescent molecules to determine the kinetics and mechanism of detection.

The bulk fluorescence quenching rate of SWNT induced by metals has been reported in the literature[93,94]. However, the demonstrated detection limit from ensemble measurements is still greater than 0.5 mM and quantitative analysis on the rate has not been conducted at the single-molecule level for any analyte to date.

The purpose of this section is to introduce a useful, collagen-based platform for single molecule detection compatible with either 3D patterning or surface plating of living cells. We demonstrate how HMM can be used to analyze the forward and reverse adsorption and quenching rates of various analytes. The analysis is shown to be self-consistent, allowing stochastic adsorption and quenching events to reconstruct the chemical mechanism and rate constants. For example, we verify that that all desorption probabilities are concentration independent, as expected. We also find that the quenching probabilities increase with the increase of quencher concentration, although nonlinearly.

Complexes of type 1 collagen and HiPCO SWNT (hereafter called collagen-SWNT) were prepared by light probe-tip sonication, resulting in a photoluminescent suspension (Fig. 3.10a).
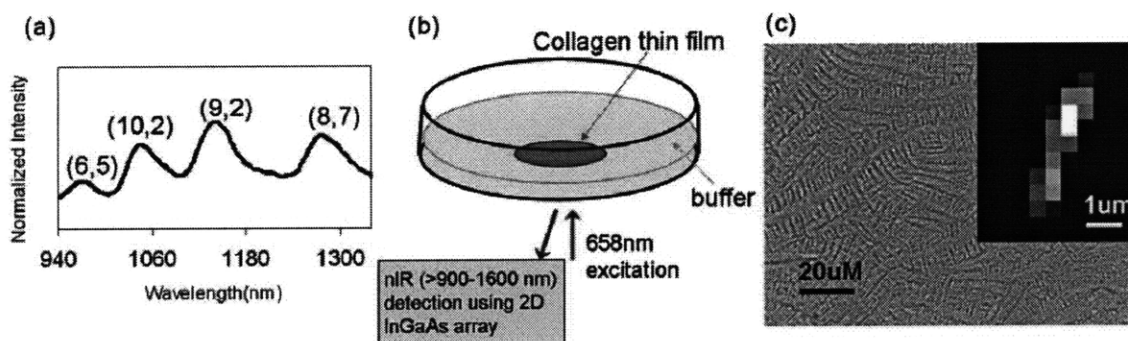
Figure 3.10 (a) The spectrum of solution-phased SWNT suspended in collagen, exited at 658 nm. (b) Experimental configuration used for single-molecule quenching of collagen-SWNT in a collagen film buffered by PBS on an inverted microscope with 658 nm laser excitation and detection via a 2D InGaAs imaging array. (c) A phase contrast image of collagen-SWNT in a collagen film with the inset representing the fluorescence image of one nanotube detected in the nIR.

Spectral resolution of the resulting system is high enough to unambiguously assign photoluminescence emission to specific (n,m) SWNT[2]. Thin films of collagen-SWNT were prepared by modification of established methods[95]. Briefly, collagen-SWNT was diluted 68x with 0.02N acetic acid and air dried on glass bottom petri dishes. The resulting films are translucent (Fig. 3.10b) and exhibit strong SWNT photoluminescence upon 658 nm excitation (Fig 3.10c inset). The fluorescence from a single nanotube is recorded at 1 frame/s and the fluorescence within a 2 × 2 pixel spatial binning region is examined. The 4 pixel area corresponds to a 900 by 900 nm region of the field, which is the diffraction limit in the nIR range.

The emission from such spatial binning regions on single SWNT in the dry film exhibits some blinking behavior and partial quenching upon immersion in 0.1x phosphate buffered saline (PBS). After rapid quenching, the photoluminescence remains stable upon long-term excitation (Fig. 3.11).
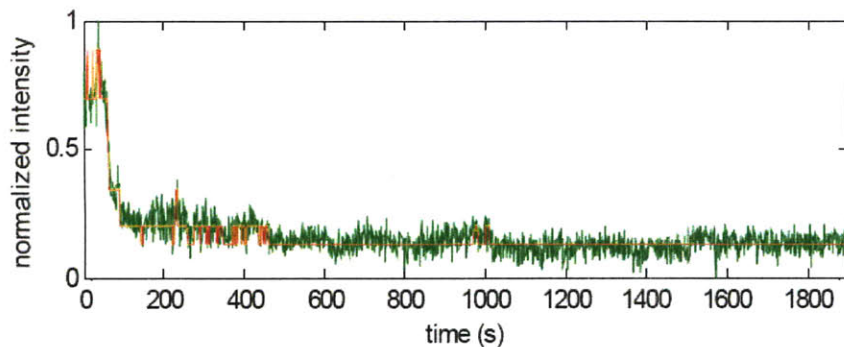
Figre 3.11 Example trace showing initial quenching of SWNT photoluminescence upon excitation of collagen-SWNT films in PBS at 658 nm. The traces (green) were fit using HMM (red).

We investigated this initial quenching by heating the sample to 45 °C before and during photoexcitation. The SWNT in the heated film exhibited a higher rate of quenching (see below) than samples kept at room temperature (Fig. 3.12). We speculate that a reorganization of the collagen peptides upon photoinduced heating elicits quenching and we will discuss further below.
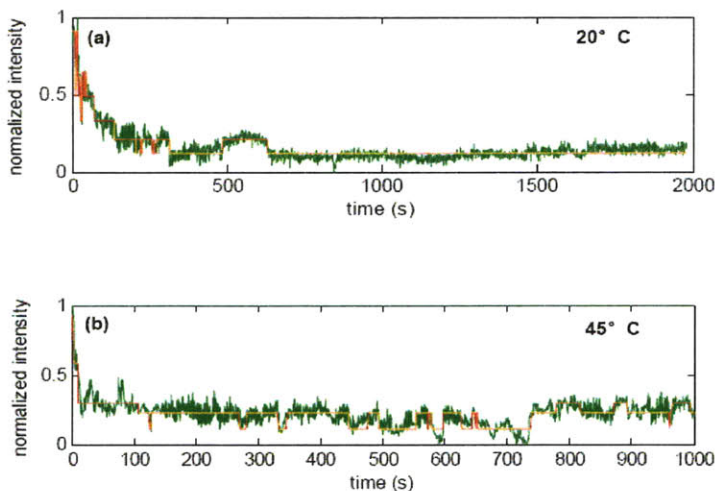
Figure 3.12 The initial SWNT photoluminescence quenching rate exhibits temperature-dependent differences. The quenching rate increases between room temperature measurement at (a) 20°C and heating the film to (b) 45°C.

Collagen denatures when heated, similar to other proteins. The denaturation takes place at temperatures as low as 37 °C [96], leading to a decrease in the degree of

crosslinking within its triple helices structure[97], and may allow peptide amine groups that were previously constrained to contact the SWNT surface. The result in this case is local excitonic quenching. Similar excitonic quenching by amine groups has been observed for quantum dots[98-101]. Ceasing photoexcitation causes signal restoration, which indicates that the process is reversible, consistent with a collagen denaturation process[102]. What is relevant for this chapter is that after this initial, partial quenching, the photoluminescence remains stable on long-term excitation[18].

With the addition of various quenchers as the start point to freshly made collagen-SWNT films, representative traces (green) are shown in Fig. 3.13, under the condition of 20 μM (Fig. 3.13a), 50 μM (Fig. 3.13b), 100 μM (Fig. 3.13c) of H_2O_2, a pH value of 4 (Fig. 3.13d), 2 (Fig. 3.13e), 1 (Fig. 3.13f).
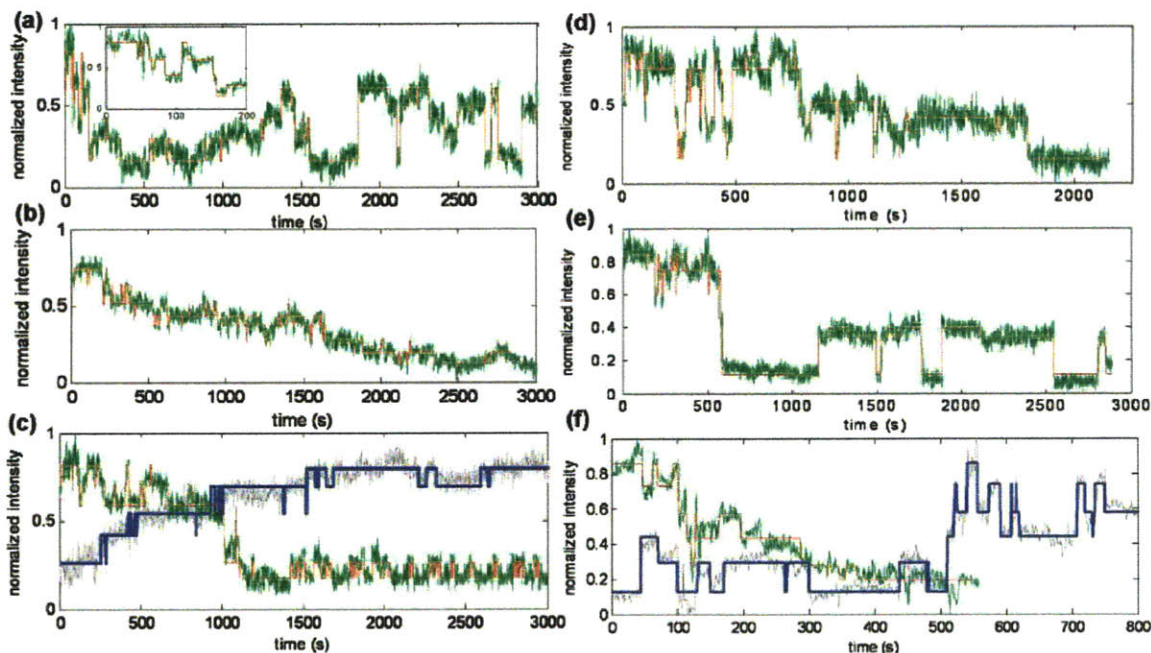
Figure 3.13 Representative luminescence intensity of a 2 x 2 pixel spatial binning region on three different individual nanotubes from three different sets of experiments that shows stepwise quenching (green traces) after the addition of (a) 20 μM H_2O_2, (An expansion of the first 200s period shown in the inset represents well-defined reversible steps.) (b) 50 μM H_2O_2, (c) 100 μM H_2O_2, (d)-(f) HCl to reach a solution pH of 4, 2 and 1 respectively. All additions occur at t=0. The quenching is reversed after adding MnO_2 (c, grey trace) or neutralizing the pH with NaOH (f, grey trace). These typical traces are fit with a HMM algorithm shown in red steps for reagent detection and blue for reagent removal/neutralization.

The representative traces, normalized the same way as previous works[91,92] on the single molecule studies using HMM, show single-step changes in SWNT photoluminescence intensity, caused by the mobile exciton on the SWNT sidewall being attacked by the quencher molecules, similar to the observations of Cognet and co-workers for agrose-gel-immobilized SWNT[17]. The normalization corrects the differences in the starting and ending fluorescence for different nanotubes and allows for the quantitative studies on the transitions between states for various nanotubes. Note that although only one representative trace is shown in various situations in Fig. 3.13, the

analysis and conclusions in this study are not based on any one particular nanotube. The later discussions on the transition density plot (TDP) shows that the same kind of transitions is observed from trace to trace for each set of experiment, which is then used to calculate the transition probabilities and quenching rate constants. For instance, after normalization, all the 100 traces studied in the case of 20 μM H_2O_2 show 5 states (Fig. 3.13a), resulting in 8 distinct peaks in TDP (Fig. 3.14). The H_2O_2 and H^+ induced quenching were reversed respectively with MnO_2, a catalyst for H_2O_2 decomposition, and NaOH. Representative traces are shown in Fig. 3.13c, f (grey traces).
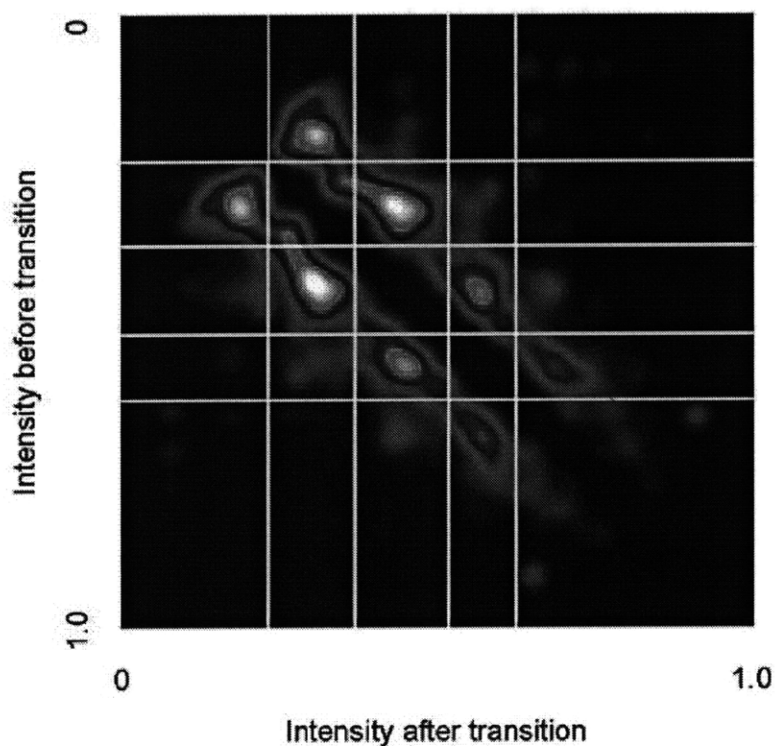
Figure 3.14 The example transition density plot (TDP) for the 100 traces under a condition of 20 μM hydrogen peroxide as an illustration, where all the transitions are plotted according to their normalized intensity levels before and after transition. The eight distinct peaks indicate that there are five distinct, reproducible fluorescence states.

The stepwise quenching and de-quenching, represented as the green and grey traces in Fig. 3.13 can be described by a Hidden Markov process[103], shown as the red and blue step traces in Fig. 3.13. A Markov process consists of state-to-state transitions with the kinetics of single-exponential decay. Hidden Markov modeling (HMM), although first developed for speech recognition, has been applied recently to single-molecule fluorescence data analysis[91,92,104-108]. Although a noiseless trace is desired experimentally, a distribution in the fluorescence states typically hides the underlying Markov process. In this case, HMM is especially useful in that it can identify and reconstruct the underlying real states[91].

The governing parameters of the model are described by transition and emission probabilities between different states. In the most general case, the transition probability P_{ij} represents the probability of a single site currently in state i transiting to state j in the next time interval. Emission probabilities EP represent the likelihood of observing an intensity value I_{data} when the system is in a certain state ϕ with idealized intensity value I_ϕ. In the analysis that we adapted from the work of McKinney and coworkers[91], the observed intensity distribution is modeled using a Gaussian function with a characteristic width δ, where the emission probability EP (I_{data}) is proportional to $\exp[-2\times(\frac{I_{data}-I_\phi}{\delta})]$. The total probability of the most likely sequence of states are optimized, by varying the model parameters (I_ϕ, δ, P_{ij}, for all i,j,ϕ) and thus the real states are reconstructed.

Consider n sites capable of quenching in our analysis, where the sites represent physically those regions capable of exciton recombination resulting in photo-emission within each 2 by 2 pixel spatial binning region. The exciton excursion range in highly

luminescent SWNT is ~90 nm[17], which contributes a maximum of 10 sites per spatial binning region of 900 by 900 nm. The exact number of sites that are quenchable apparently depends on the concentration and type of each quencher, resulting in different number of states for each case. The number of states found by HMM is 8 for 50 µM and 100 µM H_2O_2, 5 for pH 4, 6 for pH 2 and 1.

We used 100 traces per set of conditions in our data analysis (the example traces are shown in Fig. 3.13), although it has been established in the literature that with as few as 20 traces, the statistical error is already minimal[91]. Further, in our case we note that the intensity spacing is greater than noise width, data sampling occurs at more than twice the rate of typical transitions, and at least one transition occurs per trace. We conclude that the algorithm can generate accurate states and transition probabilities for our system[91]. The transition density plot (TDP) [91] for the 100 traces under a condition of 20 µM H_2O_2 is shown in Fig. 3.14 as an illustration, where all the transitions are plotted according to their normalized intensity levels before and after transition. Eight distinct peaks are developed in Fig. 3.14, meaning that there are five *distinct, reproducible* fluorescence values reconstructed as different states[91] throughout the 100 traces that we have used. Specifically, all the transitions can be described by '5->4', '4->5', '4->3', '3->4', '3->2', '2->3', '2->1', '1->2', with '5' the highest fluorescence intensity (no quenched sites) and '1' the lowest (all sites quenched).

One goal of this chapter is to link site specific quenching probabilities to an overall chemical mechanism for a series of quenchers. Our model asserts that there are unquenched sites on the nanotube that can be quenched by quencher molecules (Fig. 3.15a), with a forward probability of P_1 and a reverse probability of P_2. The probability

that an unquenched site remains unquenched and a quenched site remains quenched is 1-P_1 and 1-P_2 respectively. All of the quenchable sites on the nanotube can independently transition between unquenched and quenched. On the single-molecule level, it is important to convert the transition probabilities between states to the transition probabilities from being unquenched to being quenched for each individual site. This will allow us to characterize different reactions with various numbers of underlying states *independently*.
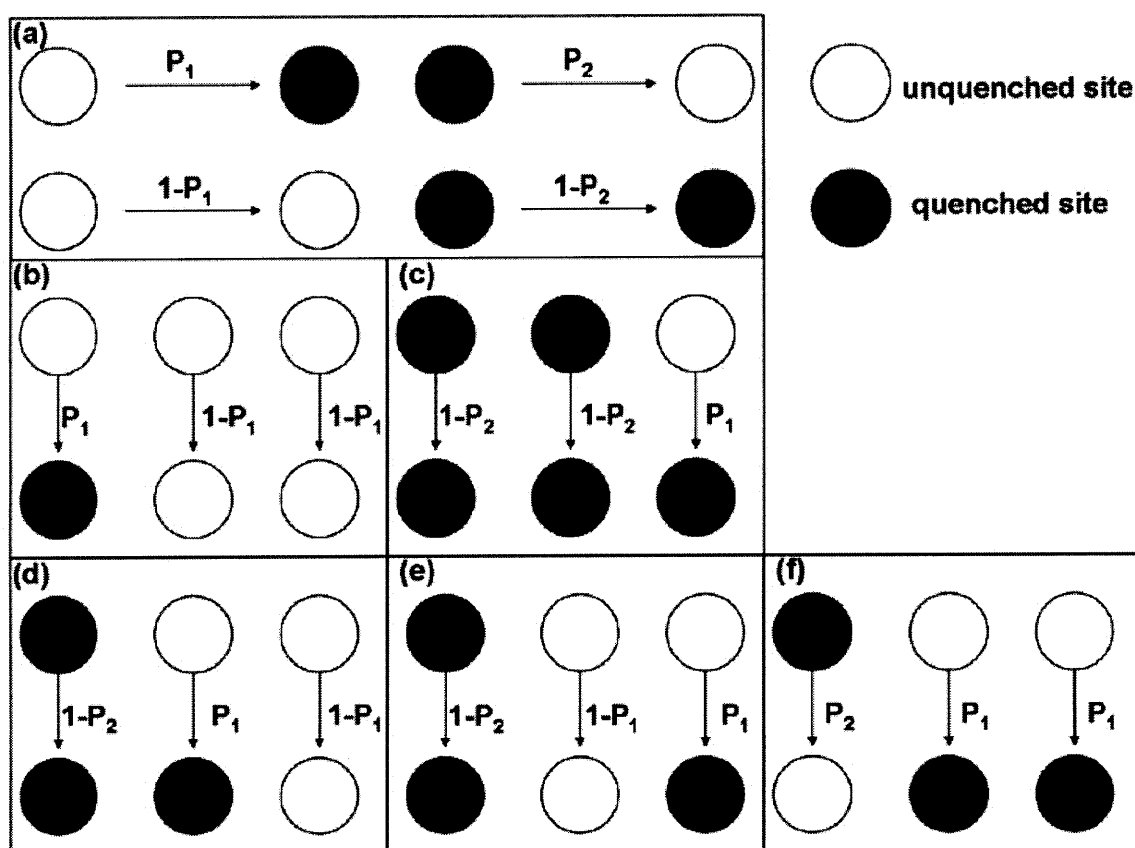
Figure 3.15 (a) The transitions between an unquenched site and a quenched site, with a transition probability of P_1 for an unquenched site to be quenched, P_2 for a quenched site to become unquenched, (1- P_1) for an unquenched site to remain unquenched and (1- P_2) for a quenched site to remain quenched. (b)-(f) The transition scheme of a three quenchable sites (four states) model. Different levels of transitions are shown in '4->3' (b), '2->1' (c) and '3>2' (d)-(f), with '4' the highest fluorescence level and '1' the lowest.

As an illustration, consider the case of 3 quenchable sites: there are a total of 4 states, with 0, 1, 2, and 3 sites quenched. Again, we will label the state with the highest fluorescence with the largest number '4' and the state with the lowest fluorescence with the smallest number '1'. The probability that a '4->3' transition will be observed is $3P_1(1-P_1)^2$, as is shown in Fig. 3.15b. Similarly, the probability that a '2->1' transition will be observed is $3P_1(1-P_2)^2$ (Fig. 3.15c). The more complicated case is '3->2' (Fig. 3.15d-f), where the total transition probability is $3[2P_1(1-P_1)(1-P_2)+P_1^2P_2]$. The reverse transition probability is $3P_2(1-P_1)^2$, $3P_2(1-P2)^2$ and $3[2P_2(1-P_1)(1-P_2)+P_1P_2^2]$ for transition '3->4', '1->2' and '2->3' respectively. Herein, if given a transition probability matrix, the quenching probability P_1 and the reverse probability P_2 for each individual site can be calculated (see Appendix A).

In general, the relationship between the transition probability and reaction rate constant[59] for a single-channel single-molecule reaction (Fig. 3.15a) is described by Gillespie's pioneering work[109]

$$P_0(\tau) = \exp(-k\,\tau) \quad \text{(Eq. 3.1)}$$

where $P_0(\tau)$ is the probability that, given the states at time t, no reaction will occur in the time interval $(t, t + \tau)$ and k is the *stochastic* reaction constant[43].

The evolution of one site between the state of being unquenched and quenched is Markovian, which means that the evolution is random and memory-less. The probability that an unquenched site at *any* time point t, *remains* unquenched in the next time interval $t + \tau$ is $(1-P_1)^2$, where P_1 is the probability that *if* the site is unquenched, the probability that it will remain unquenched in the next time interval. As a result, in Eq. 3.1, $P_0(\tau)$ equals $(1-P_1)^2$, which gives an expression for the rate constant

$$k_1 = \frac{2\ln\left(\frac{1}{1-P_1}\right)}{\tau} \qquad \text{(Eq. 3.2)}$$

where k_1 is the forward/quenching rate constant. Similarly,

$$k_{-1} = \frac{2\ln\left(\frac{1}{1-P_2}\right)}{\tau} \qquad \text{(Eq. 3.3)}$$

Where k_{-1} is the reverse rate constant.

We simulated traces similar as those shown in Fig. 3.13 by randomly assigning k_1, k_{-1} and the number of empty sites using Matlab (see Appendix A). We then used HMM to analyze these traces and generate transition probability matrix. Both k_1 and k_{-1} are successfully recovered using our stochastic model.

The reaction rate constants for different quenchers can be calculated with Eq.3.2-3.3 from our large data sets and summarized in Table 3.1.

Table 3.1 Comparison of reaction rates for different quenchers

quencher	concentration	k_1 (1/s)	k_{-1} (1/s)	K
H_2O_2	20 μM	0.000 957	0.000 600	1.59
	50 μM	0.001 239	0.000 621	1.99
	100 μM	0.001 400	0.000 600	2.33
H^+	pH 4	0.000 808	0.001 130	0.71
	pH 2	0.001 297	0.001 138	1.13
	pH 1	0.001 539	0.001 142	1.34
$Fe(CN)_6^{3-}$	20 μM	0.005 478	0.003 997	1.37
initial quenching	20 °C	0.002 678	0.001 911	1.40
	45 °C	0.005 110	0.002 630	1.94

There are two factors that can influence the quenching rates for the same SWNT sample, the adsorption binding energy of the quencher molecule for SWNT and the quencher radius, particularly for metallic quenchers. For the species studied in this work, the former is dependent upon the redox potential of the quencher. From the literature, the standard redox potential (versus a normal hydrogen electrode: NHE) of H^+ and H_2O_2 is 0, and 1.8 V^{110} respectively. The more positive the potential, the greater the affinity of the quencher for electron density from the nanotube and thus the dwell time after adsorption on the surface is higher. Alternatively, the size of the quencher can apparently influence quenching rate. It is reported in the literature that for ionic metals with radii greater than 1$\overset{\circ}{A}$, the quenching efficiency increases with the increase of size[93]. The former property (redox potential) appears to be the dominant factor, with H_2O_2 yielding the largest quenching equilibrium constant for a concentration of 20 μM among the quenchers. (Note that the detection of H^+ is so insensitive that only with a concentration of 0.1M (pH 1) can its quenching equilibrium constant be of the same magnitude as H_2O_2.)

In summary, in this chapter, we have developed a biocompatible single-molecule sensing platform of SWNT embedded in collagen films. The quenching reactions caused by different reagents are studied. A stochastic model is proposed and used for comparison between the rate constants of different quenchers and different concentrations. A HMM algorithm is applied to discover the real states in each photoluminescence intensity traces. We find that on a single-molecule level, the stochastic quenching rate constant increases with the increase of the quencher concentration, and its redox potential while the reverse rate constant is generally independent of the quencher concentration. The ability to measure rate constants at the

single-molecule level using the collagen-SWNT film platform and the stochastic analysis

is important for future biosensing applications detailed in the next chapter.

4. Detection of Single Molecule H_2O_2 Signaling from EGFR Using SWNT

4.1 Introduction

Historically, H_2O_2 has been thought to have only a deleterious role in cell biology as a toxic metabolic waste product, or as part of the immune respiratory burst in response to microbial invasion[111]. New findings suggest that it is a messenger in normal signaling pathways: H_2O_2 production has been observed in response to stimulation with various growth factors, cytokines and other signaling molecules across many cell types, and is known to activate specific downstream targets[112]. The understanding of this emerging role for H_2O_2, and other reactive oxygen species (ROS), is hampered by their low concentration and short lifetime. Existing probes for H_2O_2 cannot map the entire transient signaling response over its duration with spatial resolution[113-115].

Our laboratory has pioneered the use of SWNT as fluorescent optical sensors for analytical detection from within living cells and tissues. Recent measurements by others[17] and our own laboratory[18] have extended the detection limit down to single molecules by analyzing the stochastic quenching of single molecules as they adsorb to the SWNT surface. In this chapter, we develop an array of such single molecule sensors specifically for H_2O_2 and show that we can image the molecular flux emanating from single living cells in real time with spatial precision, a demonstration that is impossible with any known sensor technology to date. We show that these arrays can image the signaling flux of living A431 human epidermoid carcinoma cells, and resolve several questions about H_2O_2 generation upon growth factor stimulation, including the membrane activity compared to far-field signal, spatial distribution, and through inhibition experiments, the chemical mechanism of the signal response. We show generally that

such arrays can mathematically distinguish between molecules generated at the array interface from the far-field signal, an important property for cellular analysis.
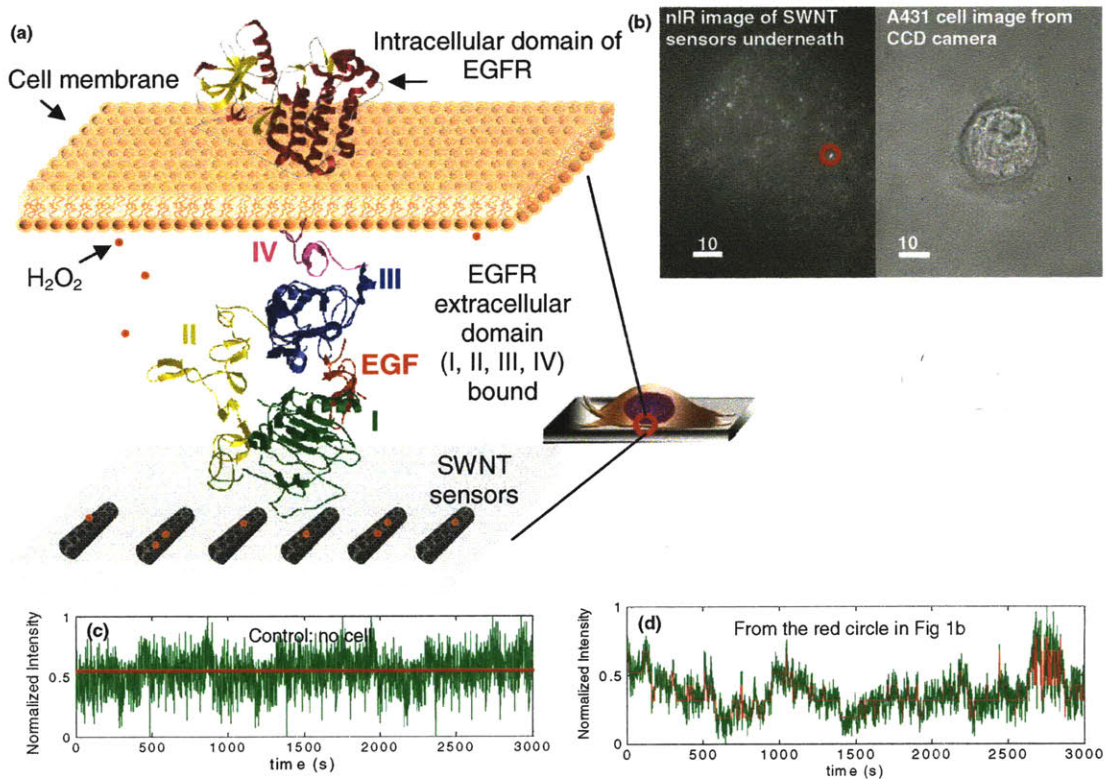
Figure 4.1 (a) A431 cell was cultured on the collagen-SWNT film. Zoomed from red circle: EGFR has an intracellular domain, a transmembrane domain and an extracellular domain (I, II, III, IV). The extracellular domain of EGFR binds to EGF, generating H_2O_2, part of which diffuses into the collagen film and quenches SWNT, the rest of which diffuses into the cell and induces cell signaling events such as phosphorylation. (b) A431 cell was cultured on the collagen-SWNT film where the SWNT sensors were excited by a 658 nm excitation laser at 1mW at the sample through Alpha Plan-Apo 100x/1.46 oil emersion objective. The fluorescence emission from SWNT was collected by the InGaAs nIR camera at 1 frame per second. The SWNT sensors embedded in the collagen film report the quenching events from H_2O_2 generated from EGF-EGFR binding. (c) The control trace from the control experiment where no cell was present showed no steps. (d) The fluorescence trace from the SWNT in the red circle in (a) showed reversible, stepwise quenching (green trace), modeled by HMM (red).

Growth factors are important signaling molecules that can regulate important events in cell development. Since its discovery by Stanley Cohen while investigating the effects of nerve growth factor some 50 years ago, epidermal growth factor (EGF) has become one of the most characterized growth factors regarding its physical and biological properties[116]. EGF is a single polypeptide chain of 53 amino acid residues, the structure of which is held together in 3D by 3 disulfide bonds in cysteine (Cys) (Fig. 4.1a)[116]. EGF is a general growth factor that can stimulate the cell growth, proliferation and differentiation by binding to EGFR, which is one of four transmembrane growth factor receptor proteins[117], including EGFR (HER-1 or c-erbB-1), HER2, HER3 and HER4. EGFR is a 170-kDa glycoprotein with an extracellular receptor domain, a transmembrane domain and an intracellular domain[118]. The extracellular domain of EGFR can be divided into four subdomains: I, II, III and IV, with I and III participating in binding[119] (Fig. 4.1a). The expression of EGFR ranges from 4×10^4 to 10^5 receptors per normal cell[116] while it is overexpressed in many cancer cells. For instance, in A431 cells, the expression of EGFR is around 10^6 receptors per cell[120]. EGF can bind to and activate EGFR, resulting in receptor dimerization at the cell membrane[118]. H_2O_2 is generated in the activation of EGFR[121]. Include summary of data from DeYula et al, not just reference.

The study of H_2O_2 generation from EGF stimulation is important in elucidating cell signaling pathways. H_2O_2 is a small, diffusive reactive oxygen metabolite in living systems that serves as a messenger in cellular signal transduction[112,122]. However, the current H_2O_2 measuring techniques have, in a way, made the elucidation of the complete pathway difficult. Several specific molecular probes[114,115] have made the measurement of H_2O_2 in living systems possible, but their slow time response (~30 min or more) of

organic dyes hinders real time spatial and temporal determination of the response[113].

Herein, we utilize SWNT arrays capable of single molecule detection of H_2O_2 to study its role in cell signaling before and after EGF stimulation on A431 cells and NIH-3T3 murine fibroblast cells in real time.

4.2 A Sensitive, Selective Platform for Single Molecule H_2O_2 Detection *In Vitro*

As has been detailed in 3.2.1, the nanotube sensor itself is selective for H_2O_2. The second property of our single molecule detector array is that they are embedded in a thin film, with 2 nm roughness (Fig. 4.2) and open porosity (average pore size = 30 nm) towards the SWNT. This means that in reality, only the most stable species emanating from the cell are detected. For example, singlet oxygen, superoxide anion and hydroxyl radicals have lifetimes of 4 μs[123], 1 μs and 1 ns respectively[124]. Singlet oxygen, superoxide anion and hydroxyl radicals no longer interfere beyond a distance of 90, 45 and 1 nm away from the generating source respectively after twice their lifetimes, assuming that the diffusion coefficient of each is one tenth in our film than in water. Because SWNT in the film are an average of 200 nm away from the interface, it is unlikely for these short lived species to diffuse into the film. The selectivity of our film, together with the diffusion calculation, result in an array of sensors specifically designed to detect single molecules of H_2O_2 in real time. We note that this does not by any means limit this approach exclusively to H_2O_2. Our recent work shows that by varying the chemistry of the encapsulating matrix[125], or by utilizing multiple orthogonal optical responses (multi-modality)[126], it is possible to selectively detect virtually any analyte emanating from the cell in this manner. Future work will underscore this point.
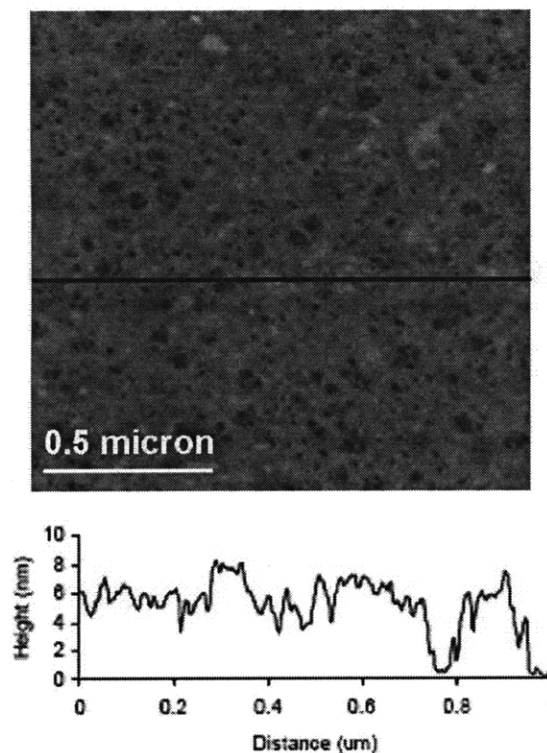
Figure 4.2

AFM image of the collegen film.

MFP-3D (Asylum Research) was used for tapping mode atomic force microscopy (AFM) imaging. Samples were directly deposited on a 75 mm × 25 mm glass slide (VWR International) and imaged using rectangular silicon tips (Olympus AC240TS) with a nominal spring constant of 2 N/m. Both topographic and height images were recorded during AFM analysis. Height analysis was performed using Igor Pro software.

4.3 Detection Single Molecule H_2O_2 Cellular Efflux

When no cells are plated onto the collagen-SWNT array, the result is a photoluminescence intensity of constant root mean square value. A Hidden Markov algorithm finds no quenched states outside of the noise floor as expected. SWNT sensors near or underneath plated A431 cells show discrete quenching transitions of the type observed previously[17,18]. Stepwise quenching and dequenching reactions are clearly observable (Fig. 4.1e), compared to the control experiment (Fig. 4.1d). Because the collagen-SWNT array has such high selectivity towards H_2O_2, we assign this flux of single molecules as H_2O_2 originating from cellular metabolic activity[112] and also non-specific receptor-ligand binding[127]. To further support this assignment, we use manganese oxide (MnO_2) to selectively catalyze the decomposition of H_2O_2 around the

90

A431 cells both with and without EGF stimulation, to show that the quenching reverses

significantly (Fig. 4.3) as the H_2O_2 is depleted.
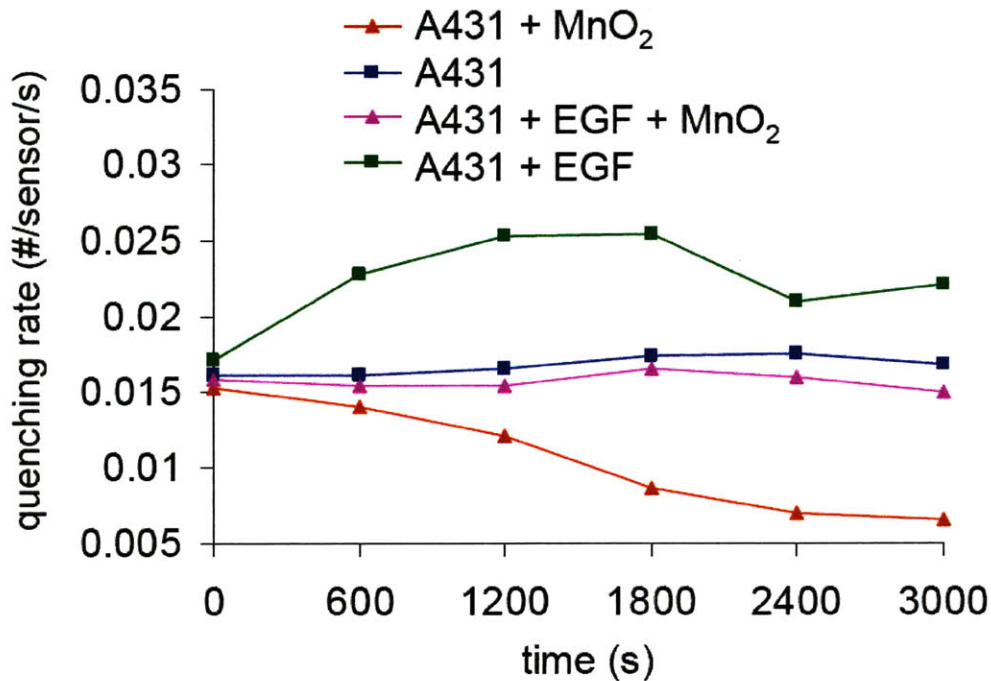
Figure 4.3 The real-time quenching rate for A431 cells with (red) and without (blue) the presence of MnO_2

4.4 Spatially Mapped Signal from EGF Stimulation

The Hidden Markov algorithm was applied to each SWNT signal in the array,

yielding the spatial and temporal detection of single molecules emitted from the cell in

real time. The typical observation time was 3000s and Fig. 4.4a-d describes the spatial

distribution of single molecule detection frequencies for both live (Fig. 4.4a, b) and fixed

(Fig. 4.4c,d) A431 cells after the addition of EGF (500ng/mL) at t = 0 using a specifically

written Matlab program. Each sensor was binned according to frequency into one of

sixteen color categories between 0 and 150 counts for Fig 4.4a-d and between 2 and 70

counts for Fig 4.4e. Note that the control array, exposed to 10 µM H_2O_2 in the absence of

cells, demonstrates a spatially random distribution of transition frequencies (Fig. 4.4e). However, when instead A431 cells are present, the frequency distribution possesses a sharp mode invariably confined to the region immediately under the cell. The behavior is seen for both live and fixed cells. The locations of these "hot spots" do not remain invariant over the course of the 3000 s experiment, but shift to alternate regions. The EGFR receptor lifetime[120] is approximately 30 min, long enough to prevent spatial averaging of the membrane signal. It is clear from these examples that the dominate contribution of the H_2O_2 flux comes from the A431 cells, and the data suggests that at any given time it is concentrated at specific locations on the array, unlike the case of a uniformly exposed control.
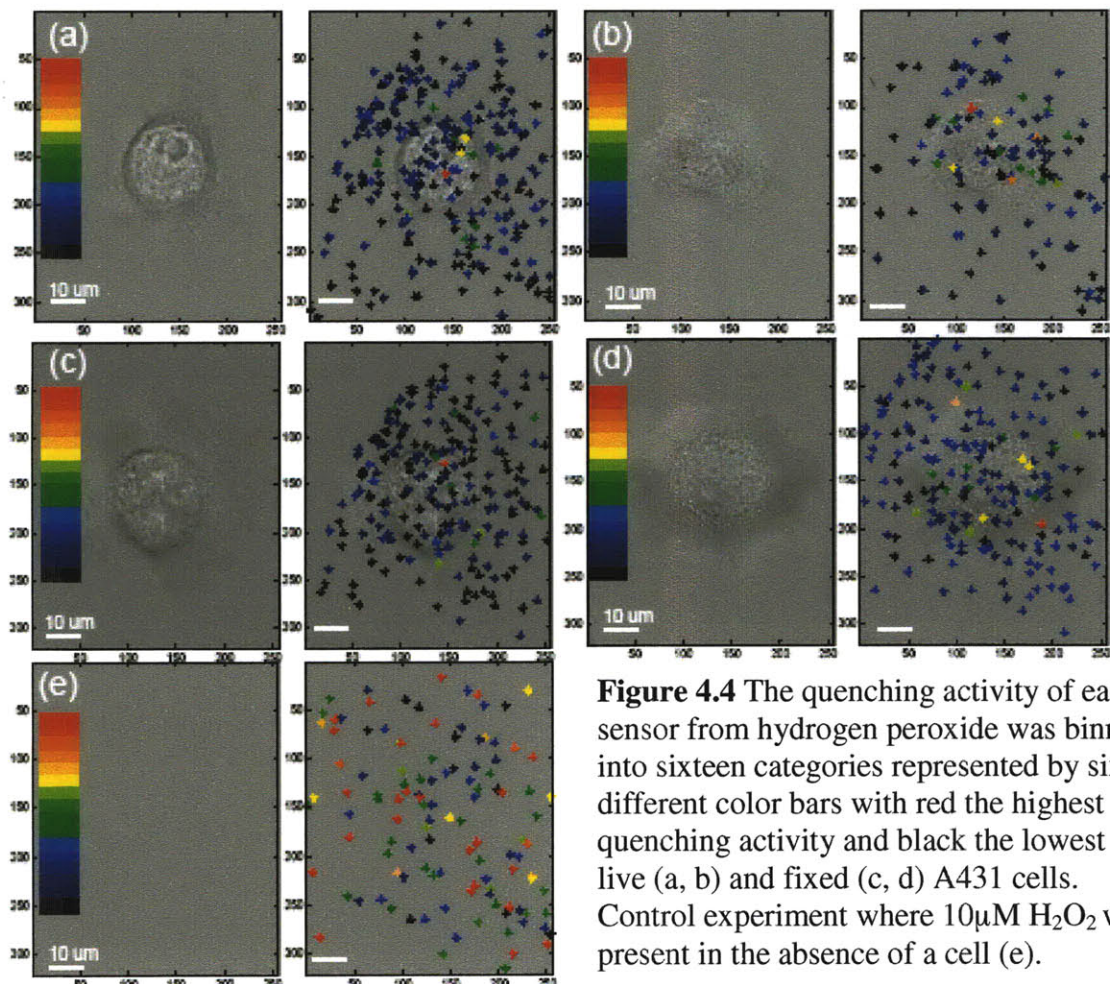
Figure 4.4 The quenching activity of each sensor from hydrogen peroxide was binned into sixteen categories represented by sixteen different color bars with red the highest quenching activity and black the lowest for live (a, b) and fixed (c, d) A431 cells. Control experiment where 10μM H_2O_2 was present in the absence of a cell (e).

4.5 Real-time Quantitative Analysis from EGF Stimulation across Two Cell Lines

First, we analyze the total dynamic count rate of each single cell in response to EGF stimulation. The quenching rate was calculated in real time for EGF stimulation (500ng/mL EGF was added at t=0) on live 3T3 (Fig. 4.5a) and live/fixed A431 cells (Fig. 4.5b). Compared to the no cell control and unstimulated cell data, the quenching rate of both A431 and 3T3 cells has been increased from EGF stimulation. A431 cells with a higher EGFR density have a much higher quenching rate than 3T3 cells. As can be seen from Fig. 4.5a-b, the behaviors of single A431 cells after EGF stimulation are similar: the quenching rate increased rapidly right after stimulation. However, the time point of maximal response ranges from 600s to 1800s after stimulation. There is no significant difference between live and fixed A431 cells. Removal of EGF decreases the quenching (Fig. 4.6). Compared to ensemble measurements on thousands of cells, our platform allows real-time quantification on single isolated cells for the first time. To confirm that the above results correlated with overexpression of EGFR, we then compared the EGFR density in 3T3 cells and A431 cells. Both cell lines were immunostained using rabbit polyclonal to EGFR as the primary antibody and Alexa Fluor 568 donkey anti-rabbit IgG as the secondary antibody. As can been seen in the confocal images (Fig. 4.5c, d), A431 cells express much more EGFR than 3T3 cells. From a calculation on the immunostaining images of 100 cells, the EGFR density of A431 cells is approximately 10 times that of 3T3 cells, consistent with the literature[116,120].
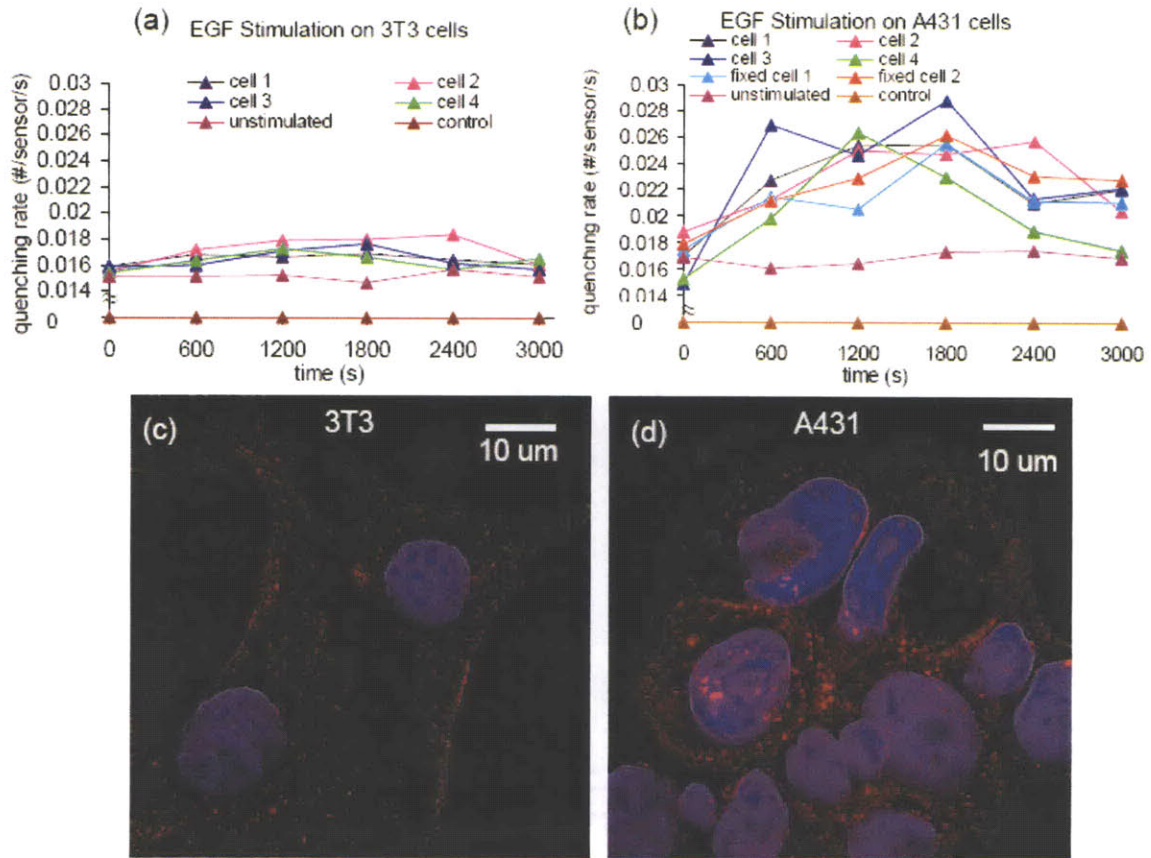
Figure 4.5 SWNT quenching is EGFR density dependent. The real-time quenching rate (#/sensor/s) for live 3T3 cells (a) and live/fixed A431 cells (b). Representitive confocal images for 3T3 cells (c) and A431 cells (d) with EGFR (red) labeled with rabbit polyclonal to EGFR and Alexa Fluor 568 donkey anti-rabbit IgG. The nuclei (blue) is labeled with 4',6-diamidino-2-phenylindole (DAPI).
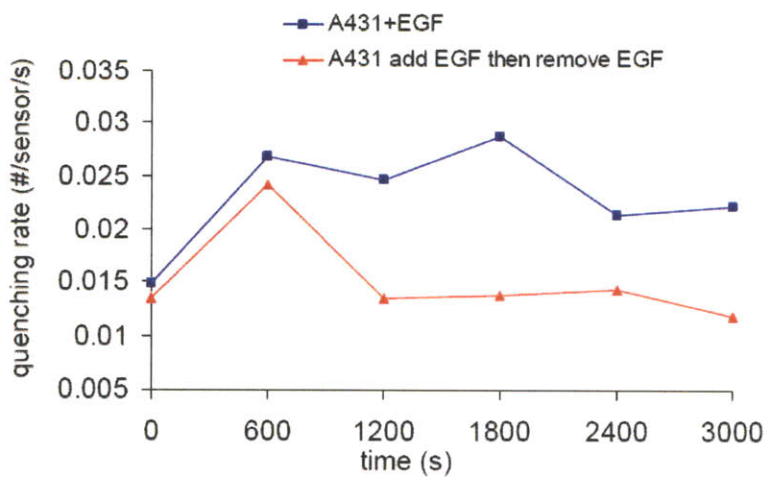
Figure 4.6

The real-time quenching rate for EGF removal after EGF stimulation (red) compared to the control (blue).

4.6 Far-field Component Subtraction and Local Generation from the Membrane

An array of sensors capable of detecting discrete, single molecules has the following unique property: it is possible to distinguish between those generated at the interface and those comprising a far-field component with no memory of origination. Molecules that have equal probability of capture on any element of the array constitute a statistically binomial process, contributing a binomial distribution of counts to the array response. A kinetic Monte Carlo simulation of 10^5 H_2O_2 molecules randomly binned into a sensor array consists of 300 sensors (n = 300) produces a binomial distribution in count rates[1] (Fig. 4.7a-b).
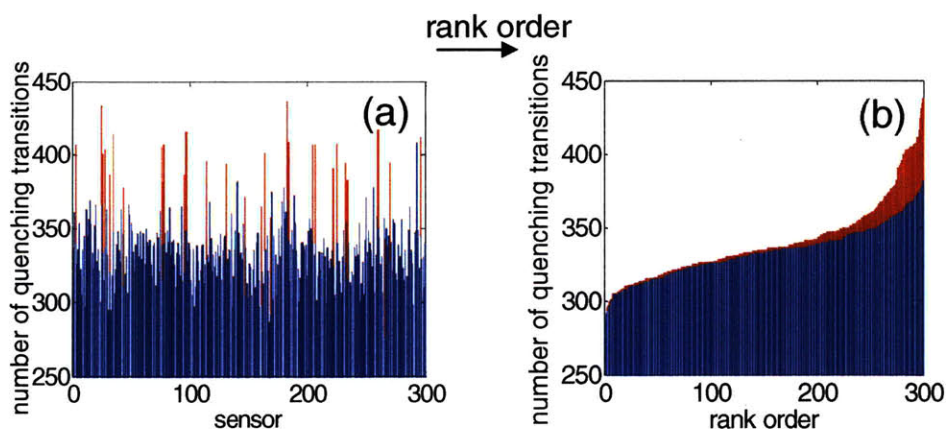
Figure 4.7 (a) Simulation of sensor response (number of quenching transitions) on 10^5 H_2O_2 randomly falling onto 300 sensors (blue), with additional response to membrane generation (red). (b) Rank ordered sensor response from (a).

Rank ordering the sensor responses from lowest to highest capture rate constructs the cumulative distribution. Let x be the number of sensors having a response less than y, so that $\dfrac{x(y)}{n}$ is then the probability of finding a sensor with a number of counts less than

y. For the case of equal capture probabilities, the rank ordered response is a modified

Gamma distribution (Fig. 4.8):

$$x = \frac{n \int_0^y e^{-t} t^{a-1} dt}{\int_0^\infty e^{-t} t^{a-1} dt} = \frac{n\Upsilon(a, y)}{\Gamma(a)} = nP(a, y) \qquad \text{(Eq. 4.1)}$$

Where Υ, Γ and P represents the lower incomplete, ordinary and regularized Gamma

functions respectively with a the mean value of y.
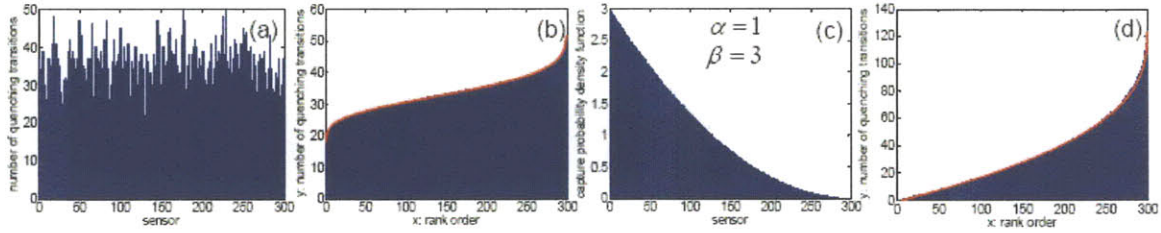
Figure 4.8 (a) Simulation of the sensor response (number of quenching transitions) for 300 uniformly distributed random sensors. (b) The simulated sensor response (blue bars) can be described by gamma incomplete function (red curve) after rank ordering. (c) The capture probability density function with beta distribution ($\alpha = 1$ and ß = 3) for 300 sensors. (d) The simulated sensor response with a capture probability distribution described in (c), after rank ordering (blue bars), can be described by beta binomial function (red curve).

On top of this far-field signal, molecules generated near the array surface (i.e. at the cell

membrane surface) are easily distinguished. The algorithm for extracting this interfacial

generation at the interface simply accounts for non-binomial contributions to the

frequency distribution. The local response, $y_{local}(x)$, is:

$$y_{local}(x) = y(x) - P^{-1}(a, \frac{x}{n}) \qquad \text{(Eq. 4.2)}$$

The mean value a can be found by computing the slope of the experimental data in the

$x \rightarrow 0$ limit:

$$\frac{\partial y}{\partial x} = \frac{\Gamma(a)}{n y^{a-1} e^{-y}} \quad (\text{from } \frac{\partial \Gamma(a, y)}{\partial y} = -y^{a-1} e^{-y})$$

It can be shown from Monte Carlo simulation that membrane generation near the array interface of sufficient activity always biases the rank ordered response to the highest activity sensors (Fig. 4.7a-b). As a result, a small number of data points at $x \rightarrow 0$ are enough to extract the far-field component (Eq. 4.1) from any experimental curve with the membrane generation recovered from Eq. 4.2. A practical sensor array constructed from SWNT embedded in a collagen matrix as described above has a distribution of sensor probabilities as each sensor varies in distance and orientation from the interface. A beta distribution is a generic, empirical function that can describe this variation (see Appendix D). It has the advantage that the far-field component then becomes a cumulative beta binomial distribution (see simulation and fit in Fig. 4.8c-d), and an analogous deconvolution can be derived (Fig. 4.9a-b).
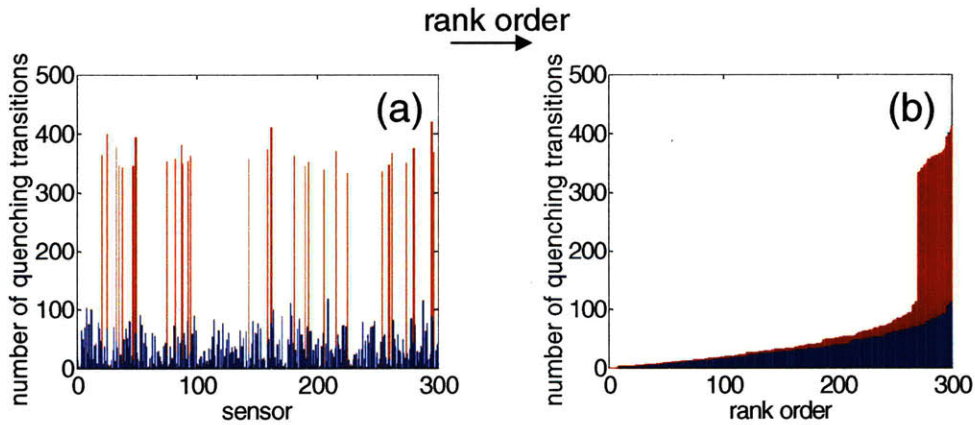
Figure 4.9 (a) Simulation of sensor response on 10^5 H_2O_2 falling onto 300 sensors following beta distribution (blue), with additional response to membrane generation (red). (b) Rank ordered sensor response from (a).

The rank ordered sensor responses of SWNT-collagen arrays exposed to constant (uniform) concentrations of H_2O_2 from 10 to 100 μM are described by beta binomial distributions with parameters α $=1.2 \pm 0.15$ and ß $= 3.0 \pm 0.12$ from control experiments. These parameters were used to correct the measured responses for the variation of capture sensitivities of each SWNT.

Membrane activities on single live, fixed A431 cell and live 3T3 cells before and after the EGF stimulation over 3000s were extracted from the above algorithm (Fig. 4.10a-c). Before EGF stimulation, the local activity is negligible. After EGF stimulation, the membrane generation observed for both live and fixed A431 cells, however not for live 3T3 cells.
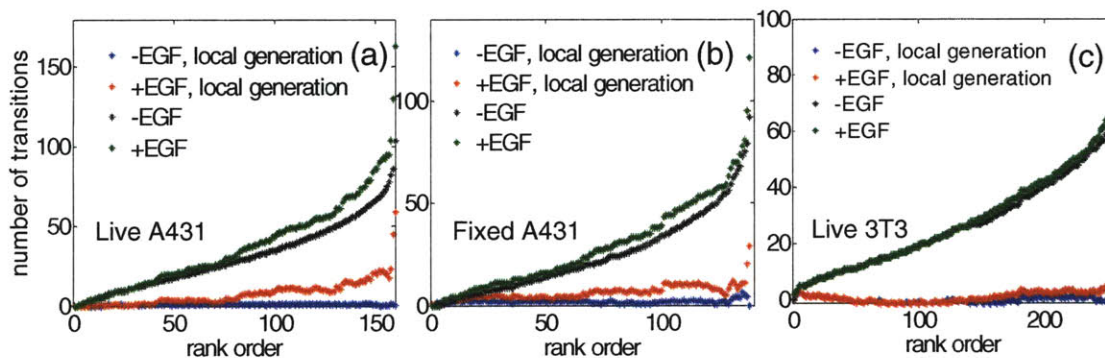
Figure 4.10 After far-field component subtraction from the rank ordered sensor response (dark, -EGF; green, +EGF), the membrane generation before (blue, star) and after (red, star) EGF stimulation for live (a), fixed (b) A431 cell and live 3T3 cell (c).

The increased activities after EGF stimulation in the unit of number of quenching transitions per sensor are summarized in Table 4.1.

98

Table 4.1 Number of quenching transitions per sensor from receptors alone calculated for live, fixed A431 cells and live 3T3 cells.

Cell type	Number of quenching transitions per sensor
Live A431 cell #1	6.6
Live A431 cell #2	4.0
Live A431 cell #3	5.0
Live A431 cell #4	7.5
Fixed A431 cell #1	4.5
Fixed A431 cell #2	7.8
A431 cells average	6.0
Live 3T3 cell #1	1.0
Live 3T3 cell #2	1.1
Live 3T3 cell #3	1.1
Live 3T3 cell #4	1.0
3T3 cells average	1.1

For A431 cells after simulation, the local H_2O_2 concentration is determined

through calibration to be 2μM using control experiments in the cell-free system (Fig.

4.11).

$$y = 0.2618x + 0.0283$$

(y-axis: 1/transitions, x-axis: 1/concentration (1/uM))
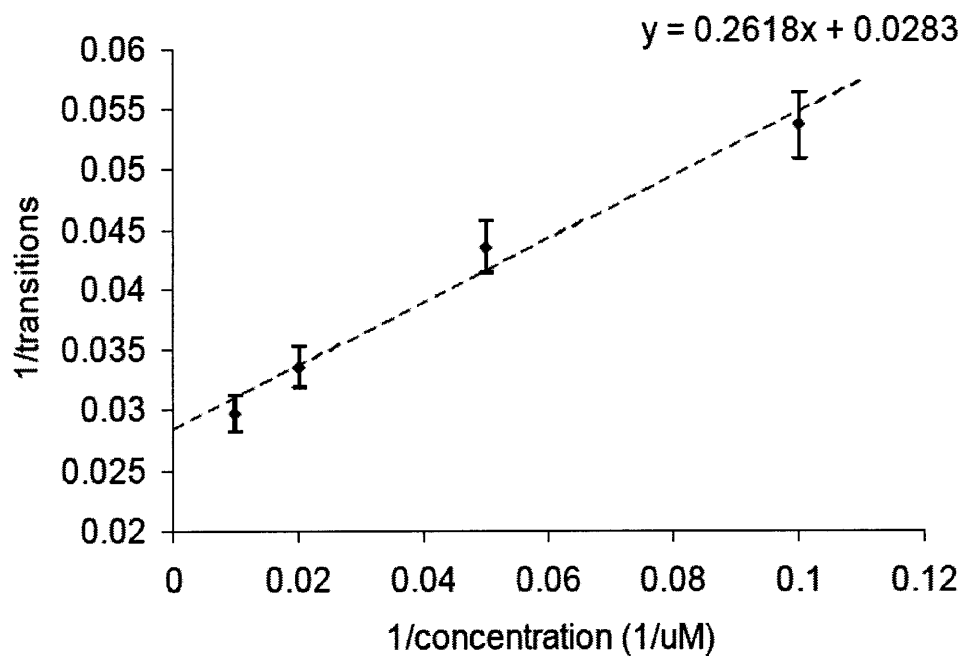
Figure 4.11 The inverse of quenching transitions (y) and the inverse of H_2O_2 concentration (x) can be described by y=0.2618x + 0.0283, calibrated from the controls.

The local H_2O_2 generation rate from each membrane source is then 0.04 nmol/min

after correcting for diffusion from the model derived below (Fig. 4.12).
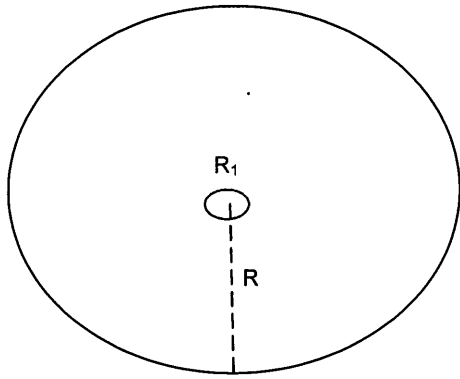
Figure 4.12 Diffusion model

k: the hydrogen peroxide generation rate at $r=R_1$
D: diffusion coefficient of hydrogen peroxide
R: radius of sphere
R_1: radius of the hydrogen peroxide generation source
c: hydrogen peroxide concentration

Conservation Equation for a spherical particle

$$\frac{\partial c}{\partial t} = \frac{D}{r^2}\frac{\partial}{\partial r}(r^2\frac{\partial c}{\partial r})$$

Boundry conditions:

B.C.1) $\quad D\frac{\partial c}{\partial r}(R_1,t) = -\frac{k}{4\pi R_1^2}$

B.C.2) $\quad \frac{\partial c}{\partial r}(r \to \infty, t) = 0$

The time scale $R^2/D=3.6\times10^{-6}$ s $<<$ observation time. So the system reaches steady state instantly.

$$c = \frac{k}{4\pi Dr}$$

$$k = 4\pi DRc$$

4.7 A Consistent H_2O_2 Signal Generation Mechanism

The spontaneous or catalytic breakdown of superoxide anions is considered to be the source of H_2O_2 in many biological pathways, not only for immune cells, but also in a variety of eukaryotic cells[112]. Superoxide anions can be produced by the partial reduction of oxygen by cytochrome c oxidase in mitochondria[112] or by membrane-associated NA(D)PH oxidase[114]. Extensive literature has shown that EGF stimulated H_2O_2 generation originates from NA(D)PH oxidase instead of mitochondria for various nonphagocytes, including A431 cells[114,128,129]. Growth factors like EGF induce the formation of a complex on NA(D)PH oxidase to promote the electron transfer from NA(D)PH to molecular oxygen[129]. Fixation of A431 cells using 4% paraformaldehyde were designed to remove the influence of the mitochondria[130] in our experiments, as has been used in the literature to kill the cells without affecting the binding abilities of EGFR[127]. The fact that we see no quantitative difference between live and fixed A431 cells in their EGF inducible membrane generation (Table 4.1) is consistent with the all existing literature where mitochondria do not affect the EGF-induced H_2O_2 generation. In addition, our array platform of single molecule sensors allows for the signaling flux from the cell to be differentiated from a diffuse far-field component for the first time, and can therefore inform the discussion of the nature of the H_2O_2 signal. Our analysis above confirms that the H_2O_2 that increases in response to EGF binding is generated at the membrane and not in the cell interior (Fig. 4.10a-c). Recently, DeYulia and co-workers demonstrated that the H_2O_2 production is EGFR-ligand-dependent in A431 cells[127], where the inhibition of EGFR phosphorylation did not affect the H_2O_2 generation. At this point, both the signaling network post-NA(D)PH oxidation, and how the activation of

NA(D)PH oxidase connects with the EGFR-ligand-dependent generation, is still unclear in the literature.

It is also not clear what catalytic portion of EGFR may be responsible for membrane H_2O_2 generation in the work by DeYulia and co-workers[127]. Tryptophan (Trp) is proposed to be responsible for the conversion of singlet oxygen to H_2O_2 in antibodies[131]. This antibody-mediated process is triggered upon binding of singlet oxygen to conserved binding sites within the antibody fold[132], where the antibody serves as the catalyst, stabilizing the intermediate (H_2O_3) and directing its conversion to H_2O_2. Trp is present in both EGF[116] (Trp 49, Trp 50) and EGFR[133] (Trp 140, 176, 453, 492) (Fig. 4.1a). If lacking these Trp residues, EGFR does not bind ligand with high affinity[133]. It is possible that EGFR, upon binding with EGF, allows greater access to sites on the receptor itself that catalyze the conversion of singlet oxygen to H_2O_2. To explore this, 1 mM sodium azide (NaN$_3$), a scavenger of singlet oxygen[134], was added to fixed A431 cells with and without the presence of EGF and the single molecule efflux of H_2O_2 was again recorded. Compared to the un-stimulated control (green curve, Fig. 4.13), NaN$_3$ greatly diminished both the local and far-field portions of the H_2O_2 response to EGF (black and red curve, Fig. 4.13).
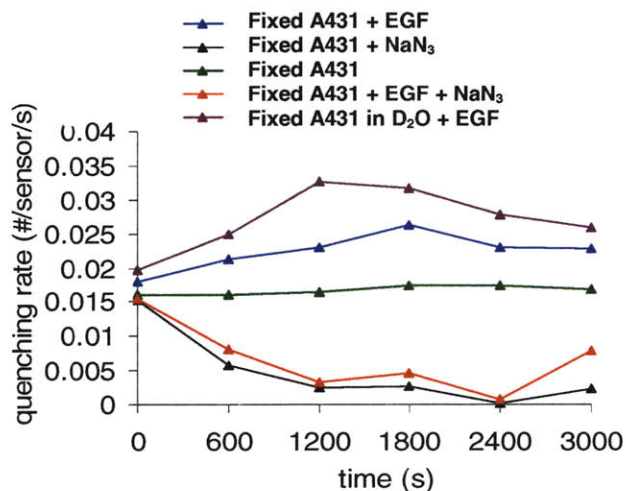
Figure 4.13 The real-time quenching rate for fixed A431, before (green) and after (blue) EGF stimulation. Sodium azide decrease the quenching, with (red) and without (black) EGF. Extending the singlet oxygen lifetime using D_2O increases the quenching (purple).

In previous studies, the level of H_2O_2 before and after EGF stimulation is not affected when shutting down the mitochondria[128,129]. The fact that we were able to observe an obvious decrease in H_2O_2 level even below the basal level when adding NaN_3 before and after EGF stimulation, and an increase in H_2O_2 level when extending the lifetime of singlet oxygen, supports a complex pathway involving singlet oxygen.

One possible signaling network that may explain this more complex response starts from superoxide anion, which is produced from the reduction of molecular oxygen by NAD(P)H oxidase in A431 cells (Fig. 4.14)[128,132].

$$NAD(P)H + 2O_2 \xrightarrow{NAD(P)H\ oxidase} NAD(P)^+ + H^+ + 2O_2^{\bullet-} \qquad \text{(Reaction 4.1)}$$
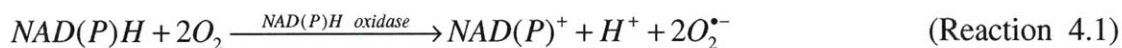
We further performed inhibition experiment using NA(D)PH oxidase and EGFR inhibitor (Fig. 4.14), and we found that consistent with our speculation, NA(D)PH oxidase inhibitors prevent H_2O_2 from forming while EGFR inhibitor has no effect on the H_2O_2 produced.
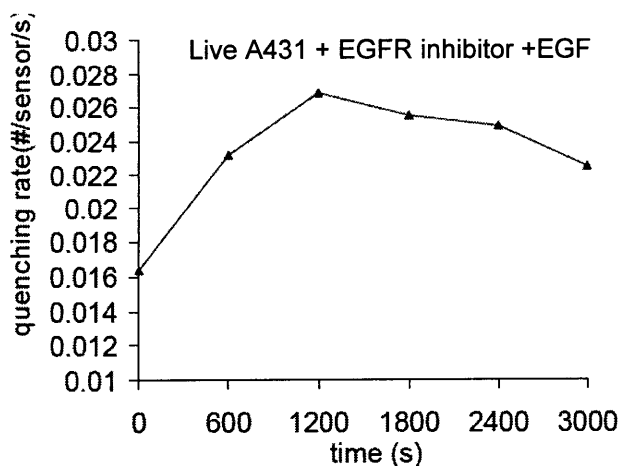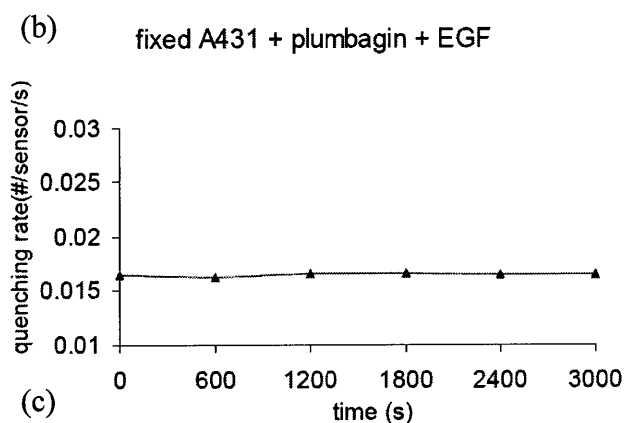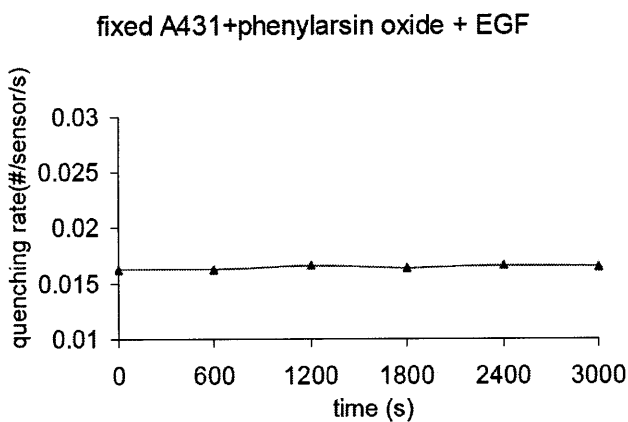
Figure 4.14

The NAD(P)H inhibitors, phyenylarsin oxide (10 μM) (a) and plumbagin (10 μM) (b) quenches H_2O_2 generation from EGF stimulation in fixed A431 cells.

The EGFR kinase inhibitor, Butein (65 μM), does not prevent the H_2O_2 from generating in A431 cells (c).

EGF was found to increase the production of superoxide anion in A431 cells while an inhibitor of NAD(P)H oxidase halts this mechanism in a manner that was also mitochondria independent[128]. This observation, together with the previous known EGF-EGFR induced NAD(P)H oxidase activation mechanism for EGF stimulated A431 cells from numerous literature[114,128,129], and our inhibition experiments (Fig. 4.14), supports Reaction 1. Superoxide anion can then be decomposed by superoxide dismutase (SOD). It has been found that SOD is a master regulator of growth factor signaling and the inhibition on SOD1, which is an abundant copper/zinc enzyme found in the cytoplasm, increases the steady-state levels of superoxide and decreases the levels of H_2O_2 in A431 cells[135]. These reactions are rapid and occur with a diffusion limited reaction rate.

$$2O_2^{\bullet-} + 2H^+ \xrightarrow{\quad SOD \quad} {}^1O_2 + H_2O_2 \text{ 136}$$
(Reaction 4.2)

$$2O_2^{\bullet-} + 2H_2O \xrightarrow{\quad SOD \quad} O_2 + H_2O_2 + 2^-OH \text{ 137}$$
(Reaction 4.3)
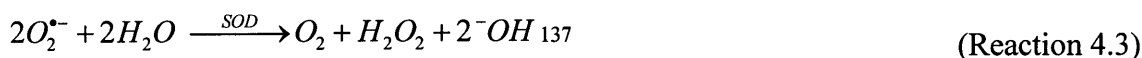
Transition metal ions such as iron or copper can catalyze the reduction of H_2O_2 by superoxide anion[138-140].

$$O_2^{\bullet-} + H_2O_2 \xrightarrow{\quad transition \ metal \ ions \quad} {}^1O_2 + {}^\bullet OH + OH^-$$
(Reaction 4.4)
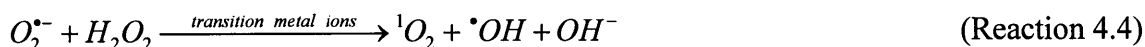
Singlet oxygen can decay to the ground state oxygen. It has been shown that the decay of singlet oxygen is determined by its interactions with water in the cell and not by interactions with other cell constituents with a decay rate constant of 3×10^5 s^{-1} [141].

$$^1O_2 \xrightarrow{\quad water \quad} O_2$$
(Reaction 4.5)

Ferrous also reacts with H_2O_2, known as the Fenton reaction[142].

$$Fe^{2+} + H_2O_2 \longrightarrow Fe^{3+} + {}^\bullet OH + OH^-$$
(Reaction 4.6)

$$Fe^{3+} + O_2^{\bullet-} \longrightarrow Fe^{2+} + O_2 \qquad \text{(Reaction 4.7)}$$

Upon EGF stimulation, singlet oxygen is converted into H_2O_2 catalyzed by EGF-EGFR[143,144].

$$2\,^1O_2 + 2H_2O \xrightleftharpoons{\; EGF-EGFR \;} 2H_2O_2 + O_2 \qquad \text{(Reaction 4.8)}$$

The proposed overall reaction network is summarized in Fig. 4.15.
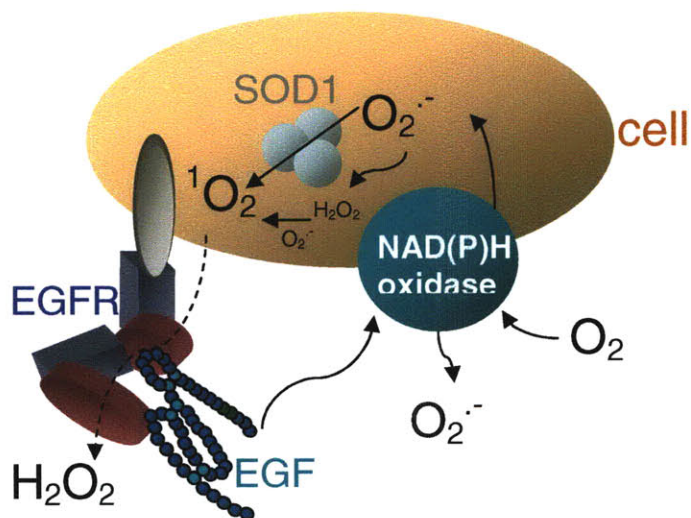
Figure 4.15 Proposed H_2O_2 generation pathway.

From solving the proposed pathway numerically (with the initial values for *in vitro* ROS obtained from the literature[145]: superoxide, ~1nM, H_2O_2, 1μM, singlet oxygen, ~1nM), the concentration of superoxide and H_2O_2 increases with the addition of EGF (Fig. 4.16a), consistent with the experimental observations by us and others[114,121,128]. The

addition of NaN₃ causes decrease of H_2O_2 (Fig. 4.16b), even below the initial value, consistent with our observations in Fig. 4.13. The heavy water, in which singlet oxygen has a longer life time, allows a higher level of H_2O_2 to generate upon EGF stimulation in fixed A431 cells (Fig. 4.13).
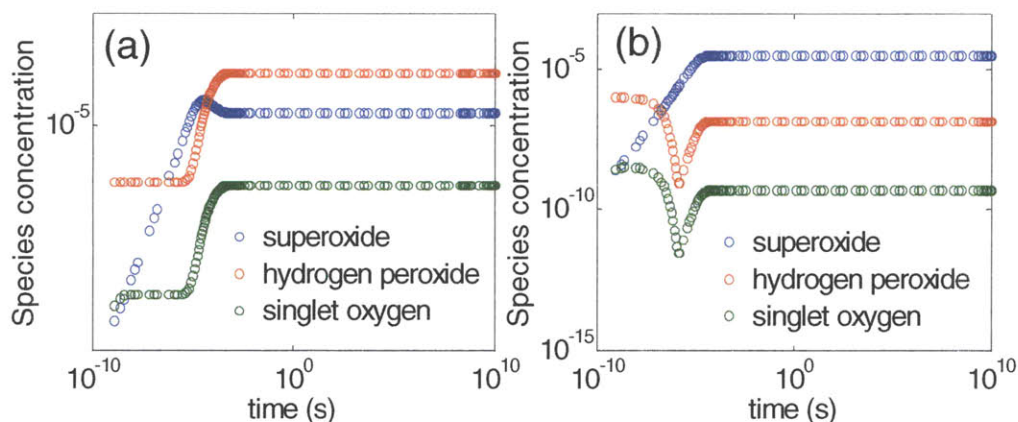
Figure 4.16 (a) The concentration profiles on log-log scale for different species from solving Reaction 4.1-4.8. (b) The concentration profiles on log-log scale for different species considering the NaN₃ effect when solving the reaction network.

4.8 Conclusions

In conclusion, an array of SWNT sensors has been used to image, for the first time, the incident flux of H_2O_2 molecules that stochastically absorb and quench the emission with spatial and temporal resolution. Notably, arrays of this type can distinguish between molecules originating near an interface and those with no memory of origination, attributed as the far-field components. The signaling activity of EGFR on single A431 cells has been successfully measured using this sensor array. We find that each local, membrane source, which consists of EGF-EGFR cluster and affected by NA(D)PH oxidase and several important enzymes, produces on average 0.04 nmol/min H_2O_2 over a

period of 50 min after exposure to EGF in A431 cells. Corresponding inhibition experiments suggest a mechanism whereby water oxidizes singlet oxygen at a catalytic site on the receptor itself, generating H_2O_2 in response to receptor binding. An EGFR-mediated H_2O_2 generation pathway that is consistent with all current and previous findings has been proposed and numerically tested for consistency. While the pathway that we proposed here is compelling, future work is necessary in order to conclusively rule out alternate mechanisms.

5. Conclusions and Future Work

In this work, we first used a broad spectrum of analytical methods (Raman, DLS, AFM, etc.) to understand the structure of biopolymer-wrapped SWNT and the basic sensing mechanisms based on the reversible red shifting of the emission energies from the nIR photoluminescence under various conditions, by adding divalent ions or temperature cycling. We found that the optical modulation is linked to specific secondary structure changes in the adsorbed biopolymers. Consistent with the experimental observations is a mechanism that proceeds via a competitive, stepwise process of partial desorption of the biopolymer along the length of SWNT. A two-state mathematical model quantitatively describes the equilibrium for various divalent ions binding to biopolymers adsorbed at the nanotube surface. Of all the DNA sequences and divalent ions tested, this type of sensor is most sensitive to $HgCl_2$, with an ion sensitivity in the order $Mg^{2+} < Ca^{2+} < Co^{2+} < Cu^{2+} < Hg^{2+}$. This is very important for future development of using SWNT as *in vitro* biosensors.

One of the most important issues in developing SWNT sensors for *in vitro* applications is, how SWNT interact with cellular systems, and if they are cytotoxic. We have developed an unorthodox method of studying this problem by tracking the non-photobleaching SWNT in real time by using a single particle tracking method. Over 10,000 individual trajectories of SWNT were tracked as they are incorporated into and expelled from NIH-3T3 cells in real time on a perfusion microscope stage. An analysis of mean square displacement allows the complete construction of the mechanistic steps involved from single duration experiments. We observe the first conclusive evidence of SWNT exocytosis and show that the rate closely matches the endocytosis rate with

negligible temporal offset, thus explains why SWNT are non-cytotoxic for various cell types at a concentration up to 5 mg/L, as observed from our live-dead assay experimental results. Further, we studied the cellular uptake and expulsion rates of length-fractionated SWNT from 130 to 660 nm in NIH-3T3 cells using this method. We developed a quantitative model to correlate endocytosis rate with nanoparticle geometry that accurately describes our data set and also literature results for Au nanoparticles. The model asserts that nanoparticles cluster on the cell membrane to form a size sufficient to generate a large enough enthalpic contribution via receptor ligand interactions to overcome the elastic energy and entropic barriers associated with vesicle formation. Interestingly, the endocytosis rate constant of SWNT (10^{-3} min^{-1}) is found to be nearly 1000 times that of Au nanoparticles (10^{-6} min^{-1}) but the recycling (exocytosis) rate constants are similar in magnitude (10^{-4} to 10^{-3} min^{-1}) for poly(D,L-lactide-co-glycolide), SWNT, and Au nanoparticles across distinct cell lines. The total uptake of both SWNT and Au nanoparticles is maximal at a common radius of 25 nm when scaled using an effective capture dimension for membrane diffusion. The ability to understand and predict the cellular uptake of nanoparticles quantitatively should find utility in designing nanosystems with controlled toxicity, efficacy and functionality.

The 1D quantum confinement of photogenerated excitons in SWNT can amplify the detection of molecular adsorption to where single-molecule discrimination is realizable, even from within living cells and tissues. Toward this aim, we developed a type I collagen film, similar to those used as 3D cell scaffolds for tissue engineering, containing embedded SWNT capable of reporting single-molecule adsorption of quenching molecules, and we used a nIR Total Internal Reflection Fluorescence (TIRF)

Microscope. We utilize Hidden Markov Modeling to link single-molecule adsorption events to rate constants for many different analytes and we found that our sensor is selectively sensitive to H_2O_2. Generally, the quenching rate constants increased with an increase in the redox potential of the quencher, indicating that electron transfer increases the adsorption equilibrium constant on the nanotube surface and, hence, the dwell time of the quencher. These developments provide the material, analytical and mechanistic groundwork for SWNT to function as single-molecule stochastic biosensors.

Finally, we used this class of single-molecule sensors to study the single molecule fluxes of H_2O_2 from living cells. We used this platform to study H_2O_2 signaling in A431 human skin carcinoma cells and particularly the local generation rate from the membrane and the associated signaling pathway production in living cells. An emerging concept in cell signaling is the natural role of reactive oxygen species, such as H_2O_2, as beneficial messengers in redox signaling pathways. Despite growing evidence, the nature of H_2O_2 signaling is confounded by the difficulty in tracking it in living systems both spatially and temporally at low concentrations. An array of near infrared fluorescent SWNT is capable of recording the discrete, stochastic quenching events that occur as H_2O_2 molecules are emitted from individual A431 human epidermal carcinoma cells in response to epidermal growth factor (EGF). We show mathematically that such detection arrays have the unique property of distinguishing between molecules originating locally on the membrane from other contributions. We find that EGF induces on average 0.04 nmol H_2O_2/min/(active receptor cluster) over a period of 50 min. This platform promises a new approach to understand reactive oxygen signaling at the cellular level.

Notably, we have worked out the mathematics of distinguishing local generation (near-field signal) from the other contributions (far-field signal) for *any* sensor arrays, which can be adapted to many classes of sensor arrays and applications.

In addition, we tried to improve the current platform by increasing the PL from individual nanotubes. We used dithiothreitol (DTT), a reducing agent, to enhance the fluorescence of individual nanotubes in the collagen film. The collagen film was imaged using a fluorescence microscope (Carl Zeiss, Axiovert 200), with a CCD camera (Carl Zeiss, ZxioCam MRm) and 2D InGaAs array (Princeton Instruments OMA 2D). Movies were acquired using the WinSpec data acquisition program (Princeton Instruments) with 1 frame/s with 1s exposure time per frame. Samples were excited by a 658 nm laser (LDM-OPT-A6-13, Newport Corp) at 35 mW. After stable fluorescence intensity was observed, 500 μL of DTT solution was added to 1500 μL of 0.1x PBS buffer on top of the collagen film to reach the desirable final concentration. The large volume of 500 μL was used to avoid slow, inhomogeneous diffusion. Preliminary single-molecule studies show that DTT increases the PL of individual nanotube, and this PL enhancement is stable until the removal of DTT (Fig. 5.1).
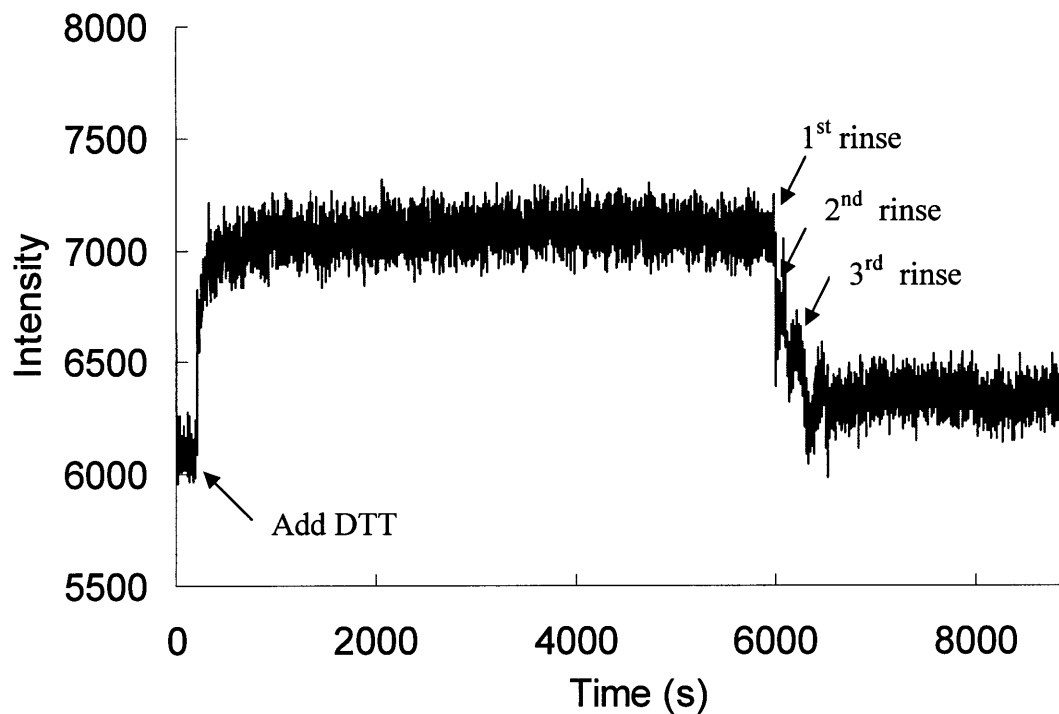
Figure 5.1 The average intensity of 150 nanotubes increases with the addition of 20 mM DTT at t = 200 s. The intensity increase persists until DTT is removed, after a sequence of three rinses with DTT free buffer.

In fact, not only did the individual nanotubes become brighter, some nanotubes that were invisible before the addition of DTT became visible after the addition (Fig. 5.2).
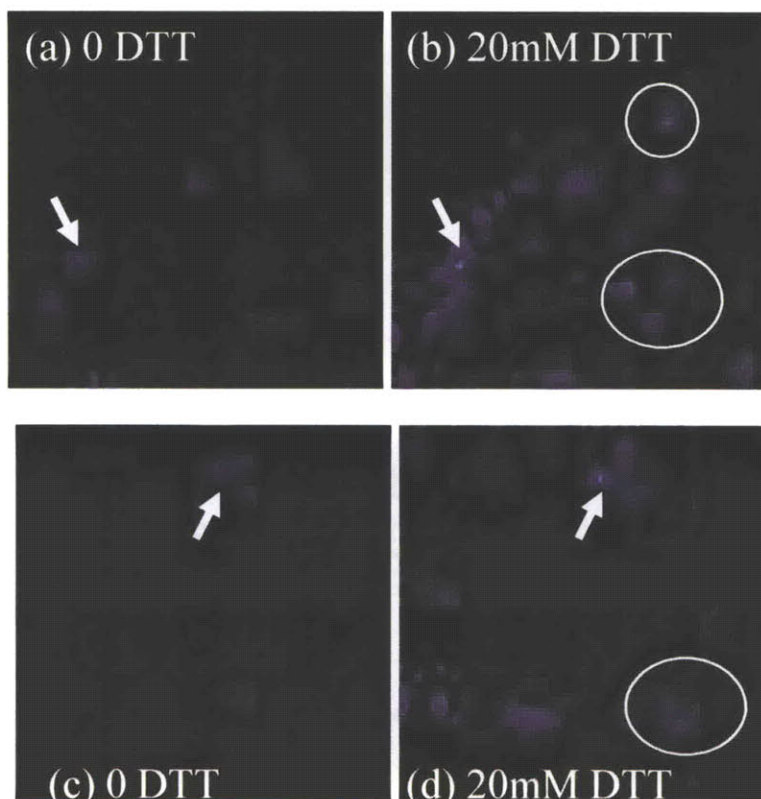
Figure 5.2 Some example comparisons on the PL of individual nanotubes before (a, c) and after (b, d) the addition of 20mM DTT. Some nanotubes became brighter (indicated by the arrows), some nanotubes that were invisible before DTT became visible (indicated by the circles).

The histogram shown in Fig. 5.3 indicates that 20mM DTT increases the fluorescence of individual nanotubes by ~30%. This method inevitably increased the number of nanotubes that are visible and thus enlarged our data sampling size per experiment. We believe that this reducing agent can remove doped holes at defect sites on the nanotube along its sidewall through electron donation, resulting in the enhancement on the fluorescence[146].
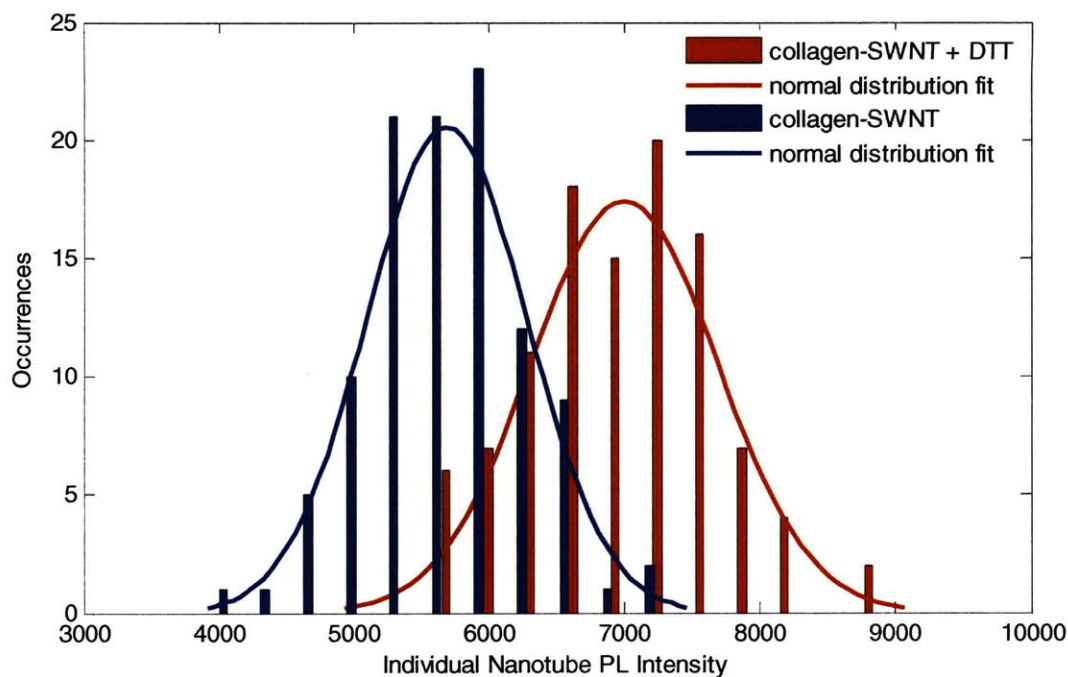
Figure 5.3 Histogram for the PL intensity distribution of 105 individual nanotubes brightened by 20mM DTT in collagen film.

We then seek out ways to incorporate DTT into the collagen film. We tried different ratios of DTT to SWNT in the procedure of making the film. We found that with 8mg/L of SWNT in the 500uL of solution before evaporation, 20mM yields the best result (concentrations above 20mM before evaporation yield inhomogeneous film). We further tested the interactions between this improved nanotube sensors and H_2O_2. Three different concentrations of H_2O_2 were used, 20 µM, 50 µM and 100 µM. The forward and reverse rate constants were compared with and without DTT in Table 5.1. Compared with the original nanotube sensors, in the presence of DTT, both the forward and reverse rate constants slightly decreased, yielding very similar equilibrium constants across various concentrations.

Table 5.1 Comparison between H_2O_2 quenching rate constants on SWNT with and without DTT

Collagen-SWNT	$H_2O_2(\mu M)$	k_1 (1/s)	k_{-1} (1/s)	K
	20	0.000957	0.000600	1.59
without DTT	50	0.001239	0.000621	1.99
	100	0.001400	0.000600	2.33
	20	0.000702	0.000440	1.60
with DTT	50	0.000758	0.000430	1.76
	100	0.001100	0.000400	2.75

While intuitive, these experimental results have proven the possibility of utilizing reducing agents on carbon nanotubes as a way of expanding our platform to more sensitive or high throughput measurements. Future work will focus on extending the single molecule sensor array for selective detection to other analytes, for example, nitric oxide, glucose and dopamine. To aid these, we have developed a series of Matlab code that can be used to collect movies in a non-memory-intensive way for an unlimited amount of time with an optional autofocus algorithm embedded (Appendix E).

6. Bibliography

(1)   Iijima, S. Helical Microtubules of Graphitic Carbon *Nature* **1991**, *354*, 56-58.

(2)   Bachilo, S. M.; Strano, M. S.; Kittrell, C.; Hauge, R. H.; Smalley, R. E.; Weisman, R. B. Structure-assigned optical spectra of single-walled carbon nanotubes *Science* **2002**, *298*, 2361-2366.

(3)   Dresselhaus, M. S.; Dresselhaus, G.; Satio, R. *Physics of Carbon nanotubes*, 1995.

(4)   Saito, R.; Dresselhaus, G.; Dresselhaus, M. S. *Physical Properties of Carbon Nanotubes*; Imperial College Press: London, 1998.

(5)   Dresselhaus, M. S.; Dresselhaus, G.; Avouris, P. *Carbon nanotubes: Synthesis, Structure, Properties, and Applications (Springer-Verlag, Heidelberg, Germany, 2001)*, 2001.

(6)   Strano, M. S.; Doorn, S. K.; Haroz, E. H.; Kittrell, C.; Hauge, R. H.; Smalley, R. E. Assignment of (n, m) Raman and optical features of metallic single-walled carbon nanotubes *Nano Letters* **2003**, *3*, 1091-1096.

(7)   Barone, P. W.; Baik, S.; Heller, D. A.; Strano, M. S. Near-infrared optical sensors based on single-walled carbon nanotubes *Nature Materials* **2005**, *4*, 86-96.

(8)   Heller, D. A.; Baik, S.; Eurell, T. E.; Strano, M. S. Single-walled carbon nanotube spectroscopy in live cells: Towards long-term labels and optical sensors *Advanced Materials* **2005**, *17*, 2793-2799.

(9)   Jeng, E. S.; Moll, A. E.; Roy, A. C.; Gastala, J. B.; Strano, M. S. Detection of DNA hybridization using the near-infrared band-gap fluorescence of single-walled carbon nanotubes *Nano Letters* **2006**, *6*, 371-375.

(10)   O'Connell, M. J.; Bachilo, S. M.; Huffman, C. B.; Moore, V. C.; Strano, M. S.; Haroz, E. H.; Rialon, K. L.; Boul, P. J.; Noon, W. H.; Kittrell, C.; Ma, J. P.; Hauge, R. H.; Weisman, R. B.; Smalley, R. E. Band gap fluorescence from individual single-walled carbon nanotubes *Science* **2002**, *297*, 593-596.

(11)   Misewich, J. A.; Martel, R.; Avouris, P.; Tsang, J. C.; Heinze, S.; Tersoff, J. Electrically induced optical emission from a carbon nanotube FET *Science* **2003**, *300*, 783-786.

(12)   Barone, P. W.; Parker, R. S.; Strano, M. S. In vivo fluorescence detection of glucose using a single-walled carbon nanotube optical sensor: Design, fluorophore properties, advantages, and disadvantages *Analytical Chemistry* **2005**, *77*, 7556-7562.

(13)   Barone, P. W.; Strano, M. S. Reversible control of carbon nanotube aggregation for a glucose affinity sensor *Angewandte Chemie-International Edition* **2006**, *45*, 8138-8141.

(14)   Heller, D. A.; Jeng, E. S.; Yeung, T. K.; Martinez, B. M.; Moll, A. E.; Gastala, J. B.; Strano, M. S. Optical detection of DNA conformational polymorphism on single-walled carbon nanotubes *Science* **2006**, *311*, 508-511.

(15)   Choi, J. H.; Strano, M. S. Solvatochromism in single-walled carbon nanotubes *Applied Physics Letters* **2007**, *90*, 223114-223113.

(16)   Strano, M. S.; Moore, V. C.; Miller, M. K.; Allen, M. J.; Haroz, E. H.; Kittrell, C.; Hauge, R. H.; Smalley, R. E. The role of surfactant adsorption during

ultrasonication in the dispersion of single-walled carbon nanotubes *Journal of Nanoscience and Nanotechnology* **2003**, *3*, 81-86.

(17)   Cognet, L.; Tsyboulski, D. A.; Rocha, J. D. R.; Doyle, C. D.; Tour, J. M.; Weisman, R. B. Stepwise quenching of exciton fluorescence in carbon nanotubes by single-molecule reactions *Science* **2007**, *316*, 1465-1468.

(18)   Jin, H.; Heller, D. A.; Kim, J.-H.; Strano, M. S. Stochastic Analysis of Stepwise Fluorescence Quenching Reactions on Single-Walled Carbon Nanotubes: Single Molecule Sensors *Nano Letters* **2008**, *8*, 4299-4304.

(19)   Jin, H.; Jeng, E. S.; Heller, D. A.; Jena, P. V.; Kirmse, R.; Langowski, J.; Strano, M. S. Divalent Ion and Thermally Induced DNA Conformational Polymorphism on Single-walled Carbon Nanotubes *Macromolecules* **2007**, *40*, 6731-6739.

(20)   Jin, H.; Heller, D. A.; Sharma, R.; Strano, M. S. Size-Dependent Cellular Uptake and Expulsion of Single-Walled Carbon Nanotubes: Single Particle Tracking and a Generic Uptake Model for Nanoparticles *ACS Nano* **2009**, *3*, 149-158.

(21)   Zheng, M.; Jagota, A.; Strano, M. S.; Santos, A. P.; Barone, P.; Chou, S. G.; Diner, B. A.; Dresselhaus, M. S.; McLean, R. S.; Onoa, G. B.; Samsonidze, G. G.; Semke, E. D.; Usrey, M.; Walls, D. J. Structure-based carbon nanotube sorting by sequence-dependent DNA assembly *Science* **2003**, *302*, 1545-1548.

(22)   Donaldson, K.; Stone, V.; Tran, C. L.; Kreyling, W.; Borm, P. J. A. Nanotoxicology *Occupational and Environmental Medicine* **2004**, *61*, 727-728.

(23)   Lacerda, L.; Bianco, A.; Prato, M.; Kostarelos, K. Carbon nanotubes as nanomedicines: From toxicology to pharmacology *Advanced Drug Delivery Reviews* **2006**, *58*, 1460-1470.

(24)   Chavanpatil, M. D.; Khdair, A.; Panyam, J. Nanoparticles for cellular drug delivery: Mechanisms and factors influencing delivery *Journal of Nanoscience and Nanotechnology* **2006**, *6*, 2651-2663.

(25)   Chavanpatil, M. D.; Khdair, A.; Panyam, J. Surfactant-polymer nanoparticles: A novel platform for sustained and enhanced cellular delivery of water-soluble molecules *Pharmaceutical Research* **2007**, *24*, 803-810.

(26)   Wieder, M. E.; Hone, D. C.; Cook, M. J.; Handsley, M. M.; Gavrilovic, J.; Russell, D. A. Intracellular photodynamic therapy with photosensitizer-nanoparticle conjugates: cancer therapy using a 'Trojan horse' *Photochemical & Photobiological Sciences* **2006**, *5*, 727-734.

(27)   Chen, W.; Zhang, J. Using nanoparticles to enable simultaneous radiation and photodynamic therapies for cancer treatment *Journal of Nanoscience and Nanotechnology* **2006**, *6*, 1159-1166.

(28)   Kam, N. W. S.; Jessop, T. C.; Wender, P. A.; Dai, H. J. Nanotube molecular transporters: Internalization of carbon nanotube-protein conjugates into mammalian cells *Journal of the American Chemical Society* **2004**, *126*, 6850-6851.

(29)   Pantarotto, D.; Briand, J. P.; Prato, M.; Bianco, A. Translocation of bioactive peptides across cell membranes by carbon nanotubes *Chemical Communications* **2004**, 16-17.

(30)   Pantarotto, D.; Singh, R.; McCarthy, D.; Erhardt, M.; Briand, J. P.; Prato, M.; Kostarelos, K.; Bianco, A. Functionalized carbon nanotubes for plasmid DNA gene delivery *Angewandte Chemie-International Edition* **2004**, *43*, 5242-5246.

119

(31)   Tkachenko, A. G.; Xie, H.; Coleman, D.; Glomm, W.; Ryan, J.; Anderson, M. F.; Franzen, S.; Feldheim, D. L. Multifunctional gold nanoparticle-peptide complexes for nuclear targeting *Journal of the American Chemical Society* **2003**, *125*, 4700-4701.

(32)   Chithrani, B. D.; Chan, W. C. W. Elucidating the Mechanism of Cellular Uptake and Removal of Protein-Coated Gold Nanoparticles of Different Sizes and Shapes *Nano Letters* **2007**.

(33)   Chithrani, B. D.; Ghazani, A. A.; Chan, W. C. W. Determining the size and shape dependence of gold nanoparticle uptake into mammalian cells *Nano Letters* **2006**, *6*, 662-668.

(34)   Kam, N. W. S.; Liu, Z. A.; Dai, H. J. Carbon nanotubes as intracellular transporters for proteins and DNA: An investigation of the uptake mechanism and pathway *Angewandte Chemie-International Edition* **2006**, *45*, 577-581.

(35)   Kostarelos, K.; Lacerda, L.; Pastorin, G.; Wu, W.; Wieckowski, S.; Luangsivilay, J.; Godefroy, S.; Pantarotto, D.; Briand, J. P.; Muller, S.; Prato, M.; Bianco, A. Cellular uptake of functionalized carbon nanotubes is independent of functional group and cell type *Nature Nanotechnology* **2007**, *2*, 108-113.

(36)   Trohalaki, S. Cellular uptake of functionalized carbon nanotubes shown to be energy-dependent *Mrs Bulletin* **2006**, *31*, 82-83.

(37)   Kirchhausen, T. Three ways to make a vesicle *Nature Reviews Molecular Cell Biology* **2000**, *1*, 187-198.

(38)   Mukherjee, S.; Ghosh, R. N.; Maxfield, F. R. Endocytosis *Physiological Reviews* **1997**, *77*, 759-803.

(39)   Bianco, A.; Kostarelos, K.; Prato, M. Applications of carbon nanotubes in drug delivery *Current Opinion in Chemical Biology* **2005**, *9*, 674-679.

(40)   Huff, T. B.; Hansen, M. N.; Zhao, Y.; Cheng, J. X.; Wei, A. Controlling the cellular uptake of gold nanorods *Langmuir* **2007**, *23*, 1596-1599.

(41)   Panyam, J.; Labhasetwar, V. Dynamics of endocytosis and exocytosis of poly(D,L-lactide-co-glycolide) nanoparticles in vascular smooth muscle cells *Pharmaceutical Research* **2003**, *20*, 212-220.

(42)   Mashanov, G. I.; Molloy, J. E. Automatic detection of single fluorophores in live cells *Biophysical Journal* **2007**, *92*, 2199-2211.

(43)   Mashanov, G. I.; Nenasheva, T. A.; Peckham, M.; Molloy, J. E. Cell biochemistry studied by single-molecule imaging *Biochemical Society Transactions* **2006**, *34*, 983-988.

(44)   Jonas, M.; Yao, Y.; So, P. T. C.; Dewey, C. F. Detecting single quantum dot motion with nanometer resolution for applications in cell biology *Ieee Transactions on Nanobioscience* **2006**, *5*, 246-250.

(45)   Berg, H. C. In *Random walks in biology*; expanded ed.; Princeton University Press: N.J., 1993, pp 5-16.

(46)   Jin, S.; Verkman, A. S. Single Particle Tracking of Complex Diffusion in Membranes: Simulation and Detection of Barrier, Raft, and Interaction Phenomena *J. Phys. Chem. B* **2007**, *111*, 3625-3632.

(47)   Hong, Q. A.; Sheetz, M. P.; Elson, E. L. Single-Particle Tracking - Analysis of Diffusion and Flow in 2-Dimensional Systems *Biophysical Journal* **1991**, *60*, 910-921.

(48)　Seisenberger, G.; Ried, M. U.; Endress, T.; Buning, H.; Hallek, M.; Brauchle, C. Real-time single-molecule imaging of the infection pathway of an adeno-associated virus *Science* **2001**, *294*, 1929-1932.

(49)　Saxton, M. J.; Jacobson, K. Single-particle tracking: Applications to membrane dynamics *Annual Review of Biophysics and Biomolecular Structure* **1997**, *26*, 373-399.

(50)　Jin, H.; Heller, D. A.; Strano, M. S. Single-Particle Tracking of Endocytosis and Exocytosis of Single-Walled Carbon Nanotubes in NIH-3T3 Cells *Nano Letters* **2008**, *8*, 1577-1585.

(51)　Tsyboulski, D. A.; Bachilo, S. M.; Weisman, R. B. Versatile visualization of individual single-walled carbon nanotubes with near-infrared fluorescence microscopy *Nano Letters* **2005**, *5*, 975-979.

(52)　Dorschel, B.; Hermsdorf, D.; Pieck, S.; Starke, S.; Thiele, H. Thickness measurements on cell monolayers using CR-39 detectors *Nuclear Instruments & Methods in Physics Research Section B-Beam Interactions with Materials and Atoms* **2002**, *187*, 525-534.

(53)　Shillaber, C. P. In *Photomicrography in Theory and Practice*; John Wiley and Sons: New York, 1944, p 254.

(54)　Sbalzarini, I. F.; Koumoutsakos, P. Feature point tracking and trajectory analysis for video imaging in cell biology *Journal of Structural Biology* **2005**, *151*, 182-195.

(55)　Kusumi, A.; Sako, Y.; Yamamoto, M. Confined Lateral Diffusion of Membrane-Receptors as Studied by Single-Particle Tracking (Nanovid Microscopy) - Effects of Calcium-Induced Differentiation in Cultured Epithelial-Cells *Biophysical Journal* **1993**, *65*, 2021-2040.

(56)　Chisena, E. N.; Wall, R. A.; Macosko, J. C.; Holzwarth, G. Speckled microtubules improve tracking in motor-protein gliding assays *Physical Biology* **2007**, *4*, 10-15.

(57)　Friedman, D. S.; Vale, R. D. Single-molecule analysis of kinesin motility reveals regulation by the cargo-binding tail domain *Nature Cell Biology* **1999**, *1*, 293-297.

(58)　Courty, S.; Luccardini, C.; Bellaiche, Y.; Cappello, G.; Dahan, M. Tracking individual kinesin motors in living cells using single quantum-dot imaging *Nano Letters* **2006**, *6*, 1491-1495.

(59)　*CD-->AG , our analysis cannot directly track the aggregation pathway, however, several observations clearly demonstrate this pathway including n-IR images at later times, Fig. 2e-g, and previous TEM data (7)* .

(60)　Colvin, V.,

(61)　Tzafriri, A. R.; Wu, D.; Edelman, E. R. Analysis of compartmental models of ligand-induced endocytosis *Journal of Theoretical Biology* **2004**, *229*, 127-138.

(62)　Gao, H. J.; Shi, W. D.; Freund, L. B. Mechanics of receptor-mediated endocytosis *Proceedings of the National Academy of Sciences of the United States of America* **2005**, *102*, 9469-9474.

(63)　Freund, L. B.; Lin, Y. The role of binder mobility in spontaneous adhesive contact and implications for cell adhesion *Journal of the Mechanics and Physics of Solids* **2004**, *52*, 2455-2472.

(64)   Decuzzi, P.; Ferrari, M. The role of specific and non-specific interactions in receptor-mediated endocytosis of nanoparticles *Biomaterials* **2007**, *28*, 2915-2922.

(65)   Decuzzi, P.; Ferrari, M. Design maps for nanoparticles targeting the diseased microvasculature *Biomaterials* **2008**, *29*, 377-384.

(66)   Lauffenburger, D. A.; Linderman, J. J. In *Receptors : models for binding, trafficking, and signaling*; Oxford University Press: New York, 1993, pp 30,95.

(67)   Jiang, W.; Kim, B. Y. S.; Rutka, J. T.; Chan, W. C. W. Nanoparticle-mediated cellular response is size-dependent *Nature Nanotechnology* **2008**, *3*, 145-150.

(68)   Becker, M. L.; Fagan, J. A.; Gallant, N. D.; Bauer, B. J.; Bajpai, V.; Hobbie, E. K.; Lacerda, S. H.; Migler, K. B.; Jakupciak, J. P. Length-dependent uptake of DNA-wrapped single-walled carbon nanotubes *Advanced Materials* **2007**, *19*, 939-945.

(69)   Heller, D. A.; Mayrhofer, R. M.; Baik, S.; Grinkova, Y. V.; Usrey, M. L.; Strano, M. S. Concomitant length and diameter separation of single-walled carbon nanotubes *Journal of the American Chemical Society* **2004**, *126*, 14567-14573.

(70)   Zheng, M.; Jagota, A.; Semke, E. D.; Diner, B. A.; McLean, R. S.; Lustig, S. R.; Richardson, R. E.; Tassi, N. G. DNA-assisted dispersion and separation of carbon nanotubes *Nature Materials* **2003**, *2*, 338-342.

(71)   Berg, O. G.; Vonhippel, P. H. Diffusion-Controlled Macromolecular Interactions *Annual Review of Biophysics and Biophysical Chemistry* **1985**, *14*, 131-160.

(72)   Freeman, D. L.; Doll, J. D. The Influence of Diffusion on Surface-Reaction Kinetics *Journal of Chemical Physics* **1983**, *78*, 6002-6009.

(73)   Richter, P. H.; Eigen, M. Diffusion controlled reaction rates in spheroidal geometry : Application to repressor-operator association and membrane bound enzymes *Biophysical Chemistry* **1974**, *2*, 255-263.

(74)   Qian, Z. M.; Li, H.; Sun, H.; Ho, K. Targeted Drug Delivery via the Transferrin Receptor-Mediated Endocytosis Pathway *Pharmacol Rev* **2002**, *54*, 561-587.

(75)   Miller, K.; Shipman, M.; Trowbridge, I. S.; Hopkins, C. R. Transferrin Receptors Promote the Formation of Clathrin Lattices *Cell* **1991**, *65*, 621-632.

(76)   Mashl, R. J.; Bruinsma, R. F. Spontaneous-curvature theory of clathrin-coated membranes *Biophysical Journal* **1998**, *74*, 2862-2875.

(77)   Murray, R. K.; Granner, D. K.; Mayes, P. A.; Rodwell, V. W. *Harper's Biochemistry*; Appleton & Lange: Norwalk CT, 1993.

(78)   Fritz M. Pohl, T. M. J. Salt-induced co-operative conformational change of a synthetic DNA: Equilibrium and kinetic studies with poly(dG-dC) *Journal of Molecular Biology* **1971**, *67*, 375-396.

(79)   Zimmerman, S. B. The Three-dimensional Structure of DNA *Annual Reviews Biochemistry* **1982**, *51*, 395-427.

(80)   Jovin, T. M.; Soumpasis, D. M. The Transition Between B-DNA and Z-DNA *Annual Reviews Biochemistry* **1987**, *38*, 521-560.

(81)   Wang, A. H.-J.; Quigley, G. J.; Kolpak, F. J.; Marel, G. V. D.; Boom, J. H. V.; Rich, A. Left-Handed Double Helical DNA: Variations in the Backbone Conformation *Science* **1981**, *211*, 171-176.

(82)   Reinhard V. Gessner, G. J. Q., Andrew H. J. Wang, Gijs A. Van der Marel, Jacques H. Van Boom, Alexander Rich Structural basis for stabilization of Z-DNA by cobalt hexaammine and magnesium cations *Biochemistry* **1985**, *24*, 237-240.

(83)   Staii, C.; Johnson, A. T. DNA-decorated carbon nanotubes for chemical sensing *Nano Letters* **2005**, *5*, 1774-1778.

(84)   White, H. W.; Vartak, N. B.; Burland, T. G.; Curtis, F. P.; Kusukawa, N. GelStar (R) nucleic acid gel stain: High sensitivity detection in gels *Biotechniques* **1999**, *26*, 984-988.

(85)   Beschetnova, I. A.; Kaluzhny, D. N.; Livshits, M. A.; Shchyolkina, A. K.; Borisova, O. F. Ethidium probing of the parallel double- and four-stranded structures formed by the telomeric DNA sequences dG(GT)(4)G and d(GT)(5) *Journal of Biomolecular Structure & Dynamics* **2003**, *20*, 789-799.

(86)   Shchyolkina, A. K.; Borisova, O. F.; Livshits, M. A.; Klement, R.; Jovin, T. M. The telomeric dG(GT)(4)G sequence can adopt a parallel-stranded double helical conformation *Journal of Biomolecular Structure & Dynamics* **2001**, *18*, 493-504.

(87)   Singer, V. L.; Jones, L. J.; Yue, S. T.; Haugland, R. P. Characterization of PicoGreen reagent and development of a fluorescence-based solution assay for double-stranded DNA quantitation *Analytical Biochemistry* **1997**, *249*, 228-238.

(88)   Cosa, G.; Focsaneanu, K. S.; McLean, J. R. N.; McNamee, J. P.; Scaiano, J. C. Photophysical properties of fluorescent DNA-dyes bound to single- and double-stranded DNA in aqueous buffered solution *Photochemistry and Photobiology* **2001**, *73*, 585-599.

(89)   Kleinman, H. K.; Klebe, R. J.; Martin, G. R. Role of Collagenous Matrices in the Adhesion and Growth of Cells *Journal of Cell Biology* **1981**, *88*, 473-485.

(90)   Merzak, A.; Koochekpour, S.; Pilkington, G. J. Adhesion of Human Glioma Cell-Lines to Fibronectin, Laminin, Vitronectin and Collagen .1. Is Modulated by Gangliosides in-Vitro *Cell Adhesion and Communication* **1995**, *3*, 27-43.

(91)   McKinney, S. A.; Joo, C.; Ha, T. Analysis of single-molecule FRET trajectories using hidden Markov modeling *Biophysical Journal* **2006**, *91*, 1941-1951.

(92)   Joo, C.; McKinney, S. A.; Nakamura, M.; Rasnik, I.; Myong, S.; Ha, T. Real-time observation of RecA filament dynamics with single monomer resolution *Cell* **2006**, *126*, 515-527.

(93)   Brege, J. J.; Gallaway, C.; Barron, A. R. Fluorescence quenching of single-walled carbon nanotubes in SDBS surfactant suspension by metal ions: Quenching efficiency as a function of metal and nanotube identity *Journal of Physical Chemistry C* **2007**, *111*, 17812-17820.

(94)   Song, C. H.; Pehrsson, P. E.; Zhao, W. Recoverable solution reaction of HiPco carbon nanotubes with hydrogen peroxide *Journal of Physical Chemistry B* **2005**, *109*, 21634-21639.

(95)   Linsenmayer, T. F. In *Collagen, in Cell Biology of Extracellular Matrix*; Hay, E. D., Ed.; Plenum Press: NY, 1991, pp 5-37.

(96)   Wang, X. D.; Bank, R. A.; TeKoppele, J. M.; Agrawal, C. M. The role of collagen in determining bone mechanical properties *Journal of Orthopaedic Research* **2001**, *19*, 1021-1026.

(97)   Pari, L.; Venkateswaran, S. Effect of an aqueous extract of Phaseolus vulgaris on the properties of tail tendon collagen of rats with streptozotocin-induced diabetes *Brazilian Journal of Medical and Biological Research* **2003**, *36*, 861-870.

(98)   Choi, J. H.; Chen, K. H.; Strano, M. S. Aptamer-capped nanocrystal quantum dots: A new method for label-free protein detection *Journal of the American Chemical Society* **2006**, *128*, 15584-15585.

(99)   Landes, C.; Braun, M.; Burda, C.; El-Sayed, M. A. Observation of Large Changes in the Band Gap Absorption Energy of Small CdSe Nanoparticles Induced by the Adsorption of a Strong Hole Acceptor *Nano Lett.* **2001**, *1*, 667-670.

(100)   Landes, C.; Burda, C.; Braun, M.; El-Sayed, M. A. Photoluminescence of CdSe Nanoparticles in the Presence of a Hole Acceptor: n-Butylamine *J. Phys. Chem. B* **2001**, *105*, 2981-2986.

(101)   Cowdery-Corvan, J. R.; Whitten, D. G.; McLendon, G. L. Electron transfer reactions at CdS semiconductor cluster interfaces. Adsorption and microenvironment effects on oxidative reactions *Chemical Physics* **1993**, *176*, 377-386.

(102)   Menter, J. M. Temperature dependence of collagen fluorescence *Photochemical & Photobiological Sciences* **2006**, *5*, 403-410.

(103)   Eddy, S. R. What is a hidden Markov model? *Nature Biotechnology* **2004**, *22*, 1315-1316.

(104)   Messina, T. C.; Kim, H. Y.; Giurleo, J. T.; Talaga, D. S. Hidden Markov model analysis of multichromophore photobleaching *Journal of Physical Chemistry B* **2006**, *110*, 16366-16376.

(105)   Talaga, D. S. Markov processes in single molecule fluorescence *Current Opinion in Colloid & Interface Science* **2007**, *12*, 285-296.

(106)   Yang, H.; Luo, G. B.; Karnchanaphanurach, P.; Louie, T. M.; Rech, I.; Cova, S.; Xun, L. Y.; Xie, X. S. Protein conformational dynamics probed by single-molecule electron transfer *Science* **2003**, *302*, 262-266.

(107)   Andrec, M.; Levy, R. M.; Talaga, D. S. Direct determination of kinetic rates from single-molecule photon arrival trajectories using hidden Markov models *Journal of Physical Chemistry A* **2003**, *107*, 7454-7464.

(108)   Schroder, G. F.; Grubmuller, H. Maximum likelihood trajectories from single molecule fluorescence resonance energy transfer experiments *Journal of Chemical Physics* **2003**, *119*, 9920-9924.

(109)   Gillespie, D. T. Exact Stochastic Simulation of Coupled Chemical-Reactions *Journal of Physical Chemistry* **1977**, *81*, 2340-2361.

(110)   Latimer, W. M. *Oxidation Potentials*; Prentice-Hall: New York, 1938.

(111)   Imlay, J. A. Cellular defenses against superoxide and hydrogen peroxide *Annu. Rev. Biochem.* **2008**, *77*, 755-776.

(112)   Veal, E. A.; Day, A. M.; Morgan, B. A. Hydrogen peroxide sensing and signaling *Molecular Cell* **2007**, *26*, 1-14.

(113)   Hong, Y.; Blackman, N. M. K.; Kopp, N. D.; Sen, A.; Velegol, D. Chemotaxis of nonbiological colloidal rods *Phys. Rev. Lett.* **2007**, *99*.

(114)   Miller, E. W.; Tulyanthan, O.; Isacoff, E. Y.; Chang, C. J. Molecular imaging of hydrogen peroxide produced for cell signaling *Nat. Chem. Biol.* **2007**, *3*, 263-267.

(115)   Zhou, M.; Diwu, Z.; Panchuk-Voloshina, N.; Haugland, R. P. A Stable Nonfluorescent Derivative of Resorufin for the Fluorometric Determination of Trace Hydrogen Peroxide: Applications in Detecting the Activity of Phagocyte NADPH Oxidase and Other Oxidases *Analytical Biochemistry* **1997**, *253*, 162-168.

(116) Carpenter, G.; Cohen, S. Epidermal Growth-Factor *Annu. Rev. Biochem.* **1979**, *48*, 193-216.

(117) Yarden, Y.; Sliwkowski, M. X. Untangling the ErbB signalling network *Nat. Rev. Mol. Cell Biol.* **2001**, *2*, 127-137.

(118) Herbst, R. S. Review of epidermal growth factor receptor biology *Int. J. Radiat. Oncol. Biol. Phys.* **2004**, *59*, 21-26.

(119) Lax, I.; Bellot, F.; Howk, R.; Ullrich, A.; Givol, D.; Schlessinger, J. Functional-Analysis of the Ligand-Binding Site of Egf-Receptor Utilizing Chimeric Chicken Human Receptor Molecules *Embo J.* **1989**, *8*, 421-427.

(120) Masui, H.; Castro, L.; Mendelsohn, J. Consumption of Egf by A431 Cells - Evidence for Receptor Recycling *Journal of Cell Biology* **1993**, *120*, 85-93.

(121) Bae, Y. S.; Kang, S. W.; Seo, M. S.; Baines, I. C.; Tekle, E.; Chock, P. B.; Rhee, S. G. Epidermal growth factor (EGF)-induced generation of hydrogen peroxide - Role in EGF receptor-mediated tyrosine phosphorylation *Journal of Biological Chemistry* **1997**, *272*, 217-221.

(122) Stone, J. R.; Yang, S. P. Hydrogen peroxide: A signaling messenger *Antioxid. Redox Signal.* **2006**, *8*, 243-270.

(123) Foote, C. S.; Pryor, W. A., Ed.; Academic: New York, 1976, pp 85-133.

(124) Ziyatdinova, G. K.; Gil'metdinova, D. M.; Budnikov, G. K. Reactions of superoxide anion radical with antioxidants and their use in voltammetry *J. Anal. Chem.* **2005**, *60*, 49-52.

(125) Kim, J.-H.; Heller, D. A.; Jin, H.; Barone, P. W.; Song, C.; Zhang, J.; Trudel, L. J.; Wogan, G. N.; Tannenbaum, S. R.; Strano, M. S. The rational design of nitric oxide selectivity in single-walled carbon nanotube near infrared fluorescence sensors for biological detection *Nature Chemistry* **2009**, submitted.

(126) Heller, D. A.; Jin, H.; Martinez, B. M.; Patel, D.; Miller, B. M.; Yeung, T. K.; Jena, P. V.; Hobartner, C.; Ha, T.; Silverman, S. K.; Strano, M. S. Multimodal optical sensing and analyte specificity using single-walled carbon nanotubes *Nature Nanotechnology* **2009**, *4*, 114-120.

(127) DeYulia, G. J.; Carcamo, J. M.; Borquez-Ojeda, O.; Shelton, C. C.; Golde, D. W. Hydrogen peroxide generated extracellularly by receptor-ligand interaction facilitates cell signaling *Proceedings of the National Academy of Sciences of the United States of America* **2005**, *102*, 5044-5049.

(128) Morazzani, M.; De Carvalho, D. D.; Kovacic, H.; Smida-Rezgui, S.; Briand, C.; Penel, C. Monolayer versus aggregate balance in survival process for EGF-induced apoptosis in A431 carcinoma cells: Implication of ROS-P38 mapk-integrin A2B1 pathway *Int. J. Cancer* **2004**, *110*, 788-799.

(129) Park, H. S.; Lee, S. H.; Park, D.; Lee, J. S.; Ryu, S. H.; Lee, W. J.; Rhee, S. G.; Bae, Y. S. Sequential activation of phosphatidylinositol 3-kinase, beta Pix, Rac1, and Nox1 in growth factor-induced production of H2O2 *Mol. Cell. Biol.* **2004**, *24*, 4384-4394.

(130) Ramey, N. A.; Park, C. Y.; Gehlbach, P. L.; Chuck, R. S. Imaging mitochondria in living corneal endothelial cells using autofluorescence microscopy *Photochem. Photobiol.* **2007**, *83*, 1325-1329.

(131) Welsher, K.; Liu, Z.; Daranciang, D.; Dai, H. Selective probing and imaging of cells with single walled carbon nanotubes as near-infrared fluorescent molecules *Nano Letters* **2008**, *8*, 586-590.

(132) Nieva, J.; Wentworth, P. The antibody-catalyzed water oxidation pathway - a new chemical arm to immune defense? *Trends Biochem.Sci.* **2004**, *29*, 274-278.

(133) Carpenter, G. In *The EGF Receptor Family: Biologic Mechanisms and Role in Cancer*; Academic Press: St. Louis, 2003, pp 33-60.

(134) Harbour, J. R.; Issler, S. L. Involvement of the Azide Radical in the Quenching of Singlet Oxygen by Azide Anion in Water *Journal of the American Chemical Society* **1982**, *104*, 903-905.

(135) Juarez, J. C.; Manuia, M.; Burnett, M. E.; Betancourt, O.; Boivin, B.; Shaw, D. E.; Tonks, N. K.; Mazar, A. P.; Donate, F. Superoxide dismutase 1 (SOD1) is essential for H2O2-mediated oxidation and inactivation of phosphatases in growth factor signaling *Proceedings of the National Academy of Sciences of the United States of America* **2008**, *105*, 7147-7152.

(136) Yang, J. L.; Wang, L. C.; Chang, C. Y.; Liu, T. Y. Singlet oxygen is the major species participating in the induction of DNA strand breakage and 8-hydroxydeoxyguanosine adduct by lead acetate *Environ. Mol. Mutagen.* **1999**, *33*, 194-201.

(137) Fridovich, I. Biology of Oxygen Radicals *Science* **1978**, *201*, 875-880.

(138) Imlay, J. A.; Chin, S. M.; Linn, S. Toxic DNA Damage by Hydrogen-Peroxide through the Fenton Reaction Invivo and Invitro *Science* **1988**, *240*, 640-642.

(139) Halliwell, B.; Aruoma, O. I. DNA Damage by Oxygen-Derived Species - Its Mechanism and Measurement in Mammalian Systems *FEBS Lett.* **1991**, *281*, 9-19.

(140) Khan, A. U.; Kasha, M. Singlet Molecular-Oxygen in the Haber-Weiss Reaction *Proceedings of the National Academy of Sciences of the United States of America* **1994**, *91*, 12365-12367.

(141) Hatz, S.; Lambert, J. D. C.; Ogilby, P. R. Measuring the lifetime of singlet oxygen in a single cell: addressing the issue of cell viability *Photochemical & Photobiological Sciences* **2007**, *6*, 1106-1116.

(142) Hardwick, T. J. The rate constant of the reaction between ferrous ions and hydrogen peroxide in acid solution *Canadian Journal of Chemistry* **1957**, *35*, 428-436.

(143) Wentworth, A. D.; Jones, L. H.; Wentworth, P.; Janda, K. D.; Lerner, R. A. Antibodies have the intrinsic capacity to destroy antigens *Proceedings of the National Academy of Sciences of the United States of America* **2000**, *97*, 10930-10935.

(144) Wentworth, P.; Jones, L. H.; Wentworth, A. D.; Zhu, X. Y.; Larsen, N. A.; Wilson, I. A.; Xu, X.; Goddard, W. A.; Janda, K. D.; Eschenmoser, A.; Lerner, R. A. Antibody catalysis of the oxidation of water *Science* **2001**, *293*, 1806-1811.

(145) Imlay, J. A. Pathways of oxidative damage *Annu. Rev. Microbiol.* **2003**, *57*, 395-418.

(146) Krauss, T. et al, ACS Annual Meeting, Washington, DC, Aug 2009

126

Appendix A: MATLAB Programs

Selected MATLAB functions for gel electrophoresis analysis

The following MATLAB program calculates the pixel row average of gel electrophoresis data.

```
%Enter the function arguments in the following manner:
%wells('input_filename','image_format','output_filename').
%Include the single quotes.
%You could either store the file in the MATLAB work directory and enter the file name directly, or
%have the file elsewhere and use the complete path while calling the "wells" routine.
%image_format = jpg OR jpeg, bmp, tif OR tiff, png
%Example: The command "wells('reaction','jpg')" will plot the row averages against the row number,
i.e.,
%pixel number in the vertical direction.
%The Pixel-Row Average data is sent to an Excel file named "well.xls", in the MATLAB work
directory.
%Save "well.xls" under another name, it will be overwritten during the next run of this program.

function row_avg=wells(input_file,format,output_file)

A=imread(input_file,format);        %converts image into a numerical matrix
rows=length(A(:,1));                %computes # of rows
cols=length(A(1,:));                %computes # of columns
row_avg=[];                         %initialises the row_avg vector

for i=1:rows
    temp=mean(A(i,:));              %computes row-wise means
    row_avg=[row_avg;temp];            %appends the means to the row_avg vector
end

max_intensity=max(row_avg);             %finds the maximum row-averaged intensity
row_avg=max_intensity-row_avg;           %now, the dark regions have higher intensities
pixel=1:rows;
pixel=pixel';
matrix=[pixel row_avg];            %2-column matrix containing the data
xlswrite(matrix,[],[],output_file);

plot(pixel,row_avg,'.');            %plots the row averages for each pixel
xlabel('Pixel');
ylabel('Intensity (greater for dark regions)');

%The following function was downloaded from
http://www.mathworks.com/matlabcentral/files/2855/xlswrite.m
%It creates an Excel spreadsheet from MATLAB.

function xlswrite(m,header,colnames,filename,sheetname);

% Parse inputs
if nargin<2
    header = [];
```

```
end;

if nargin<3
    colnames = {};
end;

if nargin<4 | isempty(filename)
    visible = 1;    % Not saving to a file, so make Excel visible
    filename = '';
else
    visible = 0;    % Saving to a file.  Keep Excel hidden
end;

if nargin < 5 | isempty(sheetname)
    sheetname = 'Sheet1';
end;

[nr,nc] = size(m);
if nc>256
    error('Matrix is too large.  Excel only supports 256 columns');
end;

% Open Excel, add workbook, change active worksheet,
% get/put array, save.
% First, open an Excel Server.
Excel = actxserver('Excel.Application');

% Three cases:
% * Open a new workbook, but don't save (filename is empty)
% * Open a new workbook, save with given file name
% * Open an existing workbook
if isempty(filename)
    % Insert a new workbook.
    op = invoke(Excel.Workbooks, 'Add');

elseif exist(filename,'file')==0
    % The following case if file does not exist (Creating New File)
    op = invoke(Excel.Workbooks,'Add');
    invoke(op, 'SaveAs', [pwd filesep filename]);
    new=1;
else
    % The following case if file does exist (Opening File)
    disp(['Opening Excel File ...(' filename ')']);
    op = invoke(Excel.Workbooks, 'open', [pwd filesep filename]);
    new=0;
end

%If the user does not specify a filename, we'll make Excel visible
%If they do, we'll just save the file and quit Excel without ever making
% it visible
set(Excel, 'Visible', visible);    %You might want to hide this if you autosave the file

% Make the specified sheet active.
```

128

```matlab
try
    Sheets = Excel.ActiveWorkBook.Sheets;
    target_sheet = get(Sheets, 'Item', sheetname);
catch
    % Error if the sheet doesn't exist.  It would be nice to create it, but
    % I'm too lazy.
    % The alternative to try/catch is to call xlsfinfo to see if the sheet exists, but
    % that's really slow.
    error(['Sheet ' sheetname ' does not exist!']);
end;

invoke(target_sheet, 'Activate');

[nr,nc] = size(m);
if nc>256
    error('Matrix is too large.  Excel only supports 256 columns');
end;


%Write header
Activesheet = Excel.Activesheet;
if isempty(header)
    nhr=0;
elseif iscell(header)
    nhr = length(header);       %Number header rows
    for ii=1:nhr
        ActivesheetRange = get(Activesheet,'Range',['A' num2str(ii)],['A' num2str(ii)]);
        set(ActivesheetRange, 'Value', header{ii});
    end;
else
    nhr = 1;                    %Number header rows
    ActivesheetRange = get(Activesheet,'Range','A1','A1');
    set(ActivesheetRange, 'Value', header);
end;


%Add column names

if ~isempty(colnames)
    nhr = nhr + 1;      %One extra column name
    ncolnames = length(colnames);
    for ii=1:ncolnames
        colname = localComputLastCol('A',ii);
        %    cellname = [char(double('A')+ii-1) num2str(nhr+1)];
        cellname = [colname num2str(nhr)];
        ActivesheetRange = get(Activesheet,'Range',cellname,cellname);
        set(ActivesheetRange, 'Value', colnames{ii});
    end;
end;


% Put a MATLAB array into Excel.
FirstRow = nhr+1;           %You can change the first data row here.  I start right after the headers
```

```
LastRow = FirstRow+nr-1;
FirstCol = 'A';      %You can change the first column here
LastCol = localComputLastCol(FirstCol,nc);
ActivesheetRange       =       get(Activesheet,'Range',[FirstCol       num2str(FirstRow)],[LastCol
num2str(LastRow)]);
set(ActivesheetRange, 'Value', m);


% If user specified a filename, save the file and quit Excel

% If user specified a filename, save the file and quit Excel
if ~isempty(filename)
   [pathstr,name,ext] = fileparts(filename);
   if isempty(pathstr)
      pathstr = pwd;
   end;

   invoke(op, 'Save');
   %    invoke(Workbook, 'SaveAs', [pathstr filesep name ext]);
   invoke(Excel, 'Quit');

   [pathstr,name,ext] = fileparts(filename);
   disp(['Excel file ' name '.xls has been created.']);
end;


%Delete the ActiveX object
delete(Excel)



function LastCol = localComputLastCol(FirstCol,nc);
% Comput the name of the last column where we will place data
%Input
%  FirstCol  (string) name of first column
%  nc      total number of columns to write

%Excel's columns are named:
% A B C ... A AA AB AC AD .... BA BB BC ...
FirstColOffset = double(FirstCol) - double('A');    %Offset from column A
if nc<=26-FirstColOffset      %Easy if single letter
   %Just convert to ASCII code, add the number of needed columns, and convert back
   %to a string
   LastCol = char(double(FirstCol)+nc-1);
else
   % Fix for 52 or more columns generously provided by dragon5645995@sina.com.cn
   ng = ceil(nc/26);     %Number of groups (of 26)
   rm = rem(nc,26)+FirstColOffset;      %How many extra in this group beyond A
   if rem(nc,26)==0
      rm=26;
   end
   LastColFirstLetter = char(double('A') + ng-2);
   LastColSecondLetter = char(double('A') + rm-1);
   LastCol = [LastColFirstLetter LastColSecondLetter];
end;
```

Selected MATLAB functions for single-particle tracking

This program is used to classify the trajectories. The input is the trajectory information, in the following format, in *.txt or *.dat files. The first column is the frame number, the second column is the location in the X axis and the third column is the location in the Y axis. The last three columns are the intensity moments.

```
%% Trajectory 1
1 170.869354 125.560600 0.453755 2.949914 202.429977
2 170.384659 125.414284 0.328693 2.675727 77.677956
3 170.457611 125.609802 0.392029 3.074666 278.027130
4 170.373688 125.214737 0.355904 3.037918 246.940598
5 170.061829 125.734886 0.311122 2.641720 49.575218
...
%% Trajectory 2
1 70.869354 15.560600 0.153755 1.949914 10.429977
2 70.384659 15.414284 0.128693 1.675727 17.677956
...
```

The following MATLAB program, SPT, takes in the all the trajectories information and classifies the trajectories.

```
function SPT(deltat,name) % deltat is the time between frames in the unit of second; name is file
name.
datafileID = fopen(name,'r');

vindex = 0;
frameindex = 0;
alpha = 0.0;
tline = 1;
while (tline ~= -1)
   tline = fgetl(datafileID);
   if (tline == -1)
      continue;
   end;
   if ((sum(isletter(tline)) == 0)&&(sum(isspace(tline)==0)))
      frameindex = frameindex + 1;
      A = sscanf(tline,'%d %f %f %f %f %f');
      frame(vindex,frameindex) = A(1);
      y(vindex,frameindex) = A(2);
      x(vindex,frameindex) = A(3);
      zerom(vindex,frameindex) = A(4);
      secondm(vindex,frameindex) = A(5);
      test(vindex,frameindex) = A(6);
   else
      tline = fgetl(datafileID);
      vindex = vindex + 1;
      frameindex = 0;
   end;
end;
fclose(datafileID);
```

```
hold on;

sizeX=size(x);

Nv=sizeX(1)

% Several cell images were taken in between movies, which create the "buffering area" in trajectory
classification. The following is shown as an example in the case where "cell2.jpg" is smaller than
"cell1.jpg". Similar "buffering areas" can be created in other cases as well.
M1=imread('cell1.jpg'); M1=M1';
M2=imread('cell2.jpg');M2=M2';

for vindex=1:Nv
    types(vindex)=0;
end

count=0;%total # of trajectories in the overlapping area (nIR and visible)
count1=0;%inside the cell
count2=0;%outside the cell
count3=0;%endocytosis
count4=0;%exotytosis
count5=0;%absorption
count6=0;%surface to inside
count7=0;%desorption
count8=0;%surface to outside
count9=0;%on surface
count10=0;%others

for vindex=1:Nv
    %disp(['vindex: ',vindex);
    Num=sizeX(2);
    if (x(vindex,Num) <= 0.)
        for n=1:Num
            if (x(vindex,n) <= 0.)
                break;
            end
        end
        Num=n-1;
    end

    flag=0;
    for n=1:Num
    %convert the dimension in CCD camera into nIR camera
        if  ((1174*x(vindex,n)/256+174  >  1388)  ||  (1467*y(vindex,n)/320-259  >  1040)  ||
(1467*y(vindex,n)/320-259 < 0))
            flag = 1;
            break;
        end
    end
    if (flag == 1)
        continue;
    end
```

132

```
flag=0;
for n=1:Num
    if (M2(round(1174*x(vindex,n)/256+174),round(1467*y(vindex,n)/320-259))== 255)
        flag=1;
        break;
    end
end
if (flag == 0)
    count1=count1+1;
    types(vindex)=1; % in
end
flag=0;
for n=1:Num
    if (M1(round(1174*x(vindex,n)/256+174),round(1467*y(vindex,n)/320-259))~= 255)
        flag=1;
        break;
    end
end
if (flag == 0)
    count2=count2+1;
    types(vindex)=2; % out
end
flag=0;
for n=1:Num
    if   ((M1(round(1174*x(vindex,n)/256+174),round(1467*y(vindex,n)/320-259))==   255)   ||
(M2(round(1174*x(vindex,n)/256+174),round(1467*y(vindex,n)/320-259))~= 255))
        flag = 1;
        break;
    end
end
if (flag == 0)
    count9=count9+1;
    types(vindex)=9; % on surface
end


if (types(vindex) == 0)
    if   ((M1(round(1174*x(vindex,1)/256+174),round(1467*y(vindex,1)/320-259))==   255)   &&
(M2(round(1174*x(vindex,Num)/256+174),round(1467*y(vindex,Num)/320-259))~= 255))
        count3=count3+1;
        types(vindex)=3; %endocytosis
    elseif ((M2(round(1174*x(vindex,1)/256+174),round(1467*y(vindex,1)/320-259))~= 255) &&
(M1(round(1174*x(vindex,Num)/256+174),round(1467*y(vindex,Num)/320-259))== 255))
        count4=count4+1;
        types(vindex)=4; %exocytosis
    elseif ((M1(round(1174*x(vindex,1)/256+174),round(1467*y(vindex,1)/320-259))== 255) &&
(M1(round(1174*x(vindex,Num)/256+174),round(1467*y(vindex,Num)/320-259))~=   255)   &&
(M2(round(1174*x(vindex,Num)/256+174),round(1467*y(vindex,Num)/320-259))== 255))
        count5=count5+1;
        types(vindex)=5; % absorption
    elseif ((M1(round(1174*x(vindex,1)/256+174),round(1467*y(vindex,1)/320-259))~= 255) &&
(M2(round(1174*x(vindex,1)/256+174),round(1467*y(vindex,1)/320-259))==      255)      &&
(M2(round(1174*x(vindex,Num)/256+174),round(1467*y(vindex,Num)/320-259))~= 255))
```

```
                count6=count6+1;
                types(vindex)=6; % surface to inside
            elseif    ((M2(round(1174*x(vindex,Num)/256+174),round(1467*y(vindex,Num)/320-259))==
255) && (M1(round(1174*x(vindex,Num)/256+174),round(1467*y(vindex,Num)/320-259))~= 255)
&& (M2(round(1174*x(vindex,1)/256+174),round(1467*y(vindex,1)/320-259))~= 255))
                count7=count7+1;
                types(vindex)=7; % inside to surface
            elseif    ((M1(round(1174*x(vindex,Num)/256+174),round(1467*y(vindex,Num)/320-259))==
255) && (M2(round(1174*x(vindex,1)/256+174),round(1467*y(vindex,1)/320-259))== 255) &&
(M1(round(1174*x(vindex,1)/256+174),round(1467*y(vindex,1)/320-259))~= 255))
                count8=count8+1;
                types(vindex)=8; % desorption
            else
                count10=count10+1;
                types(vindex)=10; % others
            end
        end

        for n=1:Num-2
            indx(n)=n;
            msdXY(vindex,n)=0.;
            for j=1:Num-1-n
                msdXY(vindex,n)=msdXY(vindex,n)+((x(vindex,j+n)-x(vindex,j))^2+(y(vindex,j+n)-
y(vindex,j))^2);
            end
            msdXY(vindex,n)=msdXY(vindex,n)/(Num-1-n);
        end

        figure(types(vindex))
        plot(indx(1:Num-2)*deltat,0.189*msdXY(vindex,1:Num-
2),'*');xlabel('Time(s)');ylabel('MSD(um^2)');hold on;
        count=count+1;


end

count
count1
count2
count3
count4
count5
count6
count7
count8
count9
count10
```

The following program calculates the **diffusion coefficient**.

```
function [expcoeff, f_expcoeff] = Diffusion(deltat,name)
datafileID = fopen(name,'r');
%again, read file first
vindex = 0;
frameindex = 0;
alpha = 0.0;
tline = 1;
while (tline ~= -1)
    tline = fgetl(datafileID);
    if (tline == -1)
        continue;
    end;
    if ((sum(isletter(tline)) == 0)&&(sum(isspace(tline)==0)))
        frameindex = frameindex + 1;
        A = sscanf(tline,'%d %f %f %f %f %f');
        frame(vindex,frameindex) = A(1);
        y(vindex,frameindex) = A(2);
        x(vindex,frameindex) = A(3);
        zerom(vindex,frameindex) = A(4);
        secondm(vindex,frameindex) = A(5);
        test(vindex,frameindex) = A(6);
    else
        tline = fgetl(datafileID);
        vindex = vindex + 1;
        frameindex = 0;
    end;
end;
fclose(datafileID);
hold on;

sizeX=size(x);
numparticles = sizeX(1);

%////////////////////////////////////////////////////////////
%Calculate mean squared distances over time
for particle = 1:1:numparticles
    disp = sizeX(2);
    if (x(particle,disp) <= 0.)
        for n = 1:1:disp
            if (x(particle,n) <= 0.)
                break;
            end
        end
        disp = n-1;
    end
    for i = 1:1:disp-1
        newMSD = calculateMSD(x(particle,i), x(particle,i+1), y(particle,i), y(particle,i+1));
        if i == 1
            MSD(particle, i) = newMSD;
        else
            MSD(particle, i) = MSD(particle, i-1) + newMSD;
```

```matlab
        end
    end
end

[MSDrows, MSDcolumns] = size(MSD);

for i = 1:1:(MSDcolumns+1)
    time(i) = (i-1)*deltat;
end

%////////////////////////////////////////////////////////////
%Perform linear regression on MSD plot
for particle = 1:1:MSDrows
    MSD_nozero(particle, 1) = 0;
    if (MSD(particle,MSDcolumns) <= 0.)
        for n = 1:1:MSDcolumns
            if (MSD(particle,n) <= 0.)
                break;
            end
        end
        disp = n-1;
    else
        disp = MSDcolumns;
    end
    time_nozero(particle, 1:disp+1) = time(1:disp+1);
    MSD_nozero (particle, 2:disp+1) = MSD(particle, 1:disp);
    stats = regstats(MSD_nozero(particle, :), time_nozero(particle,:));
    statssummary(particle,1) = stats.beta(2,1);
    statssummary(particle,2) = stats.beta(1,1);
    statssummary(particle,3) = stats.rsquare;
    clear stats;
end

%////////////////////////////////////////////////////////////
%Filter rejected data if slope is less than 20, if r^2 is less than .9, and
%if there are only 2 points in the line (r^2 = 1)

m = 1;
for particle = 1:1:MSDrows
    if statssummary(particle,1) > 20 && statssummary(particle,3) > 0.95 && statssummary(particle,3)
< 1.
        filteredMSD(m,:) = MSD_nozero(particle,:);
        filteredtime(m,:) = time_nozero(particle, :);
        filteredstatssummary(m,1) = statssummary(particle, 1);
        filteredstatssummary(m,2) = statssummary(particle, 2);
        filteredstatssummary(m,3) = statssummary(particle, 3);
        m = m+1;
    end
end

%////////////////////////////////////////////////////////////
%Calculate diffusion coefficient from slopes and plot
```

```matlab
D_coeff(:,1) = 63/100*0.18*filteredstatssummary(:,1)/4;    %convert pixel to microns if using 100x
objective
D_coeff = D_coeff';

increment = (max(D_coeff) - min(D_coeff))/60;
for i = 1:1:61
    bins(i) = min(D_coeff) + (i-1)*increment;
end

frequency = hist(D_coeff,bins);
f_expcoeff = frequency/(sum(frequency));
expcoeff = bins;

%bar(expcoeff, f_expcoeff);

return

%//////////////////////////////////////////////////////////
%       CALCULATE MSD
%//////////////////////////////////////////////////////////

%Calculates mean squared displacement for two x and y coordinates
function [msdXY] = calculateMSD(x1,x2,y1,y2)
msdXY = (x1 - x2)^2 + (y1 - y2)^2;
return
%//////////////////////////////////////////////////////////
```

Selected MATLAB functions for converting transition probability between states to transition probability between single sites

    1) 3 states

```
function calculate_no_3states
clear
clc
% calculate rate constants given transition probability matrix returned from HAMMY.
% INPUT:   tp_HMM:    transition probability matrix;
%          method:    method for optimization
%          P0:        initial guess for P.

% OUTPUT:  P1, P2:    single site transition probability;
%          rf, rr:    forward and reverse rate constants.
tp_HMM = [0.00136465
0.0020517
0.00168942
0.00260361
];

% sequence 1>2, 2>1 ... 6>7,7>6
method = 0;
P0 = [0.1, 0.0001059]' ;

if method == 1
%   options = [];
    options = optimset('TolFun',10^-12,'TolX',10^-12);
    [P,fval] = fminunc(@(P) tp_expression(P,tp_HMM,method),P0,options)
else
    options = [];
%   options = optimset('TolFun',10^-8,'TolX',10^-10);
    [P,resnorm,residual,exitflag] = lsqnonlin(@(P) tp_expression(P,tp_HMM,method),P0,[],[],options)
end

rf = 2*log(1/(1-P(1)))
rr = 2*log(1/(1-P(2)))

end

function F = tp_expression(P,tp_HMM,method)

F_model = [
2*P(2)*(1-P(2)); % 1->2
2*P(1)*(1-P(2)); % 2->1
2*P(2)*(1-P(1)); % 2->3
2*P(1)*(1-P(1)); % 3->2
];
if method == 1
    F = sum(((F_model- tp_HMM)./tp_HMM).^2);
else
    F = (F_model- tp_HMM)./tp_HMM ;
end
end
```

2) 4 states

```
function calculate_no_4states
clear
clc
% calculate rate constants given transition probability matrix returned from HAMMY.
% INPUT:   tp_HMM:    transition probability matrix;
%         method:    method for optimization
%         P0:        initial guess for P.

% OUTPUT:  P1, P2:    single site transition probability;
%         rf, rr:    forward and reverse rate constants.
tp_HMM = [0.00136465
0.0020517
0.00168942
0.00260361
0.0171285
0.0125329];

% sequence 1>2, 2>1 ... 6>7,7>6
method = 0;
P0 = [0.1, 0.0001059]' ;

if method == 1
%   options = [];
    options = optimset('TolFun',10^-12,'TolX',10^-12);
    [P,fval] = fminunc(@(P) tp_expression(P,tp_HMM,method),P0,options)
else
    options = [];
%   options = optimset('TolFun',10^-8,'TolX',10^-10);
    [P,resnorm,residual,exitflag] = lsqnonlin(@(P) tp_expression(P,tp_HMM,method),P0,[],[],options)
end

rf = 2*log(1/(1-P(1)))
rr = 2*log(1/(1-P(2)))

end

function F = tp_expression(P,tp_HMM,method)

F_model = [
3*P(2)*(1-P(2))^2; % 1->2
3*P(1)*(1-P(2))^2; % 2->1
3*(2*P(2)*(1-P(2))*(1-P(1))+P(1)*P(2)^2); % 2->3
3*(2*P(1)*(1-P(2))*(1-P(1))+P(2)*P(1)^2); % 3->2
3*P(2)*(1-P(1))^2; % 3->4
3*P(1)*(1-P(1))^2; % 4->3
];
if method == 1
    F = sum(((F_model- tp_HMM)./tp_HMM).^2);
else
    F = (F_model- tp_HMM)./tp_HMM ;
end
end
```

139

3) 5 states

```
function calculate_no_5states
clear
clc

% calculate rate constants given transition probability matrix returned from HAMMY.
% INPUT:   tp_HMM:    transition probability matrix;
%          method:    method for optimization
%          P0:        initial guess for P.

% OUTPUT:  P1, P2:    single site transition probability;
%          rf, rr:    forward and reverse rate constants.

tp_HMM = [0.00136465
0.0020517
0.00168942
0.00260361
0.0171285
0.0125329
0.118973
0.156799
];

% sequence 1>2, 2>1 ... 6>7,7>6
method = 0;
P0 = [0.1, 0.0001059]' ;

if method == 1
%   options = [];
    options = optimset('TolFun',10^-12,'TolX',10^-12);
    [P,fval] = fminunc(@(P) tp_expression(P,tp_HMM,method),P0,options)
else
    options = [];
%   options = optimset('TolFun',10^-8,'TolX',10^-10);
    [P,resnorm,residual,exitflag] = lsqnonlin(@(P) tp_expression(P,tp_HMM,method),P0,[],[],options)
end

rf = 2*log(1/(1-P(1)))
rr = 2*log(1/(1-P(2)))

end

function F = tp_expression(P,tp_HMM,method)

F_model = [
4*P(2)*(1-P(2))^3; % 1->2
4*P(1)*(1-P(2))^3; % 2->1
12*(P(2)*(1-P(1))*(1-P(2))^2+P(1)*P(2)^2*(1-P(2))); % 2->3
12*(P(1)*(1-P(1))*(1-P(2))^2+P(2)*P(1)^2*(1-P(2))); % 3->2
12*(P(2)*(1-P(2))*(1-P(1))^2+P(1)*P(2)^2*(1-P(1))); % 3->4
12*(P(1)*(1-P(2))*(1-P(1))^2+P(2)*P(1)^2*(1-P(1))); % 4->3
4*P(2)*(1-P(1))^3; % 4->5
```

```
4*P(1)*(1-P(1))^3; % 5->4
];
if method == 1
    F = sum(((F_model- tp_HMM)./tp_HMM).^2);
else
    F = (F_model- tp_HMM)./tp_HMM ;
end
end
```

4) 6 states

```
function calculate_no_6states
clear
clc

% calculate rate constants given transition probability matrix returned from HAMMY.
% INPUT:   tp_HMM:    transition probability matrix;
%          method:    method for optimization
%          P0:        initial guess for P.

% OUTPUT:  P1, P2:    single site transition probability;
%          rf, rr:    forward and reverse rate constants.

tp_HMM = [0.00136465
0.0020517
0.00168942
0.00260361
0.0171285
0.0125329
0.118973
0.156799
0.053211
0.122634
];

% sequence 1>2, 2>1 ... 6>7,7>6
method = 0;
P0 = [0.1, 0.0001059]' ;

if method == 1
%   options = [];
    options = optimset('TolFun',10^-12,'TolX',10^-12);
    [P,fval] = fminunc(@(P) tp_expression(P,tp_HMM,method),P0,options)
else
    options = [];
%   options = optimset('TolFun',10^-8,'TolX',10^-10);
    [P,resnorm,residual,exitflag] = lsqnonlin(@(P) tp_expression(P,tp_HMM,method),P0,[],[],options)
end

rf = 2*log(1/(1-P(1)))
rr = 2*log(1/(1-P(2)))

end

function F = tp_expression(P,tp_HMM,method)

F_model = [
5*P(2)*(1-P(1))^4;  % 1->2
5*P(1)*(1-P(2))^4;  % 2->1
5*(4*P(2)*(1-P(1))*(1-P(2))^3;   % 2->3
5*(4*P(2)*(1-P(1))*(1-P(2))^3+6*P(1)*P(2)^2*(1-P(2))^2); % 3->2
10*(2*P(1)*(1-P(1))*(1-P(2))^3+3*P(1)^2*P(2)^2*(1-P(2)));%3->4
```

142

```
10*(3*P(1)*(1-P(2))^2*(1-P(1))^2+6*P(1)^2*P(2)*(1-P(1))*(1-P(2))+P(1)^3*P(2)^2)); %4->3
10*(2*P(2)*(1-P(2))*(1-P(1))^3+3*P(1)^2*P(2)^2*(1-P(1))); % 4->5
5*(4*P(1)*(1-P(2))*(1-P(1))^3+6*P(1)^2*P(2)*(1-P(1))^2); %5->4
5*P(2)*(1-P(1))^4; % 5->6
5*P(1)*(1-P(1))^4; % 6->5
];
if method == 1
   F = sum(((F_model- tp_HMM)./tp_HMM).^2);
else
   F = (F_model- tp_HMM)./tp_HMM ;
end
end
```

5) 7 states

```
function calculate_no_7states
clear
clc

% calculate rate constants given transition probability matrix returned from HAMMY.
% INPUT:   tp_HMM:     transition probability matrix;
%          method:    method for optimization
%          P0:        initial guess for P.

% OUTPUT:  P1, P2:    single site transition probability;
%          rf, rr:    forward and reverse rate constants.

tp_HMM = [0.00136465
0.0020517
0.00168942
0.00260361
0.0171285
0.0125329
0.118973
0.156799
0.053211
0.122634
0.0592395
0.129169
];

% sequence 1>2, 2>1 ... 6>7,7>6
method = 0;
P0 = [0.1, 0.0001059]' ;

if method == 1
%   options = [];
    options = optimset('TolFun',10^-12,'TolX',10^-12);
    [P,fval] = fminunc(@(P) tp_expression(P,tp_HMM,method),P0,options)
else
    options = [];
%   options = optimset('TolFun',10^-8,'TolX',10^-10);
    [P,resnorm,residual,exitflag] = lsqnonlin(@(P) tp_expression(P,tp_HMM,method),P0,[],[],options)
end

rf = 2*log(1/(1-P(1)))
rr = 2*log(1/(1-P(2)))

end

function F = tp_expression(P,tp_HMM,method)

F_model = [
6*P(2)*(1-P(2))^5;  % 1->2
6*P(1)*(1-P(2))^5;  % 2->1
6*(5*P(2)*(1-P(1))*(1-P(2))^4+10*P(1)*P(2)^2*(1-P(2))^3);  % 2->3
```

144

```
15*(2*P(1)*(1-P(1))*(1-P(2))^4+4*P(2)^2*P(1)^2*(1-P(2))^3);  % 3->2
15*(4*P(2)*(1-P(2))^3*(1-P(1))^2+12*P(1)*P(2)^2*(1-P(2))^2*(1-P(1))+4*P(1)^2*P(2)^3*(1-
P(2)));%3->4
20*(3*P(1)*(1-P(2))^3*(1-P(1))^2+9*P(1)^2*P(2)*(1-P(1))*(1-P(2))^2+3*P(1)^3*P(2)^2*(1-
P(2))); %4->3
20*(3*P(2)*(1-P(2))^2*(1-P(1))^3+9*P(1)*P(2)^2*(1-P(1))^2*(1-P(2))+3*P(1)^2*P(2)^3*(1-
P(1))); % 4->5
15*(4*P(1)*(1-P(2))^2*(1-P(1))^3+12*P(1)^2*P(2)*(1-P(1))^2*(1-P(2))+4*P(1)^3*P(2)^2*(1-
P(1))); %5->4
15*(2*(1-P(2))*P(2)*(1-P(1))^4+4*P(1)*P(2)^2*(1-P(1))^3)); % 5->6
6*(5*P(1)*(1-P(2))*(1-P(1))^4+10*P(2)*P(1)^2*(1-P(1))^3)); % 6->5
6*P(2)*(1-P(1))^5;  % 6->7
6*P(1)*(1-P(1))^5;  % 7->6 ;
];
if method == 1
    F = sum(((F_model- tp_HMM)./tp_HMM).^2);
else
    F = (F_model- tp_HMM)./tp_HMM ;
end
end
```

145

6) 8 states

```
function calculate_no_8states
clear
clc

% calculate rate constants given transition probability matrix returned from HAMMY.
% INPUT:   tp_HMM:    transition probability matrix;
%          method:    method for optimization
%          P0:        initial guess for P.

% OUTPUT:  P1, P2:    single site transition probability;
%          rf, rr:    forward and reverse rate constants.

tp_HMM = [
0.00590224
0.00386798
0.00436123
0.00650007
0.00889043
0.00510106
0.00945755
0.00555765
0.00865254
0.00829086
0.007129
0.0105921
0.0100182
0.0167405
];

% sequence 1>2, 2>1 ... 6>7,7>6
method = 0;
P0 = [0.0001, 0.0001059]' ;

if method == 1
%   options = [];
    options = optimset('TolFun',10^-12,'TolX',10^-12);
    [P,fval] = fminunc(@(P) tp_expression(P,tp_HMM,method),P0,options)
else
    options = [];
%   options = optimset('TolFun',10^-8,'TolX',10^-10);
    [P,resnorm,residual,exitflag] = lsqnonlin(@(P) tp_expression(P,tp_HMM,method),P0,[],[],options)
end

rf = 2*log(1/(1-P(1)))/0.2
rr = 2*log(1/(1-P(2)))/0.2
K = rf/rr

end

function F = tp_expression(P,tp_HMM,method)
P1 = P(1);
P2 = P(2);
```

146

```matlab
F_model = [

7*P2*(1-P2)^6; % 1->2
7*P1*(1-P2)^6; % 2->1
7*(6*(1-P2)^5*P2*(1-P1)+P1*15*(1-P2)^4*P2^2) % 2->3
21*(2*P1*(1-P1)*(1-P2)^5+P1^2*10*P2^2*(1-P1)^3); % 3->2
21*((1-P1)^2*5*P2*(1-P2)^4+2*P1*(1-P1)*10*P2^2*(1-P2)^3+P1^2*10*P2^3*(1-P2)^2); % 3->4
35*(3*P1*(1-P1)^2*(1-P2)^4 + 3*P1^2*(1-P1)*4*P2*(1-P2)^3+P1^3*P2^2*(1-P2)^2); % 4->3
35*(4*(1-P1)^3*P2*(1-P2)^3+3*P1*(1-P1)^2*6*P2^2*(1-P2)^2+3*P1^2*(1-P1)*4*P2^3*(1-P2)+P1^3*P2^4); % 4->5

35*(4*(1-P2)^3*P1*(1-P1)^3+3*P2*(1-P2)^2*6*P1^2*(1-P1)^2+3*P2^2*(1-P2)*4*P1^3*(1-P1)+P2^3*P1^4); % 5->4
35*(3*P2*(1-P2)^2*(1-P1)^4 + 3*P2^2*(1-P2)*4*P1*(1-P1)^3+P2^3*P1^2*(1-P1)^2); % 5->6
21*((1-P2)^2*5*P1*(1-P1)^4+2*P2*(1-P2)*10*P1^2*(1-P1)^3+P2^2*10*P1^3*(1-P1)^2); % 6->5
21*(2*P2*(1-P2)*(1-P1)^5+P2^2*10*P1^2*(1-P1)^3); % 6->7
7*(6*(1-P1)^5*P1*(1-P2)+P2*15*(1-P1)^4*P1^2) % 7->6
7*P2*(1-P1)^6; % 7->8
7*P1*(1-P1)^6; % 8->7
 ];

if method == 1
   F = sum(((F_model- tp_HMM)./tp_HMM).^2);
else
   F = (F_model- tp_HMM)./tp_HMM ;
end
end
```

7) 9 states

```
function calculate_no_9states
clear
clc

% calculate rate constants given transition probability matrix returned from HMMY.
% INPUT:   tp_HMM:    transition probability matrix;
%          method:    method for optimization
%          P0:        initial guess for P.

% OUTPUT:  P1, P2:    single site transition probability;
%          rf, rr:    forward and reverse rate constants.

tp_HMM = [0.000658696
0.0191718
0.00499752
0.0158467
0.0665418
0.0816958
0.0591273
0.139851
0.367879
0.18683
0.201322
0.181486
0.118935
0.0592493
0.0913617
0.0552289
];

% sequence 1>2, 2>1 ... 6>7,7>6
method = 0;
P0 = [0.1, 0.0001059]' ;

if method == 1
%   options = [];
    options = optimset('TolFun',10^-12,'TolX',10^-12);
    [P,fval] = fminunc(@(P) tp_expression(P,tp_HMM,method),P0,options)
else
    options = [];
%   options = optimset('TolFun',10^-8,'TolX',10^-10);
    [P,resnorm,residual,exitflag] = lsqnonlin(@(P) tp_expression(P,tp_HMM,method),P0,[],[],options)
end

rf = 2*log(1/(1-P(1)))/0.2
rr = 2*log(1/(1-P(2)))/0.2
K = rf/rr

end
```

```
function F = tp_expression(P,tp_HMM,method)
P1 = P(1);
P2 = P(2);

F_model = [
8*P2*(1-P2)^7;  % 1->2
8*P1*(1-P2)^7;  % 2->1
8*(7*(1-P1)*(1-P2)^6*P2+21*P1*P2^2*(1-P2)^5);  % 2->3
28*(2*P1*(1-P1)*(1-P2)^6+6*P1^2*P2*(1-P2)^5);  % 3->2
28*(6*(1-P1)^2*(1-P2)^5*P2+30*P1*(1-P1)*P2^2*(1-P2)^4+20*P1^2*P2^3*(1-P2)^3); % 3->4
56*(3*P1*(1-P1)^2*(1-P2)^5+3*P1^2*(1-P1)*5*P2*(1-P2)^4+P1^3*10*P2^2*(1-P2)^3);  % 4->3
56*(5*(1-P1)^3*P2*(1-P2)^4+3*P1*(1-P1)^2*10*(1-P2)^3*P2^2+3*P1^2*(1-P1)*10*P2^3*(1-
P2)^2+P1^3*5*P2^4*(1-P2));  % 4->5
70*(4*P1*(1-P1)^3*(1-P2)^4+6*P1^2*(1-P1)^2*4*P2*(1-P2)^3+4*P1^3*(1-P1)*6*P2^2*(1-
P2)^2+P1^4*4*P2^3*(1-P2));  % 5->4
70*(4*P2*(1-P2)^3*(1-P1)^4+6*P2^2*(1-P2)^2*4*P1*(1-P1)^3+4*P2^3*(1-P2)*6*P1^2*(1-
P1)^2+P2^4*4*P1^3*(1-P1));  % 5->6
56*(5*(1-P2)^3*P1*(1-P1)^4+3*P2*(1-P2)^2*10*(1-P1)^3*P1^2+3*P2^2*(1-P2)*10*P1^3*(1-
P1)^2+P2^3*5*P1^4*(1-P1));  % 6->5
56*(3*P2*(1-P2)^2*(1-P1)^5+3*P2^2*(1-P2)*5*P1*(1-P1)^4+P2^3*10*P1^2*(1-P1)^3);  % 6->7
28*(6*(1-P2)^2*(1-P1)^5*P1+30*P2*(1-P2)*P1^2*(1-P1)^4+20*P2^2*P1^3*(1-P1)^3);  % 7->6
28*(2*P2*(1-P2)*(1-P1)^6+6*P2^2*P1*(1-P1)^5);  % 7->8
8*(7*(1-P2)*(1-P1)^6*P1+21*P2*P1^2*(1-P1)^5);  % 8->7
8*P2*(1-P1)^7;  % 8->9
8*P1*(1-P1)^7;  % 9->8
 ];

if method == 1
   F = sum(((F_model- tp_HMM)./tp_HMM).^2);
else
   F = (F_model- tp_HMM)./tp_HMM ;
end

end
```

149

MATLAB simulation of the PL trace of a nanotube with certain number of quenchable empty sites

```matlab
function [Null] = singlesite3_Hong(Null)
% This is a simple example
% A <-> B with kf (the quenching rate constant, k1) and kr (the reverse rate constant, k-1)

%Set initial population
% populations of species x1 x2 x3 ... xn
h2o2 = 1;
x = [10 10 10 0 0 0];
BT = 3;  %total number of empty sites
noise = 0.0;
datapointsperevent = 10;

%rate constant info
c1 = 3;
c2 = 2;
c = [c1 c2];

%Set simulation parameters
n = 0;
t = 0;
nmax = 800;

while n < nmax;
n = n + 1;

%Rate expressions
% x1 to x3 = unquenched nanotube site
% x4 to x6 = quenched nanotube site
% a1 = c1 X1
% a2 = c2 X2
anu = zeros(2*BT,1);
for j = 1:BT
    anu(j) = c(1)*h2o2*x(j);
    anu(j+BT) = c(2)*x(j+BT);
end;
ao = sum(anu);

%Two random numbers
r1 = rand(1);
r2 = rand(1);

tau = 1/ao*log(1/r1);
t = t + tau;
time(n) = t;

%Choose which reaction has occurred
cumanu(1) = anu(1);
for (i = 2:length(anu))
    cumanu(i) = cumanu(i-1) + anu(i);
end
```

```matlab
mu = length(cumanu(cumanu<ao*r2))+1;

%Update x given the type of reaction (x(1) = constant)

if mu <= BT
    x(mu) = 0;
    x(mu+BT) = 1;
end;

if mu > BT
    x(mu - BT) = 1;
    x(mu) = 0;
end;

xtotal1(n) = sum(x(1:BT));
xtotal2(n) = sum(x(BT+1:2*BT));

%Ends the simulation
end;
maxtime = time(nmax)
frames = time(nmax)/nmax/datapointsperevent

%Create a new array that shows steps
tprime = zeros(2*length(xtotal1),1);
timeprime = zeros(2*length(xtotal1),1);
for i = 1:length(xtotal1)
    timeprime(2*i) = time(i);
    timeprime(2*i-1) = time(i);
    tprime(2*i) = xtotal2(i);
    if (i > 1) tprime(2*i-1) = xtotal2(i-1); end;
end;


%This simulates the signal with noise
exptime = 1:time(nmax)/nmax/datapointsperevent:time(nmax);
expsignal = zeros(length(exptime),1);
stepcounter = 1;

for i = 1:length(exptime)
    if (exptime(i) < time(stepcounter) && stepcounter < length(xtotal2))
        expsignal(i) = xtotal2(stepcounter);
    else
        if (stepcounter < length(xtotal2))  stepcounter = stepcounter + 1; end;
        expsignal(i) = xtotal2(stepcounter);
    end;
end;

%This adds noise
expsignalnoise = expsignal + (rand(length(expsignal),1) - 0.5)*noise;

donorsig = (expsignal + (rand(length(expsignal),1) - 0.5)*noise)*100;
acceptorsig = (BT-expsignal + (rand(length(expsignal),1) - 0.5)*noise )*100;
```

```
dlmwrite('newmod1.dat', [exptime' donorsig acceptorsig],'delimiter', ' ');

%plot(exptime,expsignalnoise,exptime,expsignal,'--
rs','LineWidth',2,'MarkerEdgeColor','k','MarkerFaceColor','g','MarkerSize',2)

%    csvwrite('test.txt',[timeprime BT-tprime]);

plot(timeprime,BT-tprime,'--
rs','LineWidth',2,'MarkerEdgeColor','k','MarkerFaceColor','g','MarkerSize',2)

%tprime(floor(length(tprime)*4/5):length(tprime));

%result(k)= mean(BT-tprime(floor(length(tprime)*3/5):length(tprime)));

end


%plot(log(cvector), result,'o')
```

Selected   MATLAB   functions   for   fluorescence   trace   analysis

The following MATLAB program, Analyzer2, converts a data sheet containing the PL trace of n ROIs into n separate "*dat" file, with the location of each ROI documented as the name of the file. Smaller time windows can be zoomed on by change the parameter "inv". Currently, it is cutting each 3000s trace into 20 time windows.

```
function Analyzer2;

%cutting the traces
%This analyzer accepts the real-time intensity change data for multiple ROIs in the format of
%[time,average intensity,ROI1 intensity,ROI2 intensity...,error]
%It takes *.txt file yielded by using the plugin 'Time Series Analyzer' in ImageJ.
%The output are small windows of the normalized intensity of different ROIs saved under the same
folder as the source file in the form of separate 'x(value)y(value)s(starting time)e(ending time).dat'
files.

%nomenclature
%ROI: region of interest (the 4 pix region of one nanotube)

[fulldata,fname]=openfile;
time=fulldata(:,1);
[row col]=size(fulldata);

fulldata1=fulldata;   % if the txt file has the form of [time, ROI1 intensity, ROI2 intensity, average
intensity, error]
fulldata1(:,2)=fulldata(:,col-1);
for i=3:1:col-1
    fulldata1(:,i)=fulldata(:,i-1);
end
fulldata=fulldata1;

for i=1:1:row
    for j=1:1:col-3
        data3(i,j)=1000*(fulldata(i,j+2)-min(fulldata(:,j+2)))./(max(fulldata(:,j+2))-min(fulldata(:,j+2)));
    end
end

data2=1000-data3;

n=col-3;
rem1='0001-0232-0154              0001-0224-0134              0001-0239-0118...';
%input of the location of each point, with the format of "frame-X-Y"

for k=1:n;
    [token1, rem1] = strtok(rem1);
    rem2=token1;
    for i=1:3
        [token2, rem2] = strtok(rem2, '-');
        k;
        i;
        str2num(token2);
```

153

```matlab
        array(k,i)=str2num(token2);
    end
end


x=array(:,3);
y=array(:,2);

inv=150;   %specify the desired time interval to cut the traces

for j=1:1:col-3
    for q=1:inv:(inv*(floor(row/inv)-2)+1)
    resultarray=[time(q:(q+inv)) data2(q:(q+inv),j) data3(q:(q+inv),j)];
    name=['x' num2str(x(j)) 'y' num2str(y(j)) 's' num2str(q) 'e' num2str(q+inv) '.dat'];
    save(name,'resultarray','-ascii');
    end
    resultarray=[time((inv*(floor(row/inv)-1)+1):row)        data2((inv*(floor(row/inv)-1)+1):row,j)
data3((inv*(floor(row/inv)-1)+1):row,j)];
    name=['x' num2str(x(j)) 'y' num2str(y(j)) 's' num2str((inv*(floor(row/inv)-1)+1)) 'e' num2str(row)
'.dat'];
    save(name,'resultarray','-ascii');
end

function [BB, fname]=openfile;

    [FileName,PathName] = uigetfile('*.txt','Select the directory and file');
    source=sprintf('%s%s',PathName,FileName)
    cd(PathName);
    fname=FileName;

fid=fopen(FileName,'r');
count = 0;
while ~feof(fid)
    line = fgetl(fid);
    if isempty(line) | strncmp(line,'%',1)
        continue
    end
    count = count + 1;
end
fid=fopen(FileName,'r');
A=fscanf(fid,'%g');
N=length(A);
frewind(fid);
A=fscanf(fid,'%g',[N/count count]);
BB=A';
fclose(fid);
```

The following MATLAB program finds the steps in a given fluorescence trace. The main program is "StateFinder2" which calls "StepFinder".

```
function StatesFinder2;
%this will find the number of states per trace and document it in the file name as 'statenumber
filename'

global B; % this is simply a column data to send to StepFinder

directory  = 'path\';
filestruct=dir([directory '\*.dat']);

for q=1:size(filestruct,1)
    fid=fopen([directory,filestruct(q).name], 'r');
    A=textscan(fid, '%f %f %f');

    time=A{1};
    data=A{3}./1000;
    timeinc=time(2,1)-time(1,1);
    fulldata=[A{1} A{2} A{3}];

    fitdata=data;
    antifit=data;
    maxN=31; %maximum number of steps per trace

    resultArray=zeros(maxN,3); %first column the begnning index. second column is the length. third
colum is the step fit.
    resultArray(1,1)=1;
    resultArray(1,2)=length(data);
    resultArray(1,3)=mean(data);
    fitdata(:)=resultArray(1,3);
    chisquaredFit=zeros(maxN,1);
    chisquaredAntifit=zeros(maxN,1);
    chisquaredFit(1)=sum((data-fitdata).^2,1);
    SS=zeros(maxN,1);
    SS(1)=1;

    flag=0;

    for i=1:(maxN-1),
      para=0;
      for j=1:i,
        temp=resultArray(j,1);
        temp2=resultArray(j,2);
        B=data(temp:(temp2+temp-1));
        [StepSize,StepLocation,left,right]=StepFinder;
        temp3=StepSize*(temp2)^0.5;
        if temp3 > para,
          para=temp3;
          newBegin1=temp;
          newLength1=StepLocation-1;
          newValue1=left;
          newBegin2=temp+StepLocation-1;
```

155

```
        newLength2=temp2-newLength1;
        newValue2=right;
        bestJ=j;
      end
    end

    resultArray(bestJ,1)=newBegin1;
    resultArray(bestJ,2)=newLength1;
    resultArray(bestJ,3)=newValue1;
    resultArray(i+1,1)=newBegin2;
    resultArray(i+1,2)=newLength2;
    resultArray(i+1,3)=newValue2;
    %resultArray(1:i+1,:)
    currentFitArray=sort_on_key(resultArray(1:i+1,:),1);
    antiFitArray=zeros(i+2,3);
    antiFitArray(1,1)=1;
    antifitArray(1,2)=length(data);
    for j=1:(i+1),
      temp=currentFitArray(j,1);
      temp2=currentFitArray(j,2);
      if (temp2 == 1)
        flag = 1;
        break;
      end
      B=data(temp:(temp2+temp-1));
      [StepSize,StepLocation,left,right]=StepFinder;
      antiFitArray(j+1,1)=temp+StepLocation-1;
    end
    if (flag == 1)
        break;
    end
    for j=1:i+1,
      antiFitArray(j,2)=antiFitArray(j+1,1)-antiFitArray(j,1);
      antiFitArray(j,3)=mean(data(antiFitArray(j,1):(antiFitArray(j,2)+antiFitArray(j,1)-1)));
    end
    antiFitArray(i+2,2)=length(data)-antiFitArray(i+2,1)+1;
    antiFitArray(i+2,3)=mean(data(antiFitArray(i+2,1):end));

    for j=1:i+1,
      fitdata(resultArray(j,1):(resultArray(j,2)+resultArray(j,1)-1))=resultArray(j,3);
    end
    for j=1:i+2,
      antifit(antiFitArray(j,1):antiFitArray(j,2)+antiFitArray(j,1)-1)=antiFitArray(j,3);
    end


    chisquaredFit(i+1)=sum((data-fitdata).^2,1);
    chisquaredAntifit(i+1)=sum((data-antifit).^2,1);
    SS(i+1)=chisquaredAntifit(i+1)/chisquaredFit(i+1);

    resultArray0 = resultArray;

end
```

i

filestruct(q).name

resultArray = resultArray0;

```
SS;
[C,I]=max(SS);

bestfitnumber=I;
resultArray(1,1)=1;
resultArray(1,2)=length(data);
resultArray(1,3)=mean(data);
fitdata(:)=resultArray(1,3);
chisquaredFit=zeros(maxN,1);
chisquaredFit(1)=sum((data-fitdata).^2,1);
for i=1:(bestfitnumber),
  para=0;
  for j=1:i,
    temp=resultArray(j,1);
    temp2=resultArray(j,2);
    B=data(temp:(temp2+temp-1));
    [StepSize,StepLocation,left,right]=StepFinder;
    temp3=StepSize*(temp2)^0.5;
    if temp3 > para,
      para=temp3;
      newBegin1=temp;
      newLength1=StepLocation-1;
      newValue1=left;
      newBegin2=temp+StepLocation-1;
      newLength2=temp2-newLength1;
      newValue2=right;
      bestJ=j;
    end
  end

  resultArray(bestJ,1)=newBegin1;
  resultArray(bestJ,2)=newLength1;
  resultArray(bestJ,3)=newValue1;
  resultArray(i+1,1)=newBegin2;
  resultArray(i+1,2)=newLength2;
  resultArray(i+1,3)=newValue2;

end
  for j=1:bestfitnumber+1,
    fitdata(resultArray(j,1):(resultArray(j,2)+resultArray(j,1)-1))=resultArray(j,3);
  end
  finalresult=sort_on_key(resultArray((1:bestfitnumber+1),:),1);
  finalresult(:,1)=(finalresult(:,1)-1)*timeinc+time(1);
  finalresult(:,2)=finalresult(:,2)*timeinc;
  statesnum=length(unique(round(10*finalresult(:,3))))
```

157

```
    plot(time, data,'g',time, fitdata, 'r');
    token=strtok({filestruct(q).name},'.');
    t=token{1};
    save([directory num2str(statesnum) t '.dat'],'fulldata','-ascii');
    fclose(fid);
end


%save([fname 'stepAnalysis.dat'],'finalresult','-ascii');


function sorteer=sort_on_key(rij,key)
    %this function reads a (index,props) array ands sorts along the index with one of the
    %props as sort key
    size=length(rij(:,1));
    sorteer=0*rij;
    buf=rij;
    for i=1:size
        [g,h]=min(buf(:,key));
        sorteer(i,:)=buf(h,:);
        buf(h,key)=max(buf(:,key))+1;
    end
```

The program which "StateFinder2" calls:

```
function [StepSize,StepLocation,left,right]=StepFinder;
global C
global B; %this is what we receive from the main program
lengthB=length(B);
fitResult=B;
tempfit=B;
StepSize=0;
bestchisquared=10^10;
time=(1:lengthB);
StepLocation=1;

for i=1:(lengthB-1),
  C=zeros(i,2);
  C(:,1)=(1:i)';
  C(:,2)=B(1:i);
  A1=mean(C(:,2));
  tempfit(1:i)=A1;
  C=zeros((lengthB-i),2);
  C(:,1)=((i+1):lengthB)';
  C(:,2)=B((i+1):lengthB);
  A2=mean(C(:,2));
  tempfit((i+1):lengthB)=A2;
  chisquared=sum((tempfit-B).^2,1);
  if chisquared < bestchisquared,
    bestchisquared=chisquared;
    fitResult=tempfit;
    StepSize=abs(A2-A1);
    StepLocation=i+1;
    left=A1;
    right=A2;
  end
end
```

The following MATLAB program, AccumuTranstep, counts the transitions in a trace and save the total counts in a "*.dat" file.

```
function AccumuTranstep
%no cutting of the trace
%statenum in file name
%# of transitions vs ranked sensor
directory1   = "path'\';
filestruct1=dir([directory1 '*report.dat']);
for q=1:size(filestruct1,1)
    fid=fopen([directory1,filestruct1(q).name], 'r');
    A=textscan(fid, '%f %f %f %f %f', 'headerlines', 4);
    B=A{5};
    [token1,rem1]=strtok({filestruct1(q).name},'x');
    [token2,rem2]=strtok(rem1,'y');
    [token3,rem3]=strtok(rem2,'report');
    token2=strtok(token2,'x');
    token3=strtok(token3,'y');
    statenum=str2num(token1{1});
    m1(q)=str2num(token2{1});
    n1(q)=str2num(token3{1});

    if (statenum == 1)
        num1(q)=0;
    elseif (statenum == 4)
        num1(q)=B(5)+B(10)+B(15);
    elseif (statenum == 3)
        num1(q)=B(4)+B(8);
    elseif (statenum == 2)
        num1(q)=B(3);
    elseif (statenum == 5)
        num1(q)=B(6)+B(12)+B(18)+B(24);
    elseif (statenum == 6)
        num1(q)=B(7)+B(14)+B(21)+B(28)+B(35);
    elseif (statenum == 7)
        num1(q)=B(8)+B(16)+B(24)+B(32)+B(40)+B(48);
    elseif (statenum == 8)
        num1(q)=B(9)+B(18)+B(27)+B(36)+B(45)+B(54)+B(63);
    elseif (statenum == 9)
        num1(q)=B(10)+B(20)+B(30)+B(40)+B(50)+B(60)+B(70)+B(80);
    end
    fclose(fid);

end
resultarray1=[m1' 320-n1' num1'];
resultarray1=sortrows(resultarray1,3);
[row1 col1]=size(resultarray1)
save('name.dat','resultarray1','-ascii');

y1=(1:row1)/row1;
x1=resultarray1(:,3);
```

Appendix B: Length Separation of SWNT

Length Separation of Sodium Deoxycholate-SWNT

Single-walled HiPco carbon nanotubes (Rice University) were suspended with 2 wt% sodium deoxycholate surfactant (Sigma) with a SWNT concentration of 100mg/L. The sample was sonicated with a probe tip sonicator in an ice water bath at 9W for 2h. Each suspension was centrifuged at 21000g for 2h to get individually-dispersed SWNT. Using the technique in a recent paper (Fagan, J. A.; Becker, M. L.; Chun, J.; Hobbie, E. K. Length Fractionation of Carbon Nanotubes Using Centrifugation. Advanced Materials 2008, 20, 1609-1613), SWNT are length separated using density gradients and ultracentrifugation.

Re-Suspension of Sodium Deoxycholate-SWNT in DNA

Length fractions of sodium deoxycholate-SWNT were collected and then flocked using methanol. The flocked SWNT were then washed with water (nanopure) several times to get rid of the surfactant and iodixanol used in the density gradient in the ultracentrifugation step. Finally, an extra 3 day dialysis against water (nanopure) using 12-14 kDa molecular weight cutoff dialysis tubing (Spectrum Laboratories Inc.,Rancho Dominguez,CA) with 3 water changes per day was performed to ensure that all the surfactant and iodixanol were removed.

The length-separated SWNT were then re-suspended in a 30-based d(GT)15 (Biotechnology Center, University of Illinois-Urbana Champaign) with a 1:4 mass ratio in 0.1 M NaCl in distilled water and bath sonicated for 1h. The mixture was then

161

ultracentrifuged for 4hr at 30000 rpm (100,000g) and the pellet discarded, yielding individually dispersed DNA-SWNT.

Length Characterization by Atomic Force Microscope (AFM)

Dimension 3100 (Digital Instruments) was used for AFM imaging. Samples were prepared by depositing solution of d(GT)$_{15}$-SWNT(5mg/L) on thermally oxidized silicon wafer (600nm SiO$_2$, Montco Silicon Technologies). SWNT solution of 20 μL was drop dried on the cleaved wafer (30mm×30mm) followed by rinsing with copious amount of nanopure water. Both topographic and height images were recorded during AFM anaysis. The length of the individual (unbundled) nanotubes was measured using the Digitial Instruments (DI) software. An example AFM image of each length used in this study is shown in Fig. A1.
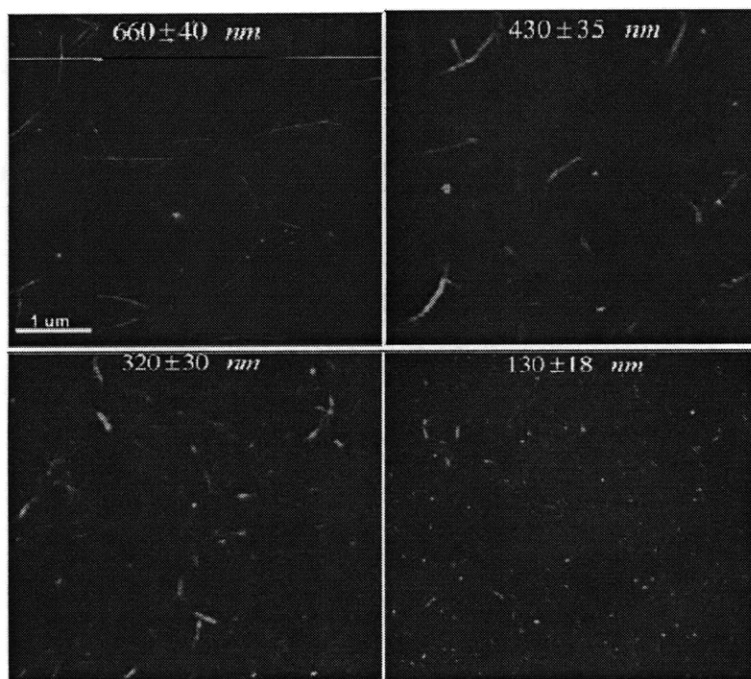
Figure A1: Example AFM images of the DNA-SWNT samples used in this work, with a calculated length of 660 ± 40nm, 430 ± 35nm, 320 ± 30nm and 130 ± 18 nm respectively

Appendix C: Size-dependent Uptake Model for Nanoparticles

For a typical incubation experiment where nanoparticles are co-incubated with a cell population at $t = 0$ (t: time), the equations can be written as (Fig. 2.12a):

$$\frac{dL}{dt} = (-k_f LR_s + k_r C_s)(n/N)$$

$$\frac{dC_s}{dt} = k_f LR_s - (k_r + k_e)C_s + k_{rec}C_i$$

$$\frac{dC_i}{dt} = k_e C_s - k_{rec}C_i$$

Here, n represents the cell density (cells/L) and N represents Avogadro's number.

For convenience, parameters can be grouped and simplified:

$$\frac{dL}{dt} = (-k_a L + k_r c_s) \qquad \text{(Eq.A1)}$$

$$\frac{dc_s}{dt} = k_a L - (k_r + k_e)c_s + k_{rec}c_i \qquad \text{(Eq.A2)}$$

$$\frac{dc_i}{dt} = k_e c_s - k_{rec}c_i \qquad \text{(Eq.A3)}$$

Where

$$k_a = k_f R_{s0}(n/N) \qquad \text{(Eq.A4)}$$

$$c_s = C_s(n/N) \qquad \text{(Eq.A5)}$$

$$c_i = C_i(n/N) \qquad \text{(Eq.A6)}$$

R_{s0} is the initial surface receptor density.

The solution by Laplace transform yields:

$$c_i = \frac{k_a k_e L_0}{\lambda_+ \lambda_- (\lambda_+ - \lambda_-)}((\lambda_+ - \lambda_-) + \lambda_- e^{-\lambda_+ t} - \lambda_+ e^{-\lambda_- t}) \qquad \text{(Eq.A7)}$$

where

$$\lambda_{\pm} = \frac{(k_r + k_e + k_a + k_{rec}) \pm \sqrt{(k_r + k_e + k_a + k_{rec})^2 - 4(k_r k_{rec} + k_a k_e + k_a k_{rec})}}{2}$$

For a typical perfusion experiment described in this work, the initial condition for L(t) is approximately a diffusion-controlled Gaussian distribution that, in practice, is asymmetric and represented as a summation of Gaussians. Gaussian/normal distribution is chosen to characterize the concentration change of SWNT in our perfusion experiment because the change is diffusion-controlled and is continuous. Other distribution like Boltzmann distribution is more often used in quantum physics where there are obviously different states. For our system, we injected SWNT into a perfusion chamber, and the SWNT is further diluted by the injected media. The concentration change should be continuous, and no distinct states should be expected. Hence it is better described by the Gaussian distribution. Equation A2 becomes:

$$\frac{dc_s}{dt} = k_a L_0 \overline{N(\mu, \sigma^2)} - (k_r + k_e)c_s + k_{rec}c_i \qquad (Eq.A8)$$

Where $N(\mu, \sigma^2)$ is the transient, pseudo-Gaussian distribution of nanoparticles with a mean of μ and a variance of σ^2 that passes over the cell in the perfusion field. In this case, numerical solution of Eq. A3 and Eq. A8 is most convenient for obtaining the profiles of c_i and c_s. Experimentally, investigators typically measure the nanoparticle uptake as a function of exposure time which is potentially a function of both the endocytosis and exocytosis rates. Hence, the above model can be utilized to estimate rate constants for nanoparticle uptake for comparisons of nanoparticle uptake between various particle geometries and composition.

By this definition, the endocytosis rate constant, k_e, is predicted by the previous model derived by Gao and co-workers.

Appendix D: Betabinomial Distribution Derivation

Similar as the Gamma distribution case, the rank ordered sensor response can be described by beta binomial function (Fig. 4.7d):

$$x = n(1 - \frac{N \cdot B(\beta + N - y - 1, \alpha + y + 1) \cdot \Gamma(N) \cdot F_n(\alpha, \beta; y)}{B(\alpha, \beta) \cdot B(N - y, y + 2) \cdot \Gamma(N + 2)}) = n \cdot betabino(\alpha, \beta, N; y) \quad (Eq.A8)$$

Where x is the rank order; y is the rank ordered sensor response in the unit of number of quenching transitions; n is the total number of sensors; N is the maximal of all the sensor response; $B(\alpha, \beta)$ is a beta function with parameters $\alpha = 1$ and $\beta = 3$; $\Gamma(N)$ is gamma function; $F_n(\alpha, \beta; y) = {}_3F_2(1, \alpha + y + 1, -N + y + 1; y + 2, -\beta - N + y + 2; 1)$ is a generalized hypergeometric function.

To obtain the parameters in beta binomial distribution for our films, we first measured the quenching of H_2O_2 on the cell-free collagen film as controls. Four different concentrations were explored: 10 μM, 20 μM, 50 μM and 100 μM. The accumulative quenching transitions over an observation window of 3000s were counted for each nanotube sensor and then rank ordered. The distinct feature observed throughout all control experiments yields $\alpha = 1.2 \pm 0.15$ and $\beta = 3.0 \pm 0.12$ in the beta distribution on sensor capture probability from Eq. A8.

The membrane generation is just

$$y_{Local}(x) = y(x) - betabino^{-1}(\alpha, \beta, N; \frac{x}{n}) \quad (Eq. A9)$$

A small number of data points at x->0 are enough to recover both the background (Eq. A8) from any experimental curve. Membrane generation can be recovered from Eq. A9 as has explained previously.

Appendix E: MATLAB Programs for Intelligent Data Collection on the Microscope

1. Design overview

The goal is to have our microscopes (Zeiss Axio Observer D1) perform what a human microscope operator could have performed. Human beings make decisions and decide what and when to image. Two types of decisions are important:

a. Where to image in the XY plane

b. Where to image in the Z axis, make sure the image is in focus

There are commercially available fully-automated microscopes that can perform some of these tasks. One problem is that we have to use the commercially available software which can only control limited parts of the microscope. In reality, microscope setups are usually customized for certain needs, and the ideal is to control as many parts of this setup as possible, have each part programmed to act and collect data, in whatever way that we want them to be. It should be noted that although this software is written specifically for our microscopes, the idea and the configuration steps can be adapted for similar platforms as well.

2. Hardware and software specifications

Hardware

i.   Microscope   parts

   (1) Zeiss Axio Observer D1

   (2) Objectives

   (3) Cameras – one CCD and one InGaAs detector

   (4) filter sets

ii. Automation Stage and control – Ludl controller: MAC 5000, external Z focus package

(focus drive - axio imager, focus drive encoders, focus drive electronics, etc.)
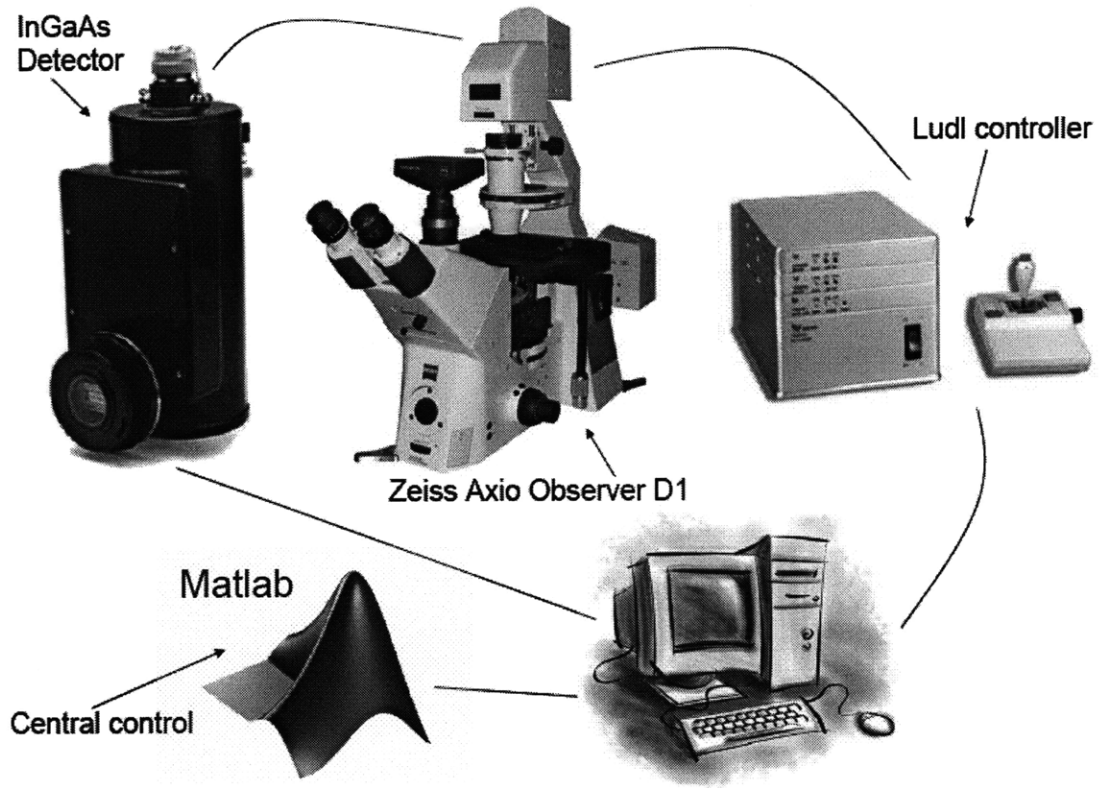
A 9-pin null modem serial cable (one male and one female head) has been used to

connect the Ludl controller to the computer for central control

Software

i. μManager (an open-sourced java-based software, has the ability to perform   limited

amount of intelligent movement)

ii. Matlab

Please also refer to the design scheme in Fig. E1.

Figure E1. Automation scheme

3. Have different devices "talk" with the central control

This is the first and most difficult part in this procedure. After a thorough research, I have found an open source software, μManager, which can help us get started.

Micro-manager was designed in a modular fashion with three distinct layers.

The Core exports its capabilities to higher levels through an interface that is computer language independent.

At the bottom there is a layer of 'Device adapters' that interfaces to the actual device drivers or talks to the hardware through serial, USB, or other ports.
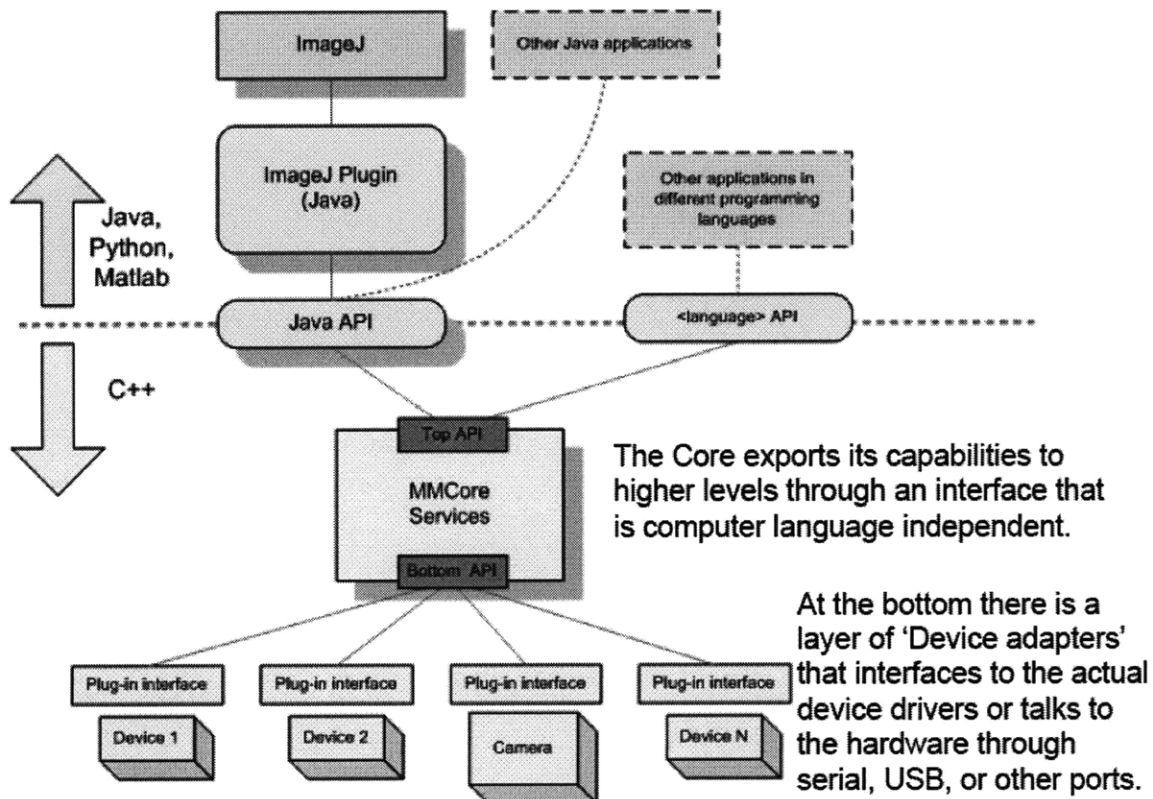
Stuurman, N., Amodaj N., Vale, R.D. (2007). Micro-Manager: Open Source software for light microscope imaging. **Microscopy Today**. 15(3):42-43

Figure E2. The structure of the open-source software

The μManager software was designed in a modular fashion with 3 distinct layers (Fig. E2). At the bottom there is a layer of 'device adapters' that interfaces to the actual device drivers or talks to the hardware through serial, USB, or other ports. Next, there is the central 'Core' that integrates all basic functionality. The Core exports its capabilities to

higher levels through an interface that is computer language independent. Therefore, it is possible to use the μManager functionality from many different environments. For instance, Matlab. Because of the modular structure of the μManager software, it is straight-forward to add support for new hardware devices. In order to control a specific microscope system, the computer needs to know what hardware is part of the microscope, in other words, we need to have these devices to be able to talk with the central control. This step is realized by writing device adapters (specific for each device) for μManager, based on the device developer's kit. Once these device adapters have been written, we are ready to configure these devices and generate a configuration file through μManager, which can be further interfaced with Matlab.

Right now, both the InGaAs detector and the Ludl stage controller have been successfully configured on our microscope. The name of the configuration file is "MMConfig_demo2.cfg" on the computer attached to this microscope in our lab, which will be used in Matlab in the next section.

4. Use Matlab to interface and have central control

The following procedure has been tested to work:

a. Install μManager in a path without any spaces (for instance: C:\Micro-Manager1.3)

b. Add the path with the drivers (all the .dll files) to the windows PATH environmental variable (Start->Settings->Control Panel->System->Advanced->Environment Variables, make a new 'User variable for Administrator named 'PATH' and set it to the location of Micro-Manager (for instance: C:\Micro-Manager1.3)

c. Open Matlab, in command window, prompt

>>edit classpath.txt

Add the location of the jar file you just installed (in the Micro-Manager folder), include the .jar at the end, for instance:

C:/Micro-Manager1.3/plugins/Micro-Manager/MMCoreJ.jar

C:/Micro-Manager1.3/plugins/Micro-Manager/MMJ_.jar

d. In matlab command prompt

    >>edit librarypath.txt

Add the location of the dll files, for instance: C:\Micro-Manager1.3

e. Researt Matlab

f. Create a java object of class MMCcore

>> mmc = MMCcore;

Then we can call all methods through that object in Matlab.

5. Demonstrations

a. Stage movement and image acquisition

<u>Main</u> Matlab code: "takeimage.m"

```
%% Basic "command line" usage
% This demo show how to initiate the scope and perform basic operation
% directly with the rS object. These operation could be performed from the
% command line. This basic functionality doesn't use the more advanced Task
% based scheduling but by itself is very useful (you can loop and do
% whatever you want :)

%% Initilize the Scope
% the scope configuration file that will be passed to MicroManager. In this
% example we are using the Demo init file *.cfg.

clear all
close all
ScopeConfigFileName='C:\Micro-Manager-1.3\MMConfig_demo2.cfg';

% call the constractor of the Scope
global rS; % name of the scope (rS=roboScope)
rS=Scope(ScopeConfigFileName);

disp('Scope initialized');

%% Move the stage in 3D
set(rS,'x',x+100,'y',y+100,'z',z+10);

%% Acquire an image in single channel
img=acqImg(rS,'',500);   %exposure unit: msec
load background.txt
img1=img-background;

figure(1)
imshow(img1)

%% Close gracefully
unload(rS)
```

The main Matlab code: "takeimage.m" calls "acqImg.m" and "Scope.m"

"acqImg.m"

```
function img = acqImg(rSin,Channel,Exposure)
% acqImg : performs image acquisition
% captures a (multichannel) image based on Channel / Exposure arguments.
%
% sets the channel and exposure for each channel
% rS      - the microscope object
% Channel   - the channel to image a cell array of strings (single char
%            will be converted to a cell array with single element)
% Exposure: - the exposure time for all channels (a double array)
% img - a 3D matrix where size(img,3)==length(Channels)
%
% example:
%       img = acqImg(rS,'FITC',100)
%       img = acqImg(rS,{'FITC','Cy3'},{300,100})
%       img = acqImg(rS)

global rS;
rS=rSin;

% check if it's a fake acquisition
if ~isempty(get(rS,'fakeacq'))
   dr=dir(get(rS,'fakeacq'));
   dr=dr(3:end);
   dr=dr(randperm(length(dr)));
   img=imread(fullfile(get(rS,'fakeacq'),dr(1).name));
   rS.lastImage=img;
   [w,h]=get(rS,'Width','Height');
   img=imresize(img(:,:,1),[h w]);
   pause(1)
   return
end

[w,h,bd]=get(rS,'Width','Height','BitDepth');

% if no exposure settings, use current rS setting
if ~exist('Channel','var')
   Channel=get(rS,'channel');
end
% if channel is not a cell array
if ~iscell(Channel)
   Channel={Channel};
end

if ~exist('Exposure','var')
   Exposure=get(rS,'exposure');
end

n=length(Channel);
```

174

```
img=zeros(h,w,n); % notice the transpose element in the loop
for i=1:n
    set(rS,'Exposure',Exposure(i));
    rS.mmc.snapImage;
    imgtmp=rS.mmc.getImage;
    img(:,:,i)=reshape(single(imgtmp)./(2^bd),w,h)';
end

rS.lastImage=img;
```

"Scope.m"

```matlab
function rS = Scope(config_file)
% Scope Constructor of the Scope class
% creates a rS object based on the config file. If no config file is
% supplied, it create the Micro-Manager GUI which asks for the config file.
% All devices etc must be configured in the MMC config_file

%% names of devices in the configuration file.
rS.XYstageName='XYStage';
rS.ZstageName='ZStage';
rS.COM='COM1'; %the focus port for ASI
% rS.OBJName='Objectives'; % the GroupConfig for the objectives
% rS.ChannelName='Channels';
% rS.LightPathName='LightPath'; % ConfigGroup of the light path
% rS.EMgainName='EM-Gain';


%% Here we initialize the MMC core part of rS
% if config file is empty - start witht he GUI otherwise
% start using the cnfig file directly.

import mmcorej.*;

% rS.mmc=CMMCore;
rS.gui=[];
try
    if nargin ==0 || isempty(config_file)
        rS.gui=MMStudioPlugin;
        rS.gui.run('')
        uiwait(msgbox('Click me - I"m beutiful'))
        rS.mmc=rS.gui.getMMCoreInstance;
    else
        rS.mmc=CMMCore;
        rS.mmc.loadSystemConfiguration(config_file);
    end
    % try to load devices - if an error occurs unload and clean
catch
    rS.mmc.unloadAllDevices;
    rS=[]; %#ok<NASGU>
    uiwait(msgbox('An error occured during device loading - please close MM, correct the hardware
problem and try again'))
    error('An error occured when loading devices - rS is not a functional Roboscope! \n %s',lasterr);
end

%% Additional properties not part of Stage or MMC:
% task ID
rS.taskID=0;

%root folder - defaults is current
rS.rootFolder='./';

% resolve error - default is yes
```

176

```
rS.resolveErrors=true;

% default focus method
% must be a funciton handle to a file in the AutofocusFcns folder
rS.focusMethod='dualScanImageBased';
rS.focusParam=struct();

% default scheduling method
% must be a funciton handle to a file in the SchedulerFcn folder
rS.schedulingMethod='greedy';

% Units
rS.units.stageXY='micro-meter';
rS.units.stageZ='micro-meter';
rS.units.exposureTime='msec';
rS.units.acqTime='sec';

% the last image captured, only saving that one (but could be a 3 channel
% image as well...
rS.lastImage=[];

% perform printscreen? if its not empty it must be a name of a folder
rS.printScreenFolder='';

% should it capture real or fake images?
rS.fakeAcquisition='';

% create the defaults plots
Plots={'planned schedule',1,[10  597  350  309];
    'focal plane',2,[10  246  350  309];
    'image',3,[380  348  894  627];
    'task schedule',4,[ 10   40  364  169];
    'task status',5,[ 380   40  483  173]};
rS.plotInfo=cell2struct(Plots,{'type','num','position'},2);

% the task buffer and schedule (the schedule carry the task id in the right order)
rS.TaskBuffer=[];
rS.TaskSchedule=[];
rS.refreshSchedule=Inf;

% Focus points - This is a list of points where rS know it had good focus
% existing points are needed for rS to be able to guess another point
rS.FocusPoints=[]; %[X Y Z T]
rS.FocusPointsHistory=1/1440; %Number of days that are used in the updateFocalPlaneGrid
rS.FocusPointsProximity=10; %the distance of points for which the history is relevant
rS.FocalPlaneGridSize=25;

% % set it in mmc
% rS.mmc.setState('Objective',ObjectiveLbl);

% load the pixel sizes from file
rS.pxlsz.label='100x';
rS.pxlsz.um=0.286;
```

```
% Focus mnethod and parameters
rS.focusMethod='noAutoFocus';
rS.focusParams=struct('placeholder',1); %will be updated in first call for getFocusParams

%% create the object from struct
rS=class(rS,'Scope');

%% update all the defaults for focus functions

%% add path - "Plug-in" folders
addpath TaskFcns
addpath SchedulerFcns
addpath AutofocusFcns
addpath DecisionFcns
addpath(['ThirdParty' filesep 'utilities'])
```

This demo shows that we now have the ability of having control over the microscope parts via a Matlab interface without any third party software. Improvement on its "intelligence" includes scheduling of events, auto refocus, etc., the algorithm of which is going to discussed in the following section.

b. Autofocus algorithm implantation

This is the key issue in any imaging application, especially if programmed movement of the stage is involved which is almost certain to cause the loss of focus. Based on the nature of our microscope and the main focus of our lab, we will image mostly in the near infrared, thus the algorithm is near infrared based as well (where the objects that we will focus on are nanotubes)

In image processing, noise reduction is usually necessary before performing higher-level processing steps, such as edge detection. The median filter is a non-linear digital filtering technique, often used to remove noise from images. Its edge-preserving nature makes it useful in our analysis.

The following algorithm has been selected from various algorithms and tested to work:

First, take a sequence of images at different Z positions.

Second, compare the 'sharpness' of each image, where the sharpness of an image is computed by:

applying 3×3 median filter to the image to remove noise

convolute image with a filter [-2 -1 0; -1 0 1; 0 1 2]

sum the square of each entry in the convoluted image

Third, compare the sharpness. If this makes the calculation too slow, we can randomly choose part of the imaging field (suppose everything is homogenous and part of the field is representative) and calculate the sharpness there.

Below is the comparison between the current filter (in the circle) with other filters on nanotube film samples. The score is the result of the sharpness function.
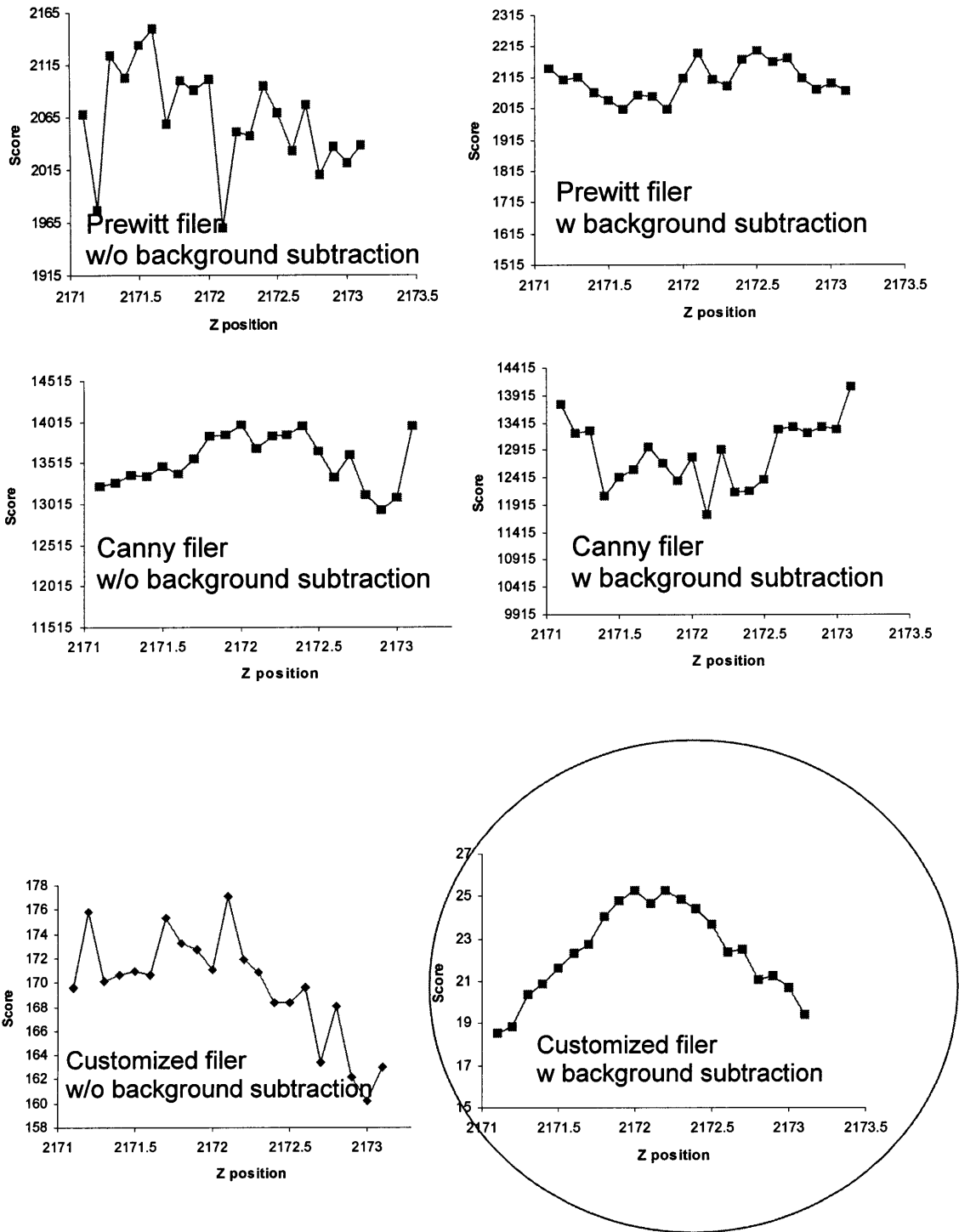
Figure E3. Comparison between different filters

180

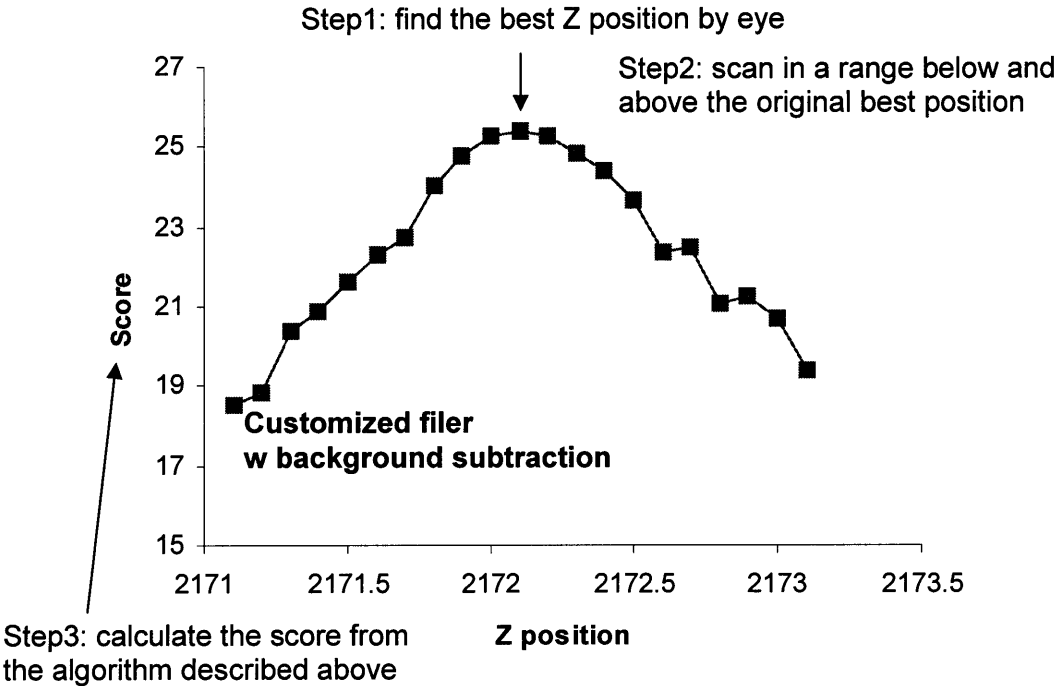The refocus algorithm is not likely to start with one layer in a matrix containing nanotubes and end with another layer based on the following tests on real samples of SWNT films.

0.1um stepsize

0.05um stepsize
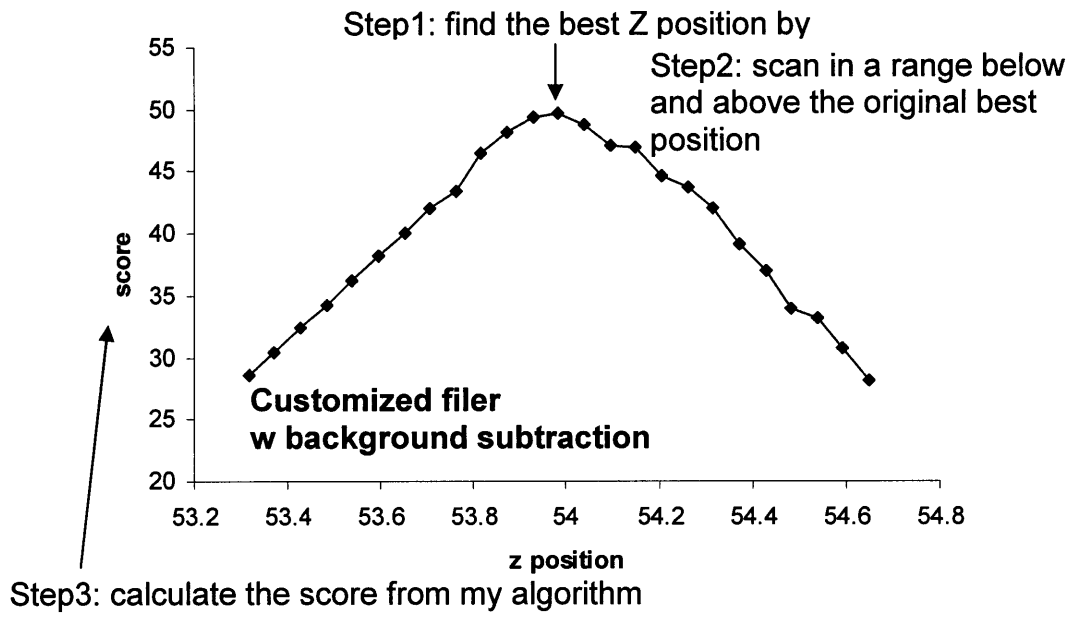0.05um is the resolution of the current focus drive

Figure E4. The bell-shaped curves

Main Matlab code: "Refocus.m"

```
function Refocus
global rS
ScanRange=0.05;
NumOfStepsInScan=3;
load background.txt

%% First coarse scan
Zcrnt=get(rS,'z');
Zscan1=Zcrnt+linspace(-ScanRange,ScanRange,NumOfStepsInScan);
Zres1=2*ScanRange/(NumOfStepsInScan-1);

%move to the lowest position and aquire score
[x,y,z]=get(rS,'x','y','z');
set(rS,'z',z-(Zcrnt-Zscan1(1)));
img0=acqImg(rS,'',500);   %exposure unit: msec
img0s=img0-background;
scor0=filter2([-2 -1 0;-1 0 1;0 1 2], medfilt2(img0s, [3 3]));
Scr0=sum(sum((scor0.^2)));
bestScr1=Scr0;
bestZ1=Zscan1(1);

for i=2:NumOfStepsInScan(1)
    [x,y,z]=get(rS,'x','y','z');
    set(rS,'z',z+Zres1);
    img1=acqImg(rS,'',500);   %exposure unit: msec
    img1s=img1-background;
    scor1=filter2([-2 -1 0;-1 0 1;0 1 2], medfilt2(img1s, [3 3]));
    Scr1(i)=sum(sum((scor1.^2)));
    if Scr1(i) > bestScr1;
        bestScr1=Scr1(i);
        bestZ1=Zscan1(i);
    end
end

bestZ1

% Move the stage to the best Z
[x,y,z]=get(rS,'x','y','z');
set(rS,'z',z-(Zscan1(NumOfStepsInScan)-bestZ1));
```

Movie collection

Method 1: Array

First preallocate array M(x,y,frame#) with zeros before movie collection, then take data which is going to be written into the array.

Advantages: very fast; almost no loss of time between frames

Problems: memory intensive; the matrix cannot be very large; with 1G memory, approx~1200 frames

Method 2: Use timer object
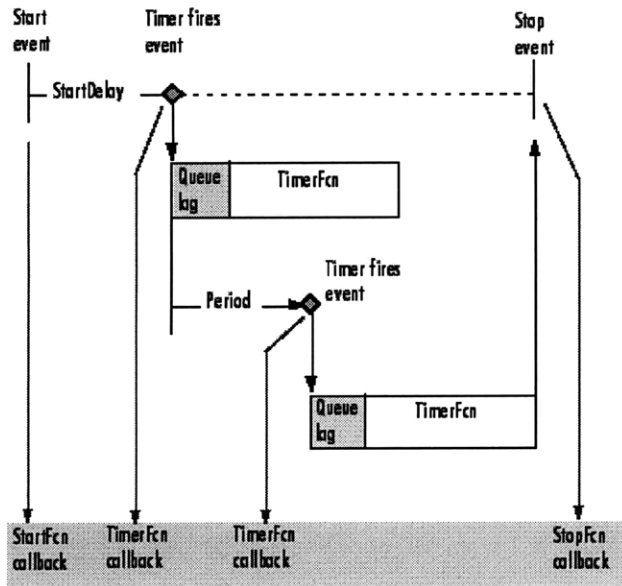
Advantages: not memory intensive; exact save time documented for each file (HHMMSS)

Problem: Queue lag time is ~0.5s for each frame

Method 3: Acquire image and then save within the same loop

Advantages: not memory intensive;

Problem: "background saving time" – because each file is saved in the same loop as image acquisition

Now optimize the total collection time. First, try to find the bottle neck.

Profiler in Matlab shows that "save" function takes 17% of the image acquisition time.

So use alternative functions (fopen, fwrite, fclose) and write data in binary format with double precision. Writing data this way takes 0.1% of the image acquisition time.

Time #of calls #of line

```
            1    57 for i=1:1499
866.75   1499    58    img=acqImg(rS,'',500);    %exposure unit: msec
  1.12   1499    59    fid=fopen([num2str(i) '.bin'],'w');count=fwrite(fid,img,'double');fclose(fid);
                 60    %save(['f' num2str(i) '.bin'],'img')
```

Use float precision instead of double saves a little more time in saving the data, but it will in turn, lower the quality of each image.

c. Intelligent movie collection

Collect movie and refocus every 500 frames. Writing data takes 0.1% of the image acquisition time and refocus takes 0.7% of the image acquisition time.

```
            1    57 for i=1:1499
866.75   1499    58    img=acqImg(rS,'',500);    %exposure unit: msec
  1.12   1499    59    fid=fopen([num2str(i) '.bin'],'w');count=fwrite(fid,img,'double');fclose(fid);
                 60    %save(['f' num2str(i) '.bin'],'img')
         1499    61    if fix(i/500)==i/500
  6.23      2    62        Refocus
            2    63    end
         1499    64 end
```

Main Matlab code: "takemovie.m".

```
clear all
close all
ScopeConfigFileName='C:\Micro-Manager-1.3\MMConfig_demo2.cfg';

global rS;
rS=Scope(ScopeConfigFileName);

disp('Scope initialized');

%another trial
for i=1:1500
    img=acqImg(rS,'',500);   %exposure unit: msec
    fid=fopen([num2str(i) '.bin'],'w');count=fwrite(fid,img,'double');fclose(fid);
    %save(['f' num2str(i) '.bin'],'img')
    if fix(i/500)==i/500
      Refocus
    end
end

disp('movie collection finished');

%% Close gracefully
unload(rS)
```

Advantages over Winspec (the current software for movie collection):

Much less "background saving" time

Winspec

safe mode: 0.5s image with 0.5s background time

fast mode: 0.5s image but very long "blackout" time after each movie, causing gaps between movies

Matlab code

Only a waste of 7e-4s per one image (in saving files). This is equivalent to 0.1% of the exposure time (if 0.5s exposure time).

Appendix F: Additional Experimental Details

Additional Experimental Details for Chapter 2

DNA Encapsulation of Single-Walled Carbon Nanotubes

Single-walled CoMoCAT carbon nanotubes (Southwest Nanotechnologies, grade S-P95-02-Dry) were suspended with d(GT)$_{15}$ sequence (Biotechnology Center, University of Illinois at Urbana-Champaign), in a 1:4 mass ratio in 0.1M NaCl in distilled water and probe-tip sonicated for 10min at 9W. The mixture was centrifuged for 4hr at 30000 rpm (100,000g) and the pellet discarded. From the AFM characterization, the band heights of DNA-SWNT reach up to 1.2 nm above the surface of the nanotube, with typical heights of 0.7-0.8 nm, and exhibit a regular spacing of 14-20 nm.

Fluorescence Microscopy

NIH3T3 fibroblast cells(ATCC) were cultured sparsely at 1.4×10^{-4}cells/μm^2 in DMEM (25 mM HEPES, 10 % FBS and pen-strep) at 37 ˚C with a 5 % CO$_2$ in a glass bottom 35mm Petri dish (MatTek Corp., P35G-1.5-14-C). The Petri dish was then put in a micro-incubation platform (Model DH-40i, Warner Instruments, Inc) on a fluorescence microscope (Carl Zeiss, Axiovert 200), with one CCD camera (Carl Zeiss, ZxioCam MRm) and one InGaAs detector (Princeton Instrument, 7531-0001) attached. Two syringes, one containing media and the other containing 5mg/L DNA-SWNT in media, were connected to a controller (PC-16, Bioscience Tools) in order to switch between the two solutions. The solutions were fed by a miniature perfusion pump (CFPS-1 Units, Bioscience Tools) into the Petri dish within the incubation stage where microscopy measurements were taken under 785nm laser excitation. Waste media solutions were

removed via a 2nd perfusion pump. Real-time movies were taken using WinSpec data acquisition program (Princeton Instruments) and SPT were done using ImageJ and its ParticleTracker plugin.

Agarose Gel Electrophoresis

Electrophoresis was performed in a 7×10cm, 1% agarose gel in 1×TAE buffer (Tris-acetate-EDTA) at pH 8.5. An initial 100V electric field was applied for 10min for a pre-run. DNA-SWNT was incubated in media for 24hr. The result of DNA-SWNT in media was compared with that of DNA-SWNT in water, after running the gel for 30min under 100V. All samples have a SWNT concentration of 100 mg/L.

Lysotracker/SWNT Colocalization

Lysosomal dye colocalization images were taken two hours after exposing cells containing GT-CoMoCAT SWNT to LysoTracker Red (Invitrogen). Cells were alternately exposed to filtered light from a xenon lamp for visible acquisition and 785 nm excitation for n-IR imaging. Visible fluorescence images were acquired using an attached AxioCam MRm CCD camera. Near-nfrared images were taken with a Princeton Instruments 2D-OMA V InGaAs camera.

Additional Experimental Details for Chapter 3

DNA Encapsulation of Single-Walled Carbon Nanotubes

Single-walled HiPco carbon nanotubes (Rice University) were suspended with three different kinds of DNA (Integrated DNA Technologies, Inc.) sequences, a 30-base d(GT)$_{15}$, a 30-base d(GC)$_{15}$ and 5'-TAG CTA TGG AAT TCC TCG TAG GCA-3' (referred to as DNA1 in the following text for convenience), in a 1:1 mass ratio in 0.1 M NaCl in distilled water and bath sonicated for 1 hour. The mixture was centrifuged for 90 minutes at 16,300 g and the pellet discarded. The supernatant was then dialyzed against 1x Tris Buffer at pH 7.4, using 100 kDa molecular weight cutoff dialysis tubing (Spectrum Laboratories Inc., Rancho Dominguez, CA) for 3-5 Days, to remove the free DNA, producing the DNA-SWNT samples used in the experiments.

DNA-SWNT Structural Study by Atomic Force Microscope

Atomic Force Microscope (AFM) samples were prepared by depositing d(GT)$_{15}$-SWNT and DNA1-SWNT on freshly cleaved mica. Dry AFM measurements were made by first exposing the mica surface to 1 M MgCl$_2$ and drying with ultra pure nitrogen before depositing d(GT)$_{15}$-SWNT solution at a concentration of 5 − 10 mg/L. Samples imaged in fluid were prepared by depositing the d(GT)$_{15}$-SWNT solution onto the mica and adding 1 M MgCl$_2$ into a Veeco Fluid Cell. A Digital Instruments Mutimode AFM in tapping mode was used for all measurements.

Aggregation Test by Dynamic Light Scattering

Dynamic Light Scattering (DLS) measurements were taken using a Brookhaven Instruments BI-200 SM goniometer, with a Lexel Argon-Ion (Model 95) 514 nm laser at a detector angle of 90°. Correlation curves of d(GT)$_{15}$-SWNT and d(GC)$_{15}$-SWNT, with and without HgCl$_2$ (1 mM), were compared using first and second delay times of 0.8 μs and 1s respectively. The diffusion coefficients were determined from a semi-logarithmic plot of the autocorrelation function against time: $\ln(G(\tau)-A)=\ln(B)-2\Gamma\tau$, using the initial linear region where G(τ) is the correlation function, τ is the time, Γ is the decay rate of the correlation function. A is the baseline intensity, and B is an instrument parameter. The relaxation rate $\Gamma=q^2D$ is related to the diffusion coefficient D, and q is

$$q = \frac{4\pi n}{\lambda}\sin\left(\frac{\theta}{2}\right)$$

where n=1.33 is the index of refraction for water, λ=514nm is the wavelength of the laser, and θ= 90° is the angle between the laser path and the detector.

Alternatively, the correlation curves were analyzed by the maximum entropy method, which computes the most probable distribution of relaxation times fitting the autocorrelation function.

Ion Binding Response of DNA-SWNT by Photoluminescence Method

DNA-encapsulated SWNT were diluted to concentrations of 5 mg/L buffered with 1x Tris buffer adjusted to a pH of 7.4. Solutions of mercury(II) chloride (Aldrich), cobalt(II) chloride hexahydrate (Acros Organics), calcium chloride (Fisher), copper(II) chloride

(Aldrich), and magnesium chloride hexahydrate (EMD Chemicals Inc., Gibbstown, NJ) were introduced to the buffered DNA-SWNT and left to equilibrate at 22 °C for at least 24 hours for the steady state experiments. Spectrofluorometry measurements were conducted using a Kaiser Optical Holospec f/1.8 imaging spectrograph (Kaiser Optical, Ann Arbor, MI). A re-circulating water bath (Fisher Scientific Inc., Isotemp 1016S) was used to control the temperature.

Temperature Dependent Thermochromism

A constant temperature cell (63-Q-10, Rectangular, Horizontal Flow Tubes, Starna Cells, Inc) was used with a water bath (Fisher Scientific Inc., Isotemp 1016S) to cycle the temperature of the purified DNA-SWNT solutions, spectrofluorometry measurements were conducted at 0 □, 20 □ and 50 □. All data were taken when the system reached steady state.

Dissociation of DNA from SWNT

Dialysis

Samples were prepared the same way as in the ion binding response for all three kinds of DNA-SWNT. The concentrations of SWNT were kept at 5 mg/L. The transition was induced using Ca^{2+} and Hg^{2+}. The d(GT)$_{15}$-SWNT solution was added with 2.5 mM Ca^{2+} to induce the transition and a further dialysis step against nanopure water was carried out using 100 kDa MW cutoff tubing for 24 hours. Further, 0.5 mM Hg^{2+} was used to induce the transitions of d(GT)$_{15}$-SWNT, d(GC)$_{15}$-SWNT and DNA1-SWNT. After an incubation of 24 hours, the samples were dialyzed against nanopure water using both 12-

14 kDa MW and 100 kDa MW cutoff tubing for 24 hours. An extra step of 24 hours dialysis using 12-14 kDa MW cutoff tubing was performed after the dialysis using 100 kDa MW cutoff tubing.

PicoGreen Assay

Two samples were obtained by equally splitting 6 mL of d(GT)$_{15}$-SWNT prepared the way specified above. An addition of 0.5 mM HgCl$_2$ was made to one sample and incubated for 24 hr to allow the system to come to equilibrium. The two samples were then dialyzed, using 100 kDa MWCO tubings against 40 mL water for 24 hr. The solution outside the dialysis membrane was collected and evaporated to dry under 20 □ by using a rotavap. Each dry sample was added with 100 μL of water. An extra 24 hr dialysis step using 3500 Da MW cutoff tubing was performed to get rid of HgCl$_2$ to make the PicoGreen samples. The PicoGreen mixture was produced by combining 50 μL of PicoGreen dyestock (Invitrogen) and 10 mL of 1x TE buffer adjusted to a pH of 7.4. An addition of 1 mL of PicoGreen mixture was added to each PicoGreen sample, to adjust the total volume to 2 ml using TE buffer, and incubated for 15 minutes for a final mixture. The fluorescence of the two final mixtures was measured by a Cary Varian Fluorescence Spectrophotometer at an excitation wavelength of 480 nm and an emission wavelength of 520 nm.

Gel Electrophoresis

Samples of d(GC)$_{15}$-SWNT and DNA1-SWNT, incubated with 0, 0.2 mM and 1 mM HgCl$_2$ for 24 hours were prepared. The final volume of each sample was 3 μL and the concentration of SWNT was kept the same. A 3 μL of 50 bp DNA ladder (Invitrogen) was used for comparison. A volume of 3 μL of blue/orange 6x loading dye (Promega)

was added to each sample. Electrophoresis was performed in a Mini-PROTEAN 3 cell (Bio-Rad Laboratories) at 250 V for 30 min, using a freshly made 20% PAGE gel buffered by 1x TBE at pH 8.5, after a pre-run under 250 V for 15min. GelStar nucleic acid gel stain (Cambrex) was used to stain the gel for 30 min afterwards. Control experiment was done using $d(GC)_{15}$ and DNA1-SWNT, incubated with and without 1 mM $HgCl_2$ for 24 hours.

Hybridization Experiment Using FRET

Modified oligonucleotide sequences labeled with the Cy3 fluorophore, biotin, and NH_2 were purchased (HPCL purified) from Integrated DNA Technologies Inc (Coralville, IA). The sequences were 5'-$Cy5(GT)_{15}Biotin$-3', 5'-$(GT)_{15}Cy3$-3' and 5'–$Cy3$-$(GT)_4G(X)(GT)_{10}$-3' where X is an amine bound to C6 on thymine. Oligonucleotide pairs were chosen to allow the formation of either a parallel strand duplex or an anti parallel strand duplex.

Sequences were annealed in a 1:1 ratio of 2-4 μM concentrations in 1x Tris pH 8 with 100 mM Na or 1 M Na. They were heated to 85 °C in a PX2 Thermal Cycler (Thermo Electron Corporation, Milford MA) for 10 minutes, then gradually cooled down to 4 °C over a period of 6 hours in a gradual controlled manner. The annealed solution at 4°C was diluted in the 1x Tris pH 8.0 buffer and kept at 4°C in a chilled quartz cuvette. Fluorescence measurements were performed on the diluted sample by exciting at 535 nm and measuring the emission with a Varian Cary Eclipse Fluorescence spectrophotometer. The temperature was controlled by a Varian Cary Single Cell Peltier accessory (Palo Alto, CA).

Circular Dichroism of DNA on SWNT

Circular dichroism (CD) measurements were taken with a JASCO J-715 spectrometer with temperature control (JASCO International Co. Ltd., Tokyo, Japan) at room temperature unless specified. Samples were freshly prepared. DI water was used in the dialysis step instead of buffer. Two kinds of experiments were done using CD. Ion-binding response experiment with d(GT)$_{15}$-SWNT and temperature dependence experiment with d(GT)$_{15}$-SWNT and d(GC)$_{15}$-SWNT. For the ion-binding response experiment, CD spectra of d(GT)$_{15}$-SWNT with various concentrations of mercury (II) chloride and calcium chloride were taken. For the temperature dependence experiment, CD spectra of d(GT)$_{15}$-SWNT and d(GC)$_{15}$-SWNT at 20□ and 50□ were taken.

Suspension of SWNT in Collagen

Single-walled HiPco carbon nanotubes (Rice University) were suspended in type 1 collagen (BD Biosciences) via 1min probe-tip sonication (1/4'' tip, 40% amplitude). One mg of SWNT was used per mL of 3.41 mg/mL collagen stock in 0.02 N acetic acid for sonication. The mixture was centrifuged for 90min at 16300g and the pellet discarded, retaining the supernatant for future experiments.

Collagen-SWNT Thin Films

Collagen-SWNT was diluted with stock collagen (3.41 mg/mL) to make 272 mg/L SWNT concentration. This solution was diluted to 50 μg/mL collagen with 0.02 N acetic acid with a final concentration of SWNT of 4mg/L for imaging purposes (the

concentration of SWNT is found by trial and error to achieve a desirable coverage of SWNT on the film) and pipetted onto glass bottom 35mm Petri dishes (MatTek Corp., P35G-1.5-14-C) in 500 μL aliquots to completely cover the glass region in the center of the dish. The collagen was dried at room temperature in a laminar flow hood. The dried film was rinsed well with PBS to remove the remaining acid. The film was stored at 4°C. A volume of 1.5 mL 0.1x PBS was added to the Petri dish before imaging.

Fluorescence Microscopy Experiments

The collagen film was imaged using a fluorescence microscope (Carl Zeiss, Axiovert 200), with a CCD camera (Carl Zeiss, ZxioCam MRm) and 2D InGaAs array (Princeton Instruments OMA 2D). Movies were acquired using the WinSpec data acquisition program (Princeton Instruments). Samples were excited by a 658 nm laser (LDM-OPT-A6-13, Newport Corp) at 35mW. After stable fluorescence intensity was observed, 500 μL of each reagent was added to reach the desirable final concentration. The large volume of 500 μL was used to avoid slow, inhomogeneous diffusion. Manganese (IV) oxide (Aldrich) was used to reverse the quenching.

Additional Experimental Details for Chapter 4

Suspension of SWNT in Collagen

Single-walled HiPco carbon nanotubes (Rice University) were suspended in type 1 collagen (BD Biosciences) via 1min probe-tip sonication (1/4'' tip, 40% amplitude). One mg of SWNT was used per mL of 3.41 mg/mL collagen stock in 0.02 N acetic acid for sonication. The mixture was centrifuged for 270min at 16300g and the pellet discarded, retaining the supernatant for future experiments.

Collagen-SWNT Thin Films

Collagen-SWNT was diluted with stock collagen (3.41 mg/mL) to make 272 mg/L SWNT concentration. This solution was diluted to 50 μg/mL collagen with 0.02 N acetic acid with a final concentration of SWNT of 8mg/L for imaging purposes (the concentration of SWNT is found by trial and error to achieve a desirable coverage of SWNT on the film) and pipetted onto glass bottom 35mm Petri dishes (MatTek Corp., P35G-1.5-14-C) in 500 μL aliquots to completely cover the glass region in the center of the dish. The collagen was dried at room temperature in a laminar flow hood. The dried film was rinsed well with PBS to remove the remaining acid. Everything was done under a sterilized environment.

Singlet Oxygen and Superoxide Generation

Rose bengal was used to generated singlet oxygen and superoxide in real time using a procedure described from a previous study (Mizukawa, H., et al, Br. J. Pharmacol. 121, 63-70, 1997). Briefly, 50 nM of rose Bengal was illuminated at 561 nm at 200mW for 30

min and the fluorescence of nanotubes upon this illumination was recorded in real time. It is reported that this procedure will generate both singlet oxygen and superoxide. MnO_2 was added to the solution to prevent any interference from H_2O_2.

Fluorescence Microscopy on Live and Fixed Cell

Human epidermoid carcinoma A431 cells and murine NIH-3T3 cells were cultured with Dulbecco's Modified Eagle's Medium (DMEM, ATCC) supplemented with 10% fetal bovine serum (FBS, Gemini Bio-Products) and 1% Pen-Strep Solution (10,000 U/mL Penicillin-G 10,000 μg/mL Streptomycin Penicillin-Streptomycin Solution, Gemini Bio-Products) at 37 °C with 5% CO2 on a collagen film in a glass bottom 35mm Petri dish (MatTek Corp., P35G-1.5-14-C) after serum starvation. Right before imaging, the cell medium was changed into Leibovitz's L-15 medium, which buffers the pH in the atmosphere. The nanotubes in the collagen film beneath the cells are then imaged using a fluorescence microscope (Carl Zeiss, Axiovert 200), with a CCD camera (Carl Zeiss, ZxioCam MRm) and 2D InGaAs array (Princeton Instruments OMA 2D). Movies were acquired using the WinSpec data acquisition program (Princeton Instruments). The nanotubes were excited by a 658 nm laser (LDM-OPT-A6-13, Newport Corp) at 35mW. After stable fluorescence intensity was observed, 500 μL of each reagent was added to reach the desirable final concentration. For experiment with fixed cells, A431 cells were washed with PBS, fixed in 4% paraformaldehyde (pH 7.4) for 10 min, washed 3 times and ready for imaging.

Fluorescent Staining of Cells

Cells were incubated with 4% PFA/PBS (USB Corporation) at 4 °C for 5 min, at room temperature for 10 min, then with 100% methanol (Sigma) at -20 °C for 10 min. The fixed cells were washed 3 times with PBS (Hyclone), permeabilize with 0.1% Triton X 100 (Sigma)/PBS for 20 min at room temperature followed by another washing with PBS. The cells were then incubated in 1% FBS/0.05% Tween (Sigma)-20/PBS for 20 min at room temperature, after which they were incubated with the primary antibody (rabbit polyclonal to EGFR, ABCAM Inc) in 1% FBS/0.05% Tween-20/PBS for 1h at room temperature. Washing and blocking were repeated. In the dark, the secondary antibody (Alexa Fluor 568 donkey anti-rabbit IgG, Invitrogen) was added in 1% FBS/0.05% Tween-20/PBS for 1h at room temperature (Alexa 1:500), after which 4',6-diamidino-2-phenylindole (DAPI, Sigma Aldrich Co.) was added with a final concentration of 1μg/L. The washing step was repeated. The sample was then mounted in Moviol (Shandon Immu-Mount, Thermo Fisher Scientific). The samples were then analyzed in Zeiss LSM 510 Meta confocal microscope using the same configuration and processed in LSM image Browser software from Zeiss.

Atomic Force Microscope (AFM)

MFP-3D (Asylum Research) was used for tapping mode atomic force microscopy (AFM) imaging. Samples were directly deposited on a 75 mm x 25 mm glass slide (VWR International) and imaged using rectangular silicon tips (Olympus AC240TS) with a nominal spring constant of 2 N/m. Both topographic and height images were recorded during AFM analysis. Height analysis was performed using Igor Pro software.